

SPATIAL AND ENERGY DISTRIBUTIONS
OF SPUTTERED ATOMS IN THIN FILM
DEPOSITION TECHNIQUES

Nastja Mahne

Doctoral Dissertation
Jožef Stefan International Postgraduate School
Ljubljana, Slovenia

Supervisor: Assoc. Prof. Miha Čekada, Jožef Stefan Institute, Ljubljana, Slovenia

Co-Supervisor: Dr. Matjaž Panjan, Jožef Stefan Institute, Ljubljana, Slovenia

Evaluation Board:

Assoc. Prof. Janez Kovač, Chair, Jožef Stefan Institute, Ljubljana, Slovenia

Assoc. Prof. Dean Cvetko, Member, University of Ljubljana, Faculty of Mathematics and Physics, Ljubljana, Slovenia

Dr. Zdravko Siketić, Member, Rudjer Bošković Institute, Zagreb, Croatia

MEDNARODNA PODIPLOMSKA ŠOLA JOŽEFA STEFANA
JOŽEF STEFAN INTERNATIONAL POSTGRADUATE SCHOOL



Nastja Mahne

SPATIAL AND ENERGY DISTRIBUTIONS OF
SPUTTERED ATOMS IN THIN FILM DEPOSITION
TECHNIQUES
Doctoral Dissertation

PROSTORSKE IN ENERGIJSKE PORAZDELITVE
RAZPRŠENIH ATOMOV PRI TEHNIKAH ZA NANOS
TANKIH PLASTI
Doktorska disertacija

Supervisor: Assoc. Prof. Miha Čekada

Co-Supervisor: Dr. Matjaž Panjan

Ljubljana, Slovenia, January 2024

To my beloved family

Acknowledgments

I am very grateful to Assoc. Prof. Miha Čekada for giving me the opportunity to begin my research work at the Department of Thin Films and Surfaces at the Jožef Stefan Institute. I would like to thank him for the guidance, patience, and understanding that he offered as the supervisor. I would also like to thank Dr. Matjaž Panjan for the guidance, discussions and all of the advice which he provided as the co-supervisor during my doctoral studies.

I would like to thank the members of the Evaluation Board, Assoc. Prof. Janez Kovač, Assoc. Prof. Dean Cvetko and Dr. Zdravko Siketić, for their time and effort invested in the review and evaluation of the dissertation.

I am grateful to the co-workers at the department who helped me to perform experiments: Jožko Fišer for the technical support, Matej Drobnič for making the semicircular substrate holder and collimators, Žan Gostenčnik and Domen Korbar for the measurements of layer thickness and mass change. I am grateful to the department co-workers for all the pleasant coffee breaks, especially to Dr. Peter Panjan for the informative introductory lectures and also for many relaxing conversations we had together with Dr. Aljaž Drnovšek.

I am grateful to Maja Koblar for teaching me SEM microscopy and for stimulating discussions. I am very grateful to Alja Čontala, my doctoral classmate, and Anja Pogačnik Krajnc for all our lunch discussions.

Last but not least, I am very grateful for all the support and encouragement received from my family throughout the period of my Ph.D. – Marko, mami, oči, Uroš and Gregor, you gave me the courage to begin this journey and helped me in every step of the way. Sofija and Klara, you two gave me a new sense and enabled me to look at any situation in a different way.

Finally, I would also like to acknowledge the Slovenian Research Agency for the financial support of the doctoral study.

Abstract

The sputtering yield, the spatial distribution of the sputtered atoms, the energy distribution and the average energy of the sputtered atoms are important for numerous deposition techniques, as they determine the microstructure and the physical properties of the thin films. Using SRIM (Stopping and Range of Ions in Matter) simulations, I investigated the influence of different parameters (surface binding energy, incident ion energy, mass of target atoms) for a numerous set of target materials, relevant to sputtering: B, C; Al, Si; Ti, V, Cr, Cu; Zr, Nb, Mo, Ag; Hf, Ta, W, Au. The incident Ar ion energies ranged from 300 to 1200 eV, both for normal and oblique ion incidence.

The total sputtering yield showed notable trends according to the element position in the periodic table. Group 4 elements exhibited the lowest sputtering yields that increased with group number in periodic table. The angular distribution of sputtered atoms revealed a cosine distribution for transition metals. The oblique ion incidence showed asymmetric distributions at lower ion energies with greater symmetry at higher energies.

We conducted a systematic investigation into the influence of surface binding energy, atomic mass, and ion energy on the total sputtering yield. These parameters were analyzed in relation to analytical equation derived by Sigmund. Due to the differences between the existing analytical model and SRIM simulations, we suggested a new modified equation. Our modification introduced a power fitting parameter, accounting for the non-linear dependency of the sputtering yield on the ion energy. The equation provides reliable estimates for sputtering yields at ion energies up to 1200 eV.

The energy distribution functions (EDFs) of sputtered atoms were investigated for the same selection of elements as the sputtering yields. SRIM simulations of EDFs for transition metals and light elements were compared to the analytical equations for EDFs derived by Sigmund and Thompson and with experimental data from the literature. The simulated EDFs provided realistic results for transition metals but were incorrect for elements lighter than Si. All EDFs exhibited a low-energy peak near one-half of the surface binding energy and a high-energy tail decreasing as E^{-2} . Variations in EDF characteristics, such as peak positions and full width at half maximum (FWHM), were observed concerning atomic number, ion energy, and periodic table group.

An empirical equation for transition metals was established to estimate the average energy from the sputtering yield – the average energies of sputtered atoms are inversely proportional to the sputtering yield, with transition metals exhibiting the highest average energies and group 11 elements displaying the lowest.

Although the thesis is primarily aimed to compare the analytical model and Monte Carlo simulations for sputtering processes we also performed measurements of sputtering yield for Ti, V, Cr, and Cu and compared them with simulated values. Notably, deviations between SRIM simulations and experimental total sputtering yields were most pronounced at lower Ar ion energies. While Cu and Cr demonstrated agreement with simulations above 100 eV, disparities were more significant for V and Ti. Additionally, the differential sputtering yields were measured. The highest differential sputtering yields were observed at 40°–50° angles, decreasing with emission angles.

Povzetek

Razpršitveni koeficient, njegova prostorska porazdelitev, energijske porazdelitve in povprečne energije razpršenih delcev so pomembne za vse tehnike naprševanja, saj določajo mikrostrukturo in fizikalne lastnosti napršenih tankih plasti. Z uporabo simulacij SRIM (Stopping and Range of Ions in Matter) sem preučila vpliv različnih parametrov (površinske vezavne energije, energije vpadnih ionov, mase atomov tarče) na raznolik nabor materialov tarč, ki so pomembni za naprševanje: B, C; Al, Si; Ti, V, Cr, Cu; Zr, Nb, Mo, Ag; Hf, Ta, W, Au. Energije vpadnih Ar ionov smo spreminjali med 300 in 1200 eV, tako za pravokotni kot tudi za poševni vpad ionov.

Razpršitveni koeficient je pokazal odvisnost glede na lego v periodnem sistemu. Elementi v skupini 4 so imeli najnižje razpršitvene koeficiente, ki so s skupino periodnega sistema naraščali. Kotna porazdelitev razpršenih atomov je za prehodne kovine pokazala kosinusno porazdelitev. Pri poševnem vpadu ionov smo pri nižjih energijah ionov opazili asimetrične porazdelitve, pri višjih energijah pa so le-te postale bolj simetrične.

Izvedli smo tudi celovito preiskavo vpliva površinske vezavne energije, atomske mase in energije ionov na razpršitveni koeficient. Vplive teh parametrov smo analizirali glede na Sigmundov analitični model. Zaradi razlik med analitičnim modelom in simulacijami SRIM smo predlagali novo, modificirano enačbo. Naša modifikacija enačbe za razpršitveni koeficient vključuje eksponent, ki upošteva nelinearno odvisnost razpršitvenega koeficienta od energije vpadnih ionov. Tako modificirana enačba zagotavlja zanesljive ocene razpršitvenih koeficientov prehodnih kovin, razpršenih z ioni Ar z energijo do 1200 eV.

Energijske porazdelitve razpršenih atomov smo preučili za enak nabor elementov kot razpršitvene koeficiente v prvem delu. Simulacije SRIM energijskih porazdelitev za prehodne kovine in lahke elemente smo primerjali z analitičnimi enačbami energijskih porazdelitev, ki sta jih razvila Sigmund in Thompson, ter z eksperimentalnimi podatki iz literature. Simulirane energijske porazdelitve so dajale realistične rezultate, vendar za elemente, lažje od Si, niso bile pravilne. Vse energijske porazdelitve imajo nizkoenergijski vrh blizu polovice površinske vezavne energije in visokoenergijski rep, ki se zmanjšuje približno kot E^{-2} . V karakteristikah energijskih porazdelitev, kot sta položaj vrha in polovica širine vrha (FWHM), smo opazili trende glede na atomsko število, energijo ionov in skupino periodnega sistema, v kateri se nahaja element.

Za prehodne kovine smo predlagali empirično enačbo za oceno povprečne energije na podlagi razpršitvenega koeficienta – povprečne energije razpršenih atomov so obratno sorazmerne z razpršitvenim koeficientom, pri čemer prehodne kovine kažejo najvišje povprečne energije, elementi v skupini 11 pa najnižje.

Čeprav je bil cilj doktorske disertacije predvsem primerjava analitičnega modela in simulacij Monte Carlo pri procesih naprševanja, smo naredili tudi meritve razpršitvenega koeficienta za Ti, V, Cr in Cu ter jih primerjali s simuliranimi vrednostmi. Odstopanja med simulacijami SRIM in eksperimentalnimi razpršitvenimi koeficienti so bila najbolj izrazita pri nižji energiji Ar ionov. Medtem ko so se meritve za Cu in Cr ujemale s simulacijami nad 100 eV, so bila odstopanja za V in Ti izrazitejša. Izmerili smo tudi diferencialne razpršitvene koeficiente. Razpršitveni koeficient je za vse izmerjene elemente največji pri 40°–50° in se zmanjšuje z emisijskim kotom.

Contents

List of Figures	xv
List of Tables	xvii
Abbreviations and Symbols	xix
1 Introduction	1
2 Theory of Sputtering	5
2.1 Ion Interactions with Solid Material	5
2.1.1 Development of collision cascades	9
2.1.2 Sputtering of atoms	10
2.2 Analytical Description of Sputtering.....	12
2.2.1 Energy distribution function of sputtered atoms.....	16
2.2.2 Analytical expressions for sputtering yield	17
3 Simulations of Sputtering	21
3.1 Molecular Dynamics Simulations	21
3.2 Monte-Carlo Binary Collision Simulations.....	23
4 Stopping and Range of Ions in Matter (SRIM) Sputtering Simulations	29
4.1 SRIM Setup Parameters and Experimental Data	30
4.2 Collision Cascades in Solid.....	32
4.3 Total and Differential Sputtering Yield Evaluation.....	35
4.4 Energy Distribution Functions and Average Energy	37
4.5 Average Energy of Sputtered Atoms	38
5 Experimental Methods	41
5.1 Sputter Deposition Techniques	41
5.1.1 Diode sputtering	41
5.1.2 Triode sputtering.....	43
5.1.3 Magnetron sputtering	44
5.1.4 Ion beam deposition	47
5.2 Measurement of the Sputtering Yield	48
5.2.1 Measurements of total sputtering yield from target mass change	48
5.2.2 Measurements of differential sputtering yield from film thickness	50
6 Results and Discussion	53
6.1 Total Sputtering Yield	54
6.1.1 Surface binding energy	54
6.1.2 Mass ratio.....	60
6.1.3 Incident ion energy	62

6.1.4	Sputtering under oblique incident angles.....	69
6.2	Differential Sputtering Yield	73
6.2.1	Angular distribution for oblique ion incident angle	78
6.3	Energy Distribution of Sputtered Particles	80
6.3.1	Total energy distribution functions.....	84
6.3.2	Angular energy distribution functions	90
6.4	Average Energy of Sputtered Particles.....	94
6.4.1	Total average energy of sputtered atoms.....	94
6.4.2	Angular average energies of sputtered atoms.....	99
6.5	Measurements of the Sputtering Yield	102
6.5.1	Measurements of the total sputtering yield from target mass change...	103
6.5.2	Measurements of differential sputtering yield from thin film thickness	104
7	Conclusions	111
	References	115
	Bibliography	125
	Biography	127

List of Figures

Figure 1.1: Overview of the processes.....	2
Figure 1.2: Microstructure of growing films.....	3
Figure 2.1: (a) Stopping power as a function of incident particle energy.	8
Figure 2.2: Four processes that can cause an atom to leave a solid.	9
Figure 2.3: (a) Single-knock on regime, (b) the linear cascade regime and (c) the spike..	10
Figure 2.4: Incident and emission angle.....	11
Figure 2.5: (a) Sputtering yield for Ti, Al and W,	12
Figure 2.6: Schematic representation of the collision cascade of binary collisions	13
Figure 2.7: The direction of sputtered atom changes due to the surface binding energy..	15
Figure 2.8: Deviation of trajectories and increase in solid angle.....	15
Figure 2.9: Thompson and Sigmund energy distribution functions	17
Figure 2.10: The α function in dependence on the target-ion mass ratio.	20
Figure 3.1: Sputtering of Pt (111)	22
Figure 3.2: Binary collision	23
Figure 3.3: An example of a collision cascade.....	26
Figure 4.1: SRIM setup window.	31
Figure 4.2: Window during calculations of a sputtering cascade.	32
Figure 4.3: The cross-section of the ion interaction volume.	33
Figure 4.4: The cross-section of the recoiled atom interaction volume	34
Figure 4.5: (a) Maximum depth and (b) maximum width	34
Figure 4.6: Schematic of the geometry in the evaluation of the SRIM data.....	35
Figure 5.1: Schematics of the diode sputtering.....	42
Figure 5.2: First ionization potential	43
Figure 5.3: Schematics of the triode sputtering system.	44
Figure 5.4: Schematic cross-section of a planar magnetron.	45
Figure 5.5: (a) Plasma potential and electric field distribution	45
Figure 5.6: Scheme of ion beam deposition.....	47
Figure 5.7: Sputtering Ti target with Ar ions in the Sputron deposition unit.....	49
Figure 5.8: Experimental set-up.	51
Figure 5.9: Experimental set-up with collimators.....	51
Figure 6.1: Target materials investigated by SRIM.....	53
Figure 6.2: The influence of (a) the displacement energy	54
Figure 6.3: The total sputtering yield SRIM simulations and experimental data.....	56
Figure 6.4: The total sputtering yield SRIM simulations and experimental data.....	57
Figure 6.5: The surface binding energy in dependence on the atomic number:	59
Figure 6.6: The sputtering yield in dependence on the modified surface binding energy:.	60
Figure 6.7: Sputtering yields.....	61
Figure 6.8: The total sputtering yield in dependence on Ar ion energy	63
Figure 6.9: Total sputtering yield in dependence on the ion energy	66
Figure 6.10: Fitting parameter b	67
Figure 6.11: Total sputtering yield in dependence on the ion incidence angle.....	70

Figure 6.12: The sputtering yield at 70° Ar ion incidence	71
Figure 6.13: The total sputtering yield for sputtering under an oblique ion angle.....	72
Figure 6.14: Angular distribution of sputtered metallic elements	73
Figure 6.15: Angular distribution of sputtered light elements.....	74
Figure 6.16: Polar distribution of the differential sputtering yield.....	75
Figure 6.17: Angular distribution of sputtered atoms for selected elements	79
Figure 6.18: (a) Angular distribution of Cr atoms sputtered by Ar ions at 60°.....	79
Figure 6.19: Cross section of collision cascades for sputtering a Cr	80
Figure 6.20: An example of an EDF in (a) logarithmic and (b) linear scale.....	81
Figure 6.21: EDFs for selected elements	82
Figure 6.22: EDFs for selected elements	83
Figure 6.23: EDFs for selected elements	84
Figure 6.24: Normalized EDFs simulated by SRIM	85
Figure 6.25: Low-energy peak in dependence on the atomic number.....	86
Figure 6.26: Comparison between the peak positions.....	87
Figure 6.27: Full width at half maximum (FWHM) of EDFs.....	88
Figure 6.28: The maximum energy of sputtered particles	90
Figure 6.29: Normalized angular EDFs obtained from SRIM simulations	91
Figure 6.30: Angular and total EDFs for Ti bombarded by 600 eV Ar ions.....	91
Figure 6.31: The total average energy of sputtered atoms	95
Figure 6.32: Comparison of the average energies	96
Figure 6.33: Total average energy in dependence on sputtering yield.....	97
Figure 6.34: The average energy (a) and sputtering yield (b) of transition metals.....	98
Figure 6.35: Angular distribution of average energies	100
Figure 6.36: Average energies of sputtered atoms in dependence on emission angle.....	101
Figure 6.37: Sputtering yields of Ti, V, Cr and Cu in dependence on Ar ion energy.....	103
Figure 6.38: Differential sputtering yields	105
Figure 6.39: (a) Photo of a used magnetron source.....	105
Figure 6.40: Normalized differential deposition rate on a semicircular substrate.....	107
Figure 6.41: Differential sputtering yield measurements	108

List of Tables

Table 2.1: Parameters c_i and d_i from Eq. (2.8) for calculation of screened potentials.....	7
Table 2.2: Semi-empirical equations for the total sputtering yield adopted from [58].	19
Table 3.1: Monte Carlo programs [29].	27
Table 6.1: Parameters used for SRIM simulations.	58
Table 6.2: Parameters obtained by fitting the sputtering yield Eq. (6.1).....	63
Table 6.3: Parameters obtained by fitting the sputtering yield Eq. (6.3).....	65
Table 6.4: The experimental and semi-empirical values of the total sputtering yield.....	68
Table 6.5: Fitting parameters for cosine approximation.....	76
Table 6.6: The low-energy peak positions.....	87
Table 6.7: The fitting parameter n	89
Table 6.8: Parameters a and b were obtained when fitting the total average energy	95
Table 6.9: Average energies of sputtered atoms	98

Abbreviations and Symbols

BCA	...	Binary Collision Approximation
E_d	...	displacement energy
EDF	...	Energy Distribution Function
E_{msb}	...	modified surface binding energy
E_{sb}	...	surface binding energy
F_S	...	Sigmund energy distribution
F_T	...	Thompson energy distribution
M_i	...	ion mass
M_s	...	mass of sputtered atoms
N_A	...	Avogadro number
p	...	impact parameter
R	...	particle range
S	...	stopping power function
SBE	...	Surface Binding Energy
T	...	energy transfer
$u(r/a)$...	screened interaction potential
$V(r)$...	interaction potential
Y	...	sputtering yield
Z	...	atomic number
Λ	...	energy transfer factor
σ	...	scattering cross section
Σ	...	stopping cross section

Chapter 1

Introduction

Ion bombardment of surfaces is widely used in various fields of science and technological processes. It is the basis of ion etching and sputtering processes. In ion etching the material is removed from the surface, while in sputtering, the goal is to deposit thin films onto the surfaces.

Ion etching plays a crucial role in various applications and research fields, including materials science, surface analysis, nanotechnology and microelectronics. It is used to remove material and control surface properties, which makes it indispensable in numerous scientific fields and industrial techniques. Ion etching is employed in analytical techniques such as secondary ion mass spectrometry (SIMS), Auger electron spectroscopy (AES) and X-ray photoelectron spectroscopy (XPS) [1, 2]. These techniques involve bombarding the sample surface with ions to sputter and analyze the emitted secondary ions or electrons, providing valuable information about the surface composition, elemental distribution, and chemical bonding. In thin film deposition processes, ion etching is used as a pre-treatment step to clean and prepare the substrate surface before the deposition of thin films. The ions bombarding the surface remove contaminants, oxides, and other impurities, ensuring good adhesion and quality of the deposited films. Ion etching can be used to modify the surface properties of materials, such as creating surface textures, improving wettability, or inducing desired chemical reactions. This is particularly relevant in research areas like surface engineering, biomaterials, and catalysis. Ion etching is extensively used in the fabrication of integrated circuits (ICs) and microelectromechanical systems (MEMS) [3]. It is employed to remove specific layers of materials during device manufacturing, shape structures, create patterns, and define circuit features with high precision. Techniques such as reactive ion etching (RIE) and focused ion beam (FIB) milling are vital for nanofabrication processes [4-6].

Ion etching is also presented in fusion reactors. There, the generation of energy originates from nuclear reactions, which can only be realized at the high temperatures of a plasma. In the common reactor principles, tokamak and stellarator, the plasma is confined in a magnetic field, but cannot be completely retained by the wall. Finding suitable wall materials for the reactor that can withstand high temperatures and bombardment by charged particles is one of the biggest challenges [7-13]. Ion etching also occurs in natural processes in space: the interaction between ions and planetary surfaces is an important process in the solar system that continuously alters the surfaces of many planetary bodies [14].

Sputtering is widely used for depositing thin films. It is a versatile technique capable of depositing a wide range of materials, including metals, oxides, nitrides, and semiconductors. By sputtering a material onto the surface, it can enhance characteristics such as hardness,

wear resistance, and biocompatibility. Deposited films are used in areas like tribology, biomedical implants, protective coatings, microelectronics, solar cells, magnetic storage devices, optical coatings, and more. They are extensively used in the fabrication of integrated circuits and semiconductor devices. Sputtering is employed to deposit thin films for metallization layers, diffusion barriers, contacts, and interconnects. It is also a key process in the production of magnetic recording media used in hard disk drives. Thin films of magnetic materials, such as cobalt alloys, are deposited onto the disk surfaces to create the recording layer. Sputtering is also used in the production of optical coatings for applications such as anti-reflective coatings, mirror coatings, and filters. Using sputtered thin films we can achieve precise refractive index, thickness and layer composition requirements. This enables the production of high-performance optical devices.

These are just a few examples of the diverse applications of sputtering. The technique's ability to deposit thin films with precise control over composition, thickness, and structure makes it essential in numerous research areas and technological applications.

This thesis presents interactions between ions and solids, with a specific emphasis on the sputtering process. When ions impinging on the surface possess kinetic energies in the range between 100 eV and 1 keV, a resulting collision cascade leads to the ejection of atoms from the solid. The collision cascade is initiated as the ion dissipates its energy through multiple collisions, spanning a distance ranging from several nanometers to several tens of nanometers within the solid. The actual distance depends on factors such as the energy and type of the ion, and the type of the solid material.

When an ion with high energy penetrates through a solid material, it causes various processes. In addition to sputtering, an emission of secondary electrons, ion implantation, ion scattering, or heating of the target due to lattice vibrations can occur (Figure 1.1). This thesis focuses only on the process of atom sputtering.

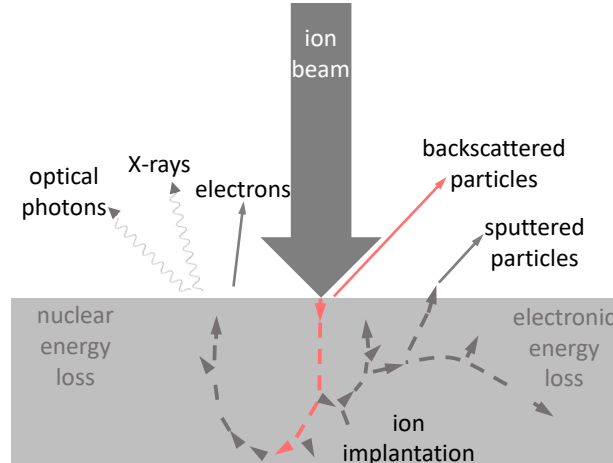


Figure 1.1: Overview of the processes that occur when ions with energies in the 1 keV energy range interact with a solid material.

Sputtering of atoms depends on the type of the material bombarded as well as on the energy, mass and current density of impinging ions and on the angle of ion incidence. For significant sputtering to occur, ions require an energy of at least several 100 eV. Such ions can be obtained from various plasma sources (e.g., ion gun, magnetron). These sources have different energy, spatial distribution and current density of emitted ions.

An ion gun emits a beam of ions generated in the plasma inside the gun [15]. The formation of ions is spatially separated from the processed material. The ions from the ion gun have a well-defined energy, their angle of incidence to the surface is precisely

determined, and the ion flux can be varied over a wide range. Using ion guns, the surface etching is precise but limited to smaller surfaces.

When plasma is generated next to the treated material, a larger surface area can be processed. In such plasma, it is more difficult to independently control the energy of the ions, their flux, and their spatial distribution. The ions are obtained from plasma generated by applying an electrical voltage to the material (i.e., the target to be sputtered) at low pressure of an inert gas (usually Ar). The density of the plasma and the associated ion bombardment of the material depend on the voltage applied to the target, the target material, the type of gas, the pressure, and other parameters of the discharge.

The influence of energetic species on the properties of thin films has been discussed and demonstrated in several works [16-21]. The changes induced by ion bombardment depend not only on the average energy deposited per atom, but also on the ion energy and the ratio between the ion and the deposited particle flux [16]. This indicates that the average energy deposited per atom is not a universal parameter that determines the properties of the deposited thin film. The role of the energetic particles in the microstructure of the thin film is best illustrated by the structure-zone diagram. In recent revisions of the diagram (Figure 1.2), the universal parameters that determine the microstructure are related to the normalized kinetic energy E^* of the impinging particles (i.e., both the ions of the working gas and the sputtered atoms and ions) [22]. The energy emitted by the energetic atoms affects the microstructure by local heating and by displacement of the atoms in the growing layer. In addition to the energy, the direction in which the sputtered atoms hit the substrate also significantly affects the growth of the thin film and its properties. The microstructure is also influenced by the film thickness t^* and by the temperature T^* (Note: modified quantities are used, which are denoted with an asterisk; for an explanation see [22].)

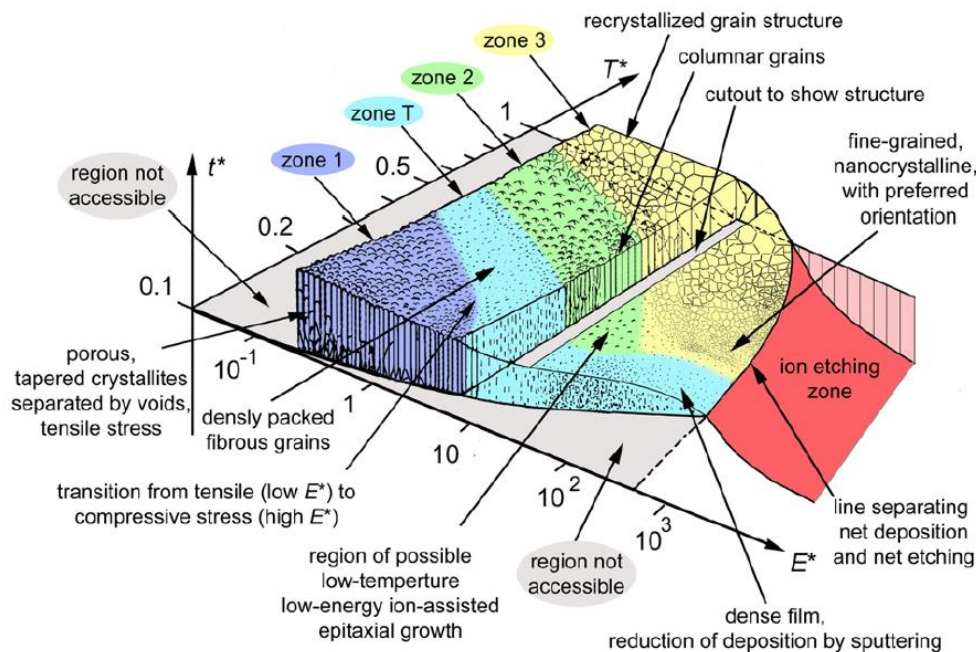


Figure 1.2: Microstructure of growing films is determined by the energy of the sputtered particles and temperature [22].

Good estimates for the number of sputtered atoms per incident ion (called the sputtering yield) and the energy distribution of sputtered atoms are required in thin film deposition for precise control of the thin film thickness, microstructure, texture and other film properties. They are also essential to accurately model sputtering and properties of glow discharges [23-27]. Sputtering yields and energy of sputtered atoms are often necessary

in various techniques, such as semiconductor manufacturing, surface analysis, fusion research, and elsewhere.

In this thesis, we will focus on the physical processes that occur at the atomic level when an ion collides with a solid. Understanding these processes is important for the application of various analytical and sputtering techniques. We will describe in more detail the processes of energy transfer between the incident ion and the sputtered atoms of the target and investigate the influence of various parameters on the number and energy distribution of the sputtered atoms.

This thesis is divided into six chapters. We begin with this Introduction and then follow with Chapter 2, where the theory of the sputtering process and interactions of ions with a solid is introduced along with the analytical calculation approach. In Chapter 3, we elaborate on two different types of simulations – Molecular dynamics simulations and Monte Carlo binary collision simulations. We focus on the Monte Carlo binary collision approach, which was used for calculations in this thesis. The SRIM program, which uses this approach, is briefly described in Chapter 4 along with details of SRIM simulations and the parameter settings used in this thesis. In Chapter 5, we introduce the sputter deposition techniques and the experimental methods applied throughout this thesis. Finally, the results and discussion of sputtering simulations and experiments for relevant target materials are given in Chapter 6. Therein we discuss the sputtering yield, its angular dependence, the energy distributions of sputtered atoms and their angular distribution according to different properties of incident ion and sputtered atoms.

Chapter 2

Theory of Sputtering

This chapter presents the atomic level processes caused by an ion traveling through a solid. The ion energy decreases with each collision. Two types of interactions are described – nuclear and electronic – that affect the energy transfer between the incident particle and the solid. Several types of collision cascades can develop at different energies of the incident ions or at different scattering intersections – the single-knock-on regime, the linear cascade regime, and the spike regime. These collision cascades can lead to particle sputtering when they reach the surface. The influence of the incident ion energy and angle of incidence on the final number of sputtered particles is shortly outlined. The analytical model of Sigmund and Thompson, most commonly used in sputtering research, is also briefly presented. The energy distribution function and the sputtering yield equations are explained along with the main assumptions and models used in the final solution.

2.1 Ion Interactions with Solid Material

The ions with kinetic energy between 100 eV and several thousands of eV can cause a collision cascades that result in sputtering of atoms from a solid. These collision cascades are initiated as the ions gradually dissipate their energy through nuclear collisions that occur over a range of several nanometers to tens of nanometers. The actual range depends on the specific properties of the ion type and its initial energy.

Before an ion collides with a solid it can be neutralized and become an atom. As positive ion is near the surface of a solid, a very strong electric field is created between the ion and the surface. This field reduces the barrier to electron tunneling, allowing the electron to neutralize the ion. The process is called Auger neutralization [28]. In such case, interaction in the material occurs between the incident atom and the solid.

A momentum and kinetic energy of a particle (ion or atom) are affected by various types of interactions when it enters a solid material. In general, interactions occur between the nucleus of the particle and the nuclei of the atoms in the solid, and between the electrons of the particle and the free and bound electrons of the solid [29-31]. The first type of interactions are elastic interactions, while the others are inelastic. Both types of interactions cause the penetrating particle to lose kinetic energy and change its direction of motion in the solid.

The energy losses of a penetrating particle are described by the stopping power S , which is defined as the particle's energy loss E per unit of traveled path x [32]:

$$S(E) = -\frac{dE}{dx}. \quad (2.1)$$

Another quantity, which describes the stopping of particles in the solid, is the stopping cross section:

$$\Sigma = \frac{1}{\rho} \left(-\frac{dE}{dx} \right), \quad (2.2)$$

where ρ is the target density. Stopping cross section is equal to stopping power S divided by target density [32]. On the other hand, the stopping cross section is related to the energy transfer T as:

$$\Sigma = \int T d\sigma(T), \quad (2.3)$$

where σ is the scattering cross section and T is the energy transfer, defined as:

$$T = E \frac{M_s M_i}{(M_s + M_i)^2} \cos^2 \phi. \quad (2.4)$$

Here, ϕ is the scattering angle of the recoil, M_s is the target atom mass and M_i is the mass of the ion.

The scattering cross-section can be evaluated from differential cross-sections as:

$$\frac{d\sigma(\theta)}{d\omega} = \frac{p}{\sin \theta} \left| \frac{dp}{d\theta} \right|, \quad (2.5)$$

where ω is the solid angle, p is the impact parameter and θ is the scattering angle in the central mass system.

The energy transfer T and the scattering cross section are determined by the scattering angle in the elastic collision, which can be calculated as:

$$\theta = \pi - 2p \int_{r_{\min}}^{\infty} \frac{dr}{r^2 \sqrt{1 - \frac{V(r)}{E_{\text{cms}}} - \left(\frac{p}{r}\right)^2}}, \quad (2.6)$$

where r is the distance between two particles involved in the collision, r_{\min} is the distance of the closest approach between them, E_{cms} is the energy in the central mass system and $V(r)$ is the interaction potential. Using pure Coulomb potential, Eq. (2.6) gives the Rutherford cross section [33]. This is a result for light ions with energies in the MeV range. In the keV energy range, which is used in thin film deposition, the screened Coulomb potential is required because the electron shells of the atoms cannot be neglected. In this potential, the colliding atoms are separated far enough between each other and the positive charge of the nuclei is at least partially compensated by the negative charge of the electrons. These screened Coulomb potentials can be written as follows:

$$V(r) = \frac{1}{4\pi\epsilon_0} \frac{Z_s Z_i e^2}{r} u \left(\frac{r}{a} \right). \quad (2.7)$$

Here, Z_s and Z_i are the atomic numbers of the particles involved and a is the screening length. The screening length determines above which distance the electrons screen the electric field of the protons in the nucleus. The most commonly used potentials $u(r/a)$ can be generally written as:

$$u\left(\frac{r}{a}\right) = \sum_{i=1}^n c_i \exp\left(-d_i \frac{r}{a}\right). \quad (2.8)$$

The values for c_i and d_i are presented in Table 2.1 for the most commonly used potentials. The Moliere potential is an empirical fit to the Thomas-Fermi function [34]. Kr-C potential describes the interaction between Kr and C atoms [35]. It has been shown that this potential describes well also other atom-atom collisions [36]. The ZBL (Ziegler-Biersack-Littmark) potential was determined as the average potential calculated from many individual combinations of impinging ions and sputtered materials [37].

Table 2.1: Parameters c_i and d_i from Eq. (2.8) for calculation of screened potentials.

	Bohr [38]	Moliere [34]	Kr-C [35]	ZBL [37]	Lenz-Jensen [39, 40]
n	1	3	3	4	3
c_1	1	0.35	0.190945	0.028171	0.01018
c_2	0	0.55	0.473674	0.28022	0.24330
c_3	0	0.10	0.335381	0.50986	0.7466
c_4	0	0	0	0.18175	0
d_1	1	0.3	0.278544	0.20162	0.206
d_2	0	1.2	0.637174	0.40290	0.3876
d_3	0	6.0	1.919249	0.94229	1.038
d_4	0	0	0	3.1998	0

Nuclear interactions, which are elastic, result in a localized loss of energy since the interactions are significant only when the moving particle comes very close to the atomic nuclei in the solid. The interaction is described by the nuclear potential between the nuclei of the penetrating particle and the atom of the solid. In elastic interactions, the momentum and kinetic energy of the particles involved in the collision change significantly, while the total momentum and energy of the system are conserved. In elastic collisions, a large part of the energy of the incident particle is transferred to the atoms in the solid, and the atoms in the crystal structure can therefore leave their equilibrium position and move through the solid and collide with other atoms. Elastic collisions between nuclei are the main mechanism that causes the sputtering of atoms.

Electronic interactions are inelastic and can be divided into local and continuous energy losses. Continuous energy losses result from the interaction between electrons of penetrating ion/atom and free electrons in the solid (Fermi gas in metals), while local energy losses are affected by bound electrons in the solid. In the inelastic type of interaction, the energy losses are proportional to the velocity of the particle (or the square root of the energy of the moving particle). Thus, this type of reduction in the particle energy is continuous (or linear) because it occurs continuously as the particle travels through the solid. In continuous inelastic energy loss, the penetrating particle loses energy, but its direction of motion does not change. Local energy losses occur due to the interaction between the electrons of the moving particle and the bound electrons in the material and are more significant at very high energies of the incident particle (i.e., greater than 10 keV). In these interactions, ionization and excitation of electrons in the solid and in the

penetrating particle occur. In contrast to the continuous losses, these energy losses are localized because they occur when the two electron clouds of the particles overlap.

The stopping power depends on the energy and type of the incident particle, as well as on the solid through which the ion penetrates. The stopping power is determined experimentally and theoretically for various combinations of ions and solid materials [37]. The stopping power can be divided into the nuclear stopping power (S_n) and the electronic stopping power (S_e):

$$S(E) = S_n(E) + S_e(E). \quad (2.9)$$

From the dependence of the stopping power on the energy, the range R which a particle with the initial kinetic energy E_0 reaches in the solid can be determined:

$$R = \int_0^{E_0} \frac{1}{S(E)} dE. \quad (2.10)$$

Figure 2.1(a) shows the electronic and total stopping power for the penetration of Ar ions through transition metals and some light elements. The range of energies up to 1200 eV is shown. In this energy range, the energy of the particle is mainly influenced by nuclear interactions, while the influence of electronic interactions is much lower, but not completely negligible. An Ar ion with an energy of 1000 eV loses on average about 415 eV when it travels 1 nm in Ti, of which 370 eV is lost due to nuclear interactions and 45 eV due to interactions between electrons. Energy losses due to electron interactions are an order of magnitude lower than those due to nuclear interactions. The influence of electronic interaction increases with the decreasing energy of the penetrating ion.

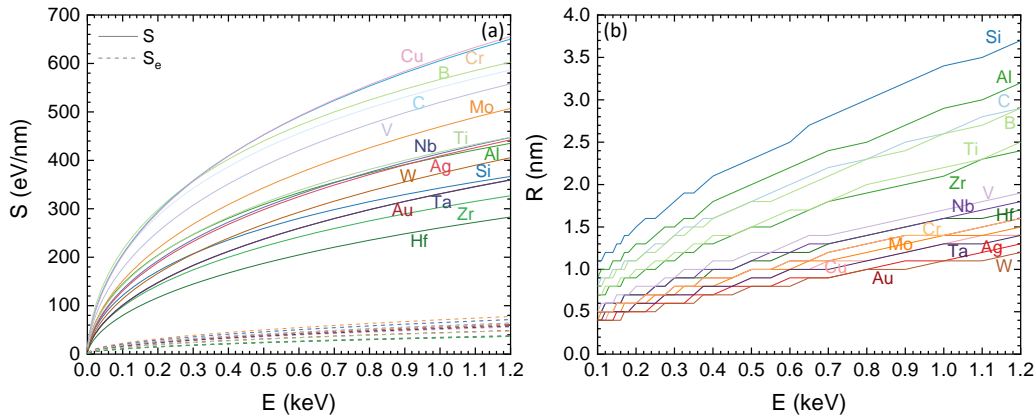


Figure 2.1: (a) Stopping power as a function of incident particle energy. The graph shows the electron (S_e) and the total stopping power (S) for the penetration of Ar ions through different solid materials. (b) The range R that Ar ions with a given incident energy can travel inside a solid. The values were taken from the tables of the SRIM program [37]. In the left part of the chart (b) the values are discrete because in the the SRIM program only discrete values are tabulated.

Figure 2.1(b) shows the range of Ar ions in chosen materials. An Ar ion with an energy of 1000 eV travels about 2 nm, and with an energy of 500 eV about 1.5 nm in Ti solid. In direct magnetron sputtering, Ar ion energies are typically below 400 eV, which means that Ar ions penetrate only a few atomic layers deep. In general, lighter ions penetrate deeper

into the solid than heavier ions with the same energy, but they sputter less material. The graph in Figure 2.1(b) is step-like because the values were taken from the SRIM program, where only discrete values are tabulated.

As an ion travels through the solid, it transfers its kinetic energy to the atoms in the solid. Some atoms, especially those near the surface of the solid, can gain enough energy through the first collision or through several successive collisions to leave the solid. We will describe this process in more detail in the next section.

2.1.1 Development of collision cascades

An ion traveling through a solid causes a set of collisions that are described as collision cascades. The kinetic energy of the ion is transferred by collisions between the ion and atoms in the solid – this is called the primary collision cascade. When the collision of an ion with an atom causes further collisions of that atom with other atoms in the solid, a secondary collision cascade forms. Tertiary and higher orders of cascade collisions can be formed by further collisions of the recoiled atoms.

Figure 2.2 shows several possible cases that can lead to the ejection of an atom from a solid. Primary ejected atom is the atom sputtered directly after collision with the incident ion. Secondary knocked out atoms (or higher order knocked out atoms) are atoms sputtered after the collision cascade is developed – one of the recoiled atoms knocks out another atom. Similarly, we can characterize those sputtered atoms where the incident ion is reflected towards the surface due to collisions (i.e., backscattered ion).

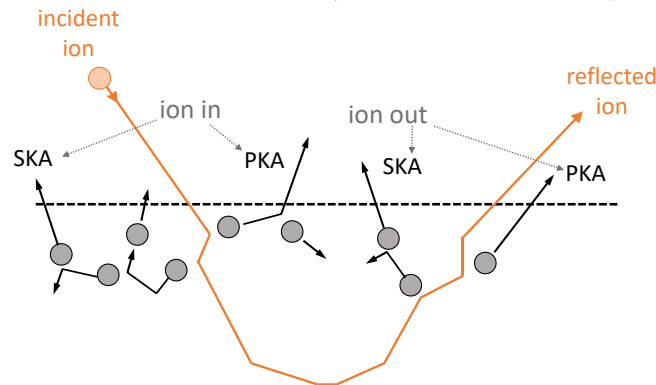


Figure 2.2: Four processes that can cause an atom to leave a solid. We distinguish between primary (PKA) and secondary knocked-out atoms (SKA) or knock out higher-order atoms when multiple indirect collisions are involved (adopted from [29]).

Several collision regimes can generally be distinguished, depending on the energy of the incident ions and the scattering cross-sections. The boundaries between them are not clearly defined [41, 42]. For light ions and/or lower energy heavier ions, the incident ion scatters off the atoms in the solid several times or only once (Figure 2.3a). If the ion is directed back towards the surface, it can knock the atom out of the material, and the energy transferred must be greater than the surface binding energy of the atom (typically a few eV). This sputtering process is called the *single-knock on regime*. Secondary cascades usually do not develop in this regime. This sputtering regime is important when ion energies are below 1 keV, but it becomes more important with larger ion incident angles [43]. In sputtering processes, most ions are directed perpendicularly to the surface, and the ion energies are below 1 keV. It is also important in the sputtering with an ion gun, where the

energies are usually higher (several keV), but the samples are usually sputtered at larger angles of incidence.

At higher energies and/or heavier ions, the most important regime is the *linear cascade regime* (Figure 2.3b). In this regime, the incident ions have enough energy to displace several atoms from their equilibrium positions, and these atoms then collide with other atoms in the solid. Therefore, secondary collision cascades and cascades of higher orders are formed. For this regime, the density of the colliding atoms is low enough that only two particles are involved in the collision at the same moment – the one that is moving and the other that is at rest before the collision in the solid. It is assumed that the thermal fluctuations of the atoms in the crystal lattice can be neglected and also the collision between moving atoms can be neglected. This regime therefore consists of a consecutive series of binary collisions between a moving particle and a stationary particle in a single cascade. In this mode of sputtering, the sputtering yield is proportional to the energy of the incident ion, therefore it is also called the linear regime. This sputtering regime is typical for the energy range from around 1 keV to about 1 MeV.

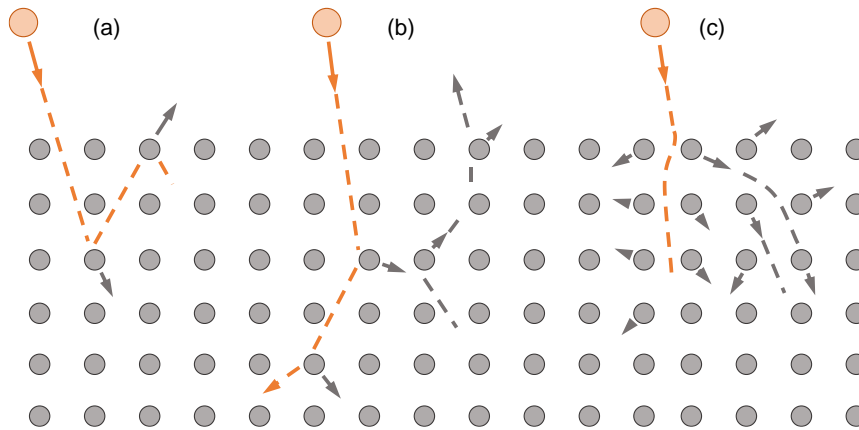


Figure 2.3: (a) Single-knock on regime, (b) the linear cascade regime and (c) the spike regime. Adapted from [17].

When a solid is bombarded by heavy ions that have a large scattering cross section or with larger molecules, the density of recoiled atoms can be so high that most atoms within the sputtering volume are in motion (Figure 2.3c). This regime is characterized by non-linear processes, it is called the *spike regime*. It differs from the linear regime since binary collisions occur between two moving particles, while in the linear regime, the collisions occur exclusively between one moving particle and another stationary particle. The nonlinear regime is similar to the evaporation of a solid, or more specifically, sublimation, since most atoms within a small volume leave the solid in a very short time.

In the following section, we will focus on collisions that take place in the single knock-on regime and in the linear cascade regime, as these are the dominant regimes for most sputter deposition and ion etching techniques.

2.1.2 Sputtering of atoms

Sputtering describes an emission of atoms from the surface of a solid when impacted by energetic particles, typically ranging from a few electron volts (eV) to several megaelectron volts (MeV) [41]. In this process, shown in Figure 1.1, a collision cascade forms near the surface of the material when energy of ions is below 1 MeV. In order for sputtering to

occur, the atoms within the target must receive enough energy to displace them from their bounded lattice position. The energy needed for this is called the displacement energy (E_d) and is typically in the range of tens of electron volts (eV). Additionally, the recoiled atoms must have sufficient energy to overcome the surface binding energy (E_{sb}), which is often not precisely determined and is typically approximated by the sublimation enthalpy, which is a few eV. These conditions establish a threshold energy range for the so-called kinetic sputtering, typically in the range of tens of electron volts (eV) [41].

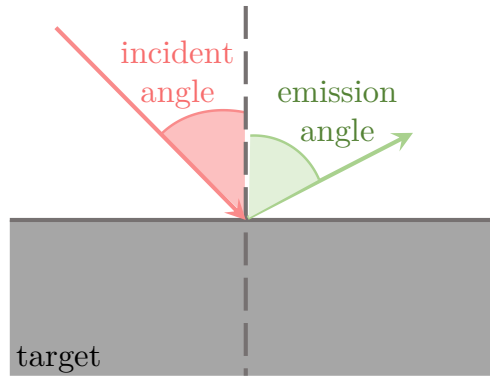


Figure 2.4: Incident and emission angle.

The average number of sputtered atoms per incident ion is called a sputtering yield. It is defined as the ratio between the number of sputtered atoms N_s and the number of ions impinging on the solid N_i :

$$Y = N_s / N_i. \quad (2.11)$$

The number of atoms sputtered from the target depends on the energy, mass and incident angle of the ion, as well as on the properties of target material. Regarding energy dependence, the sputtering yield initially increases with energy as more energy is transferred to the recoiling atoms. Maximum sputtering yield is typically achieved at energies in the range of a few keV to several tens of keV. Beyond this range, the increased energy cannot compensate for the shorter interaction times and longer penetration range of the ions, so less energy is deposited near the surface. The dependence on the angle of incidence (see Figure 2.4) results from the shorter range of ions at oblique incidence, bringing the collisional cascade closer to the surface. Established fitting formalisms take into account that at incidence angles of about 60° or more, ion reflection becomes more frequent, leading to a decrease in sputtering yield [44]. Figure 2.5 shows an example of the energy (a) and angular dependence (b) of the sputtering yield (Y) for Ar ions sputtering an Al, Ti and W target, obtained by SRIM simulations [37]. The inset of Figure 2.5a shows the sputtering yields for those three elements in the energy range, typical for deposition techniques. The sputtering yield dependence on Ar incident angle for the sputtering Ti target reaches the maximum values between 70° and 80° angle for the 300–2000 eV energy range. The difference between the minimum and maximum values of sputtering yield between different incident angles increases with ion incident energy.

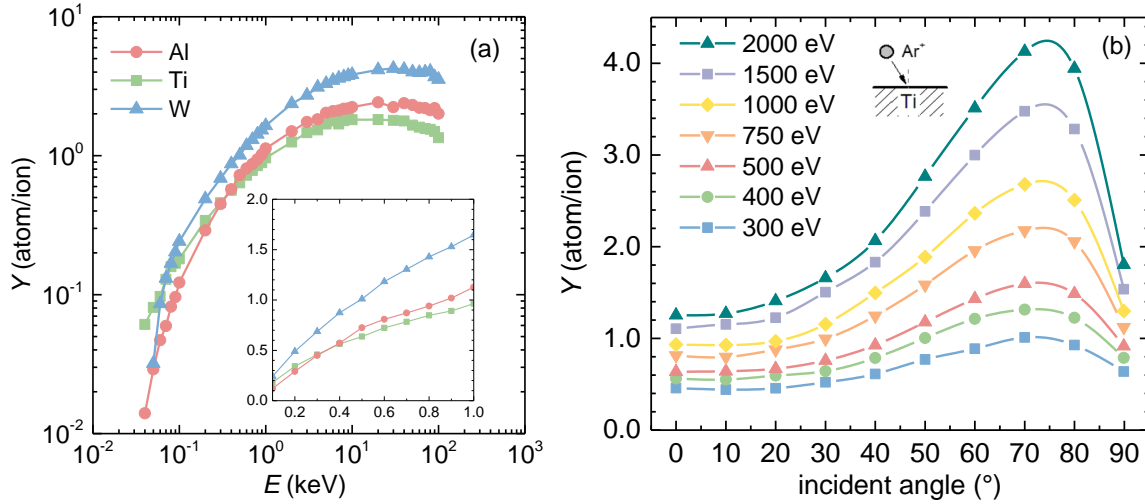


Figure 2.5: (a) Sputtering yield for Ti, Al and W, as a function of the Ar ion energy. The inset graph shows the sputtering yields for the energy range up to 1000 eV in a linear scale. (b) Sputtering yield of Ti as a function of the angle of Ar ion incidence for different energies. All sputtering yields were calculated using SRIM simulation program [37].

2.2 Analytical Description of Sputtering

The theory of sputtering was first presented by M. W. Thompson in 1968 [45]. A year later P. Sigmund published his theory of sputtering [46]. Sigmund theory is a statistical approach, treating sputtering as a probabilistic process where ions interact with target atoms which leads to ejection of atoms. The theory considers the ion energy, mass, charge, and angle of incidence, as well as the target material atomic properties. The theory developed by Sigmund has been widely used to predict sputtering yields and energy distribution of sputtered atoms for a range of ion-target combinations and has provided valuable insights into the sputtering phenomenon.

Thompson sputtering theory also provides insights into the fundamental mechanisms of sputtering and has been used as a basis for understanding the sputtering process in various experimental contexts. In this model, the sputtering is influenced by a wide range of factors, including ion energy, angle of incidence, target material properties and others.

Despite some differences between the two approaches, the general description of sputtering and the results of the two theories are similar [47]. For example, in the literature, an energy distribution function of sputtered atoms is often called the Sigmund-Thompson distribution, which can be justified based on the similarities of the two functions for the most part of the energy distribution. We will introduce the Thompson theory of sputtering and discuss the differences between the two approaches at the end of this chapter.

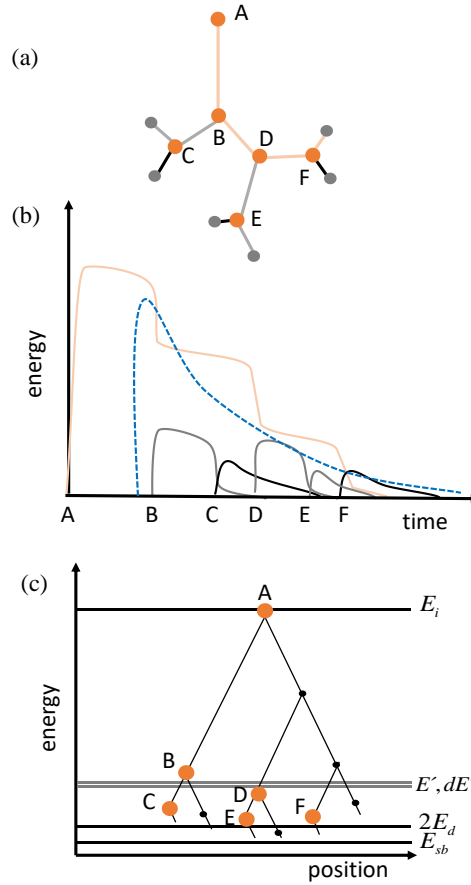


Figure 2.6: Schematic representation of the collision cascade of binary collisions (a). The letters A, B, C, D, E, and F denote the locations of the collisions. Graph (b) shows the kinetic energy of each particle as a function of time and the average energy of the atoms involved in the collisions. Diagram (c) shows the energies of particles after each collision. The figures (a-c) were adopted from [48].

Thompson model of sputtering assumes a linear collision regime, i.e., each ion causes a series of binary collisions and the recoiled atoms generate new collisional cascades. The cascade process ends when the atoms cannot be removed from its equilibrium position. This is the case when the incident particle has an energy less than $2E_d$, where E_d is the displacement energy – i.e., the threshold energy to move the atom from its equilibrium position. The number of atoms participating in the collision cascade and permanently displaced from their equilibrium position is on average equal to [49]:

$$N_d = \frac{E_i}{2E_d}, \quad (2.12)$$

where E_i is the energy of the particle (ion or recoil atom) that causes the formation of the cascade.

Figure 2.6a shows the cascade process of the sequence of collisions between the atoms, labeled as A, B, C, D, E, and F. The trajectory of the incident ion or the first observed atom in the solid that has the energy E_i is marked in orange. The gray color indicates the trajectories of atoms that have gained enough energy through collision with an incident ion to move from their equilibrium position and collide with other atoms (secondary trajectories). The trajectories after the third-order collision are marked in black. A schematic representation of the kinetic energy of the particles as a function of time is shown in Figure 2.6b, where the blue dashed line indicates the average energy of the recoiled

atoms involved in the collisions. Figure 2.6c shows the energy diagram of this collision cascade. The vertical axis represents the kinetic energy of the atoms, while the horizontal axis indicates their position.

Due to a large number of collisions between particles, the sputtering can be considered statistically. Following the Thompson procedure described in [48], the velocity or rate at which particles enter the energy interval between E' and $E'+dE'$ due to collisions is on average proportional to $1/E'$. Particles spend time dt in the energy interval dE' , and the density of atoms at each time is proportional to dt/E' . The deceleration time (dt) is related to the stopping power from Eq. (2.1). The energy loss of the particle per unit time is proportional to the stopping power dE'/dt , the linear rate of energy loss as:

$$\frac{dE'}{dt} = v \frac{dE'}{dx}, \quad (2.13)$$

where the velocity of the particle is $v=dx/dt$ and E' is its kinetic energy. It follows from the above equation that the deceleration time is:

$$dt = \frac{dE'}{v(dE'/dx)}. \quad (2.14)$$

In the energy range typical for sputtering techniques (i.e., 100–1000 eV), the stopping power (i.e., the energy loss per unit distance traveled) is approximately proportional to the energy E' . Thus, we can write:

$$\frac{dE'}{dx} = K \frac{E'}{\lambda}, \quad (2.15)$$

where we have taken into account that the particle travels on average a length λ equal to the average distance between atoms in the solid, and K is a constant. Combining equations (2.14) and (2.15), we obtain:

$$dt = \frac{(\lambda/K)dE'}{vE'}. \quad (2.16)$$

The particle flux j through a given surface inside the solid is calculated by the product of the particle velocity v and the number of atoms, which is proportional to dt/E' . Thus, if we calculate the product vdt/E' and consider Eq. (2.16), we can write the particle flux as follows:

$$\phi(E')dE' = \frac{(\lambda/K)dE'}{E'^2}. \quad (2.17)$$

The above equation represents the flux of particles propagating inside the solid, however we are interested in the number of particles leaving the solid. As particles cross the surface, the atoms must also overcome the surface binding energy. When the cascade reaches the surface of the target, an atom near the surface can leave the material. This occurs when the atom receives an energy larger than the surface binding energy E_{sb} .

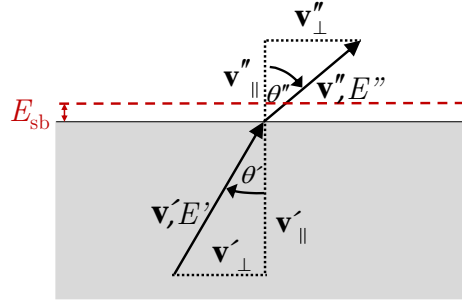


Figure 2.7: The direction of sputtered atom changes due to the surface binding energy E_{sb} .

When passing across the surface, the direction of the sputtered atoms refracts from the normal due to the surface binding energy (Figure 2.7). For an atom leaving the surface of a solid, the following relations must hold [41]:

$$E'' \cos^2 \theta'' = E' \cos^2 \theta' - E_{sb} \quad (2.18)$$

$$E'' \sin^2 \theta'' = E' \sin^2 \theta', \quad (2.19)$$

where E' and E'' are the kinetic energies of the atom inside and outside the solid, respectively, while E_{sb} is the surface binding energy. The θ' and θ'' are corresponding polar angles inside and outside the solid. The energy of the sputtered atom is reduced by the surface binding energy when the atom crosses the surface of the solid, i.e., $E'' = E' - E_{sb}$.

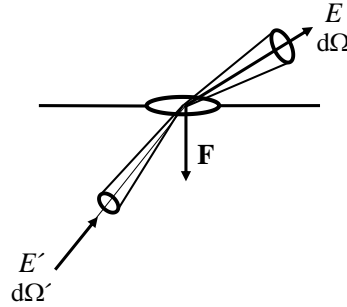


Figure 2.8: Deviation of trajectories and increase in solid angle as atoms pass through the surface. As the atoms pass through the surface, one can imagine a force \mathbf{F} acting in a direction perpendicular to the surface due to the surface binding energy.

In Figure 2.8, the surface binding energy is shown as a force acting on the atoms in a direction perpendicular to the surface. The action of this force causes the trajectories to deflect away from the normal (toward the target surface, as determined by Eq. (2.18) and Eq. (2.19)). In addition to the deflection trajectory of the particles, the solid angle $d\Omega'$ inside the solid changes to a larger solid angle $d\Omega$ as it passes through the surface. The flux of the sputtered particles is therefore equal to [48]:

$$\phi(E)dEd\Omega = \frac{L\lambda EdEd\Omega}{(E + E_{sb})^3}, \quad (2.20)$$

where L is a constant containing the scattering cross section for ion-atom collisions and the density of atoms of the solid. In the limiting case, when the energy of the sputtered

atom is much higher than the surface binding energy (i.e., $E \gg E_{sb}$), we obtain Eq. (2.17) from Eq. (2.20). These equations show only a part of Thompson's derivation, more detailed description of the derivation can be found in [45, 48].

2.2.1 Energy distribution function of sputtered atoms

The Thompson procedure described in the previous section provides insight into the fundamental mechanisms of sputtering and gives the energy distribution of sputtered particles which depends on several parameters. In its final form, the Thompson energy distribution is described as follows:

$$F_T(E) = A_T \cdot \frac{E}{(E + E_{sb})^3} \left(1 - \sqrt{\frac{E + E_{sb}}{\Lambda E_i}} \right) \quad \text{for } E + E_{sb} \leq \Lambda E_i. \quad (2.21)$$

The equation is valid for atom energies up to the maximum transferable energy (i.e. $E_{\max} = \Lambda E_i$). In the above distribution, E is the energy of the sputtered atoms, A_T is the normalization constant, and Λ is the energy transfer factor calculated as:

$$\Lambda = \frac{4M_s M_i}{(M_s + M_i)^2}. \quad (2.22)$$

The energy distribution of sputtered atoms was presented independently in the same year by Peter Sigmund [46]. Sigmund arrived to a similar equation as Thompson. In its simplest form, Sigmund expression for the energy distribution of sputtered atoms is (see e.g. [31] Eq. (7)):

$$F_S(E) = A_S \frac{E_{sb} E}{(E + E_{sb})^3}. \quad (2.23)$$

The full expression can be found in Chapter 2 of Ref. [41] (see Eq. 2.3.16b) and is further discussed by Sigmund in Ref. [50].

Note that Thompson Eq. (2.21) and Sigmund Eq. (2.23) are similar but not entirely identical (see Figure 2.9). In general, both distributions have comparable shapes with a peak close to $E_{sb}/2$ and an energy tail, which decreases as $1/E^2$. Nevertheless, there are a few notable differences between the two distributions. The Thompson distribution includes an additional factor $\sqrt{(E + E_{sb})/\Lambda E_i}$. This factor influences only the tail of the distribution but not the low-energy part since $\Lambda E_i \gg E + E_{sb}$ for energies near the peak of EDF. The factor $\sqrt{(E + E_{sb})/\Lambda E_i}$ causes the energy tail to curve toward zero when atom energies approach the maximum energy ($E_{\max} = \Lambda E_i$). The Sigmund distribution on the other hand does not include such curvature of the function near the end of the energy tail. The Thompson distribution appears to provide a more detailed description of EDF of sputtered atoms.

However, the Thompson distribution does not contain a surface binding energy in the numerator, which is a part of the Sigmund distribution (i.e., $E_{sb} E / (E + E_{sb})^3$). In the Thompson distribution, the parameters related to the sputtered material and impinging ion are included in the constant A_T (the constant is specified in Eq. (19) in the original

paper of Thompson [45]). It should be emphasized that the Sigmund distribution does not depend on the energy of the impinging ion whereas in Thompson distribution, the ion energy affects only the tail of the distribution (i.e., $\sqrt{(E + E_{\text{sb}})/\Lambda E_i}$).

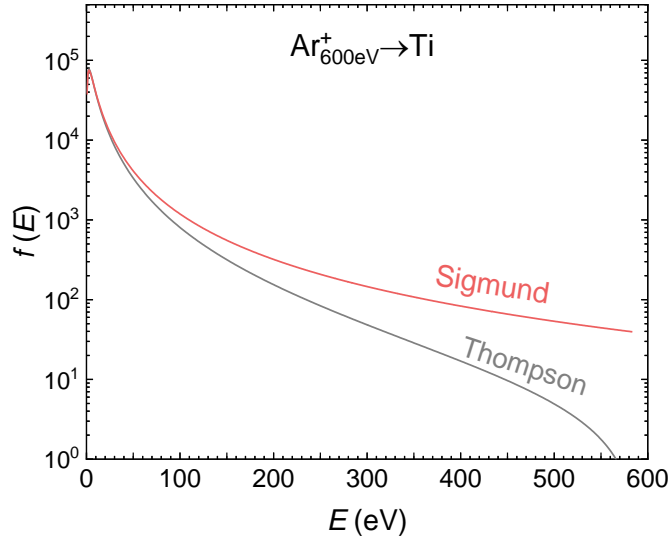


Figure 2.9: Thompson and Sigmund energy distribution functions for sputtering Ti target with 600 eV Ar^+ ions.

Despite several differences between the two distributions, the general shape of the two distributions is similar except near the energy tail. Both authors suggested adding a cosine factor to the total EDF to obtain the angular EDF; this is based on the assumption that the angular distribution of recoils is isotropic [51].

2.2.2 Analytical expressions for sputtering yield

As we mentioned before, the sputtering yield is defined as the number of sputtered atoms N_s per incident ion N_i :

$$Y = N_s / N_i. \quad (2.24)$$

The sputtering yield depends on several parameters that are related to the impinging ion and the sputtered target material. An insight into the influence of these parameters can be obtained from the analytical model of sputtering. For a perpendicular ion impact in the linear cascade regime, Sigmund derived the following expression for the total sputtering yield [46]:

$$Y = \frac{3}{4\pi^2} \frac{2\alpha}{\pi\lambda_0 a^2 E_{\text{sb}}} \Sigma_n \approx 0.042 \frac{\alpha}{E_{\text{sb}}} \Sigma_n, \quad (2.25)$$

where the dimensionless parameter $\lambda_0 = 24$ and a is the screening length (Sigmund used the value 0.219 \AA). α is a dimensionless function, which depends on the ion-target atomic mass ratio and the ion incidence angle, but it does not depend on the ion energy. In Eq. (2.25), the nuclear stopping cross section Σ_n is a complex function of the ion and the target atomic masses and the ion energy:

$$\Sigma_n = 4\pi a_i \frac{e^2}{4\pi\epsilon_0} Z_i Z_s \frac{M_i}{M_i + M_s} s_n, \quad (2.26)$$

with Z and M corresponding to the ion atomic number and mass (index i) and the solid atomic number and mass (index s), respectively. The a_i factor is the Lindhard screening length. Further complexity in Eq. (2.26) arises from the reduced nuclear stopping power s_n . In practice, different forms of the reduced nuclear stopping power are used, which are based on the particular interatomic potential between the interacting atoms. Often a Thomas–Fermi or krypton–carbon potential is utilized [52]. Note that the numerical factors in Eqs. (2.27) and (2.28) originate from nuclear interaction modelling. For the Thomas–Fermi potential, the reduced nuclear stopping power is:

$$s_n^{TF} = \frac{3.441\sqrt{\epsilon} \ln(\epsilon + 2.718)}{1 + 6.35\sqrt{\epsilon} + \epsilon(6.882\sqrt{\epsilon} - 1.708)}, \quad (2.27)$$

while for the krypton–carbon potential, it is:

$$s_n^{KC} = \frac{0.5 \ln(1 + 1.2288\epsilon)}{\epsilon + 0.1728\sqrt{\epsilon} + 0.008\epsilon^{0.1504}}, \quad (2.28)$$

where the reduced energy ϵ is defined as:

$$\epsilon = \frac{a_i}{Z_i Z_s} \frac{4\pi\epsilon_0}{e^2} \frac{M_s}{M_i + M_s} E_i. \quad (2.29)$$

The nuclear stopping cross section Σ_n is the only term in Eq. (2.25) which depends on the ion energy (E_i).

Over the years, the general equation for the total sputtering yield has been modified to achieve a better agreement with the experimental data (particularly at lower ion energies). An overview of various semi-empirical equations for the total sputtering yield can be found in Table 2.2. Several authors have performed different modifications to Eq. (2.25). Bohdansky [53] and Yamamura [54] introduced corrections for low-energy sputtering using very light or heavy ions (also at grazing incident angles). The correction factor that they introduced decreased the sputtering yield near the threshold energy. Eckstein *et al.* [44] proposed a different empirically based correction factor for low-energy sputtering, whereas Wilhelm [55] considered sputtering near the sputtering threshold by employing the quantum statistical approach of three-body sputtering. In the latest attempt, Shang *et al.* [56] included a factor that is related to electronic energy loss for low-energy sputtering. They modified the equation of Zhang [57], which is based on Yamamura’s semi-empirical formula.

Table 2.2: Semi-empirical equations for the total sputtering yield adopted from [58].

Name	Original monatomic formula	Generalized formula	Free parameters
Sigmund	$Y = 0.042 \frac{\alpha}{E_{sb}} \Sigma_n$	$Y = Q S_n$	Q
Bohdansky	$Y = 0.042 \frac{\alpha R_p}{E_{sb} R} \Sigma_n \left[1 - \left(\frac{E_{th}}{E} \right)^{\frac{2}{3}} \right] \left[1 - \frac{E_{th}}{E} \right]^2$	$Y = Q \Sigma_n \left[1 - \left(\frac{E_{th}}{E} \right)^{\frac{2}{3}} \right] \left[1 - \frac{E_{th}}{E} \right]^2$	Q, E_{th}
Yamamura	$Y = 0.042 Q \frac{\alpha^*}{E_{sb}} \frac{\Sigma_n}{1 + \Gamma k_c \epsilon^{0.3}} \left[1 - \sqrt{\frac{E_{th}}{E}} \right]^3$	$Y = Q \Sigma_n \left[1 - \sqrt{\frac{E_{th}}{E}} \right]^3$	Q, Σ_n, E_{th}
Eckstein	$Y = 0.042 Q \Sigma_n \frac{\left(\frac{E}{E_{th}} - 1 \right)^\mu}{\frac{\lambda}{(\epsilon + 0.1728 \sqrt{\epsilon} + 0.008 \epsilon^{-0.1504})} + \left(\frac{E}{E_{th}} - 1 \right)^\mu}$	$Y = Q \Sigma_n \frac{\left(\frac{E}{E_{th}} - 1 \right)^\mu}{\frac{\lambda}{(\epsilon + 0.1728 \sqrt{\epsilon} + 0.008 \epsilon^{-0.1504})} + \left(\frac{E}{E_{th}} - 1 \right)^\mu}$	Q, λ, μ, E_{th}
Wilhelm	$Y = \frac{h_{2/1}}{24} \frac{\sigma(E_{th})}{E_{th}^2} N^{2/3} \left(\frac{M_s/M_j}{1 + 2M_s/M_j} \right)^{3/2} (E - E_{th}^2)$ <small>$h_{2/1}$ dimensionless coefficient</small>	$Y = Q \left(\frac{E}{E_{th}} - 1 \right)^2$	Q, E_{th}

The general sputtering yield equation, Eq. (2.25), should provide the most accurate data for the total sputtering yields; however, it is not very convenient for practical calculations due to the complexity of the Σ_n function. Furthermore, it does not provide a clear relationship between the target and the ion-related parameters (e.g., mass and energy) and the sputtering yield. For this reason, Sigmund attempted to derive a simpler expression for the total sputtering yield. He considered the Thomas–Fermi potential for the nuclear stopping cross section and made several simplifications for the ion energies below 1 keV (i.e., energies typical for the sputter deposition). Sigmund derived a simple relation for the total sputtering yield [46]:

$$Y \approx \frac{3}{4\pi^2} \frac{\alpha \Lambda E_i}{E_{sb}} \quad \text{for } E_i \gg E_{sb}. \quad (2.30)$$

This equation depends only on a few target and ion parameters: the energy transfer factor Λ (see Eq. (2.22)), the dimensionless factor α (which is a function of the target-to-ion mass ratio), the surface binding energy E_{sb} , and the incident ion energy E_i .

Sigmund analyzed the factor α for different sputtering conditions and proposed a general function in dependence of the target-to-ion mass ratio (i.e., M_s/M_i). The α function is presented in Figure 13 of [46]. By extracting the data from the figure and fitting a linear function (see Figure 2.10), a good fit to the following function can be found:

$$\alpha \approx k \left(1 + \frac{M_s}{M_i} \right), \quad (2.31)$$

where constant k is approximately 0.15. By inserting Eq. (2.31) into Eq. (2.30) we obtain a simple expression for the total sputtering yield:

$$Y \approx \frac{0.45}{\pi^2} \frac{M_s}{M_s + M_i} \frac{E_i}{E_{sb}}. \quad (2.32)$$

Note that this more elegant equation depends only on two target parameters (the atomic mass and the surface binding energy) and two ion parameters (the atomic mass and

the ion energy). The total sputtering yield, according to this equation, is linearly dependent on the ratio between the target atomic mass and the sum of the target and ion masses. It also depends on the ratio between the ion energy and the surface binding energy. In general, this equation should be useful for calculating sputtering yields of different ion-target combinations for ion energies that are up to 1200 eV. However, the accuracy of the calculated values in many instances differs significantly from the experimental sputtering yield data as is shown in [59]. Nevertheless, Eq. (2.32) provides a very useful insight into the relations between the total sputtering yield, and the ion and the target properties.

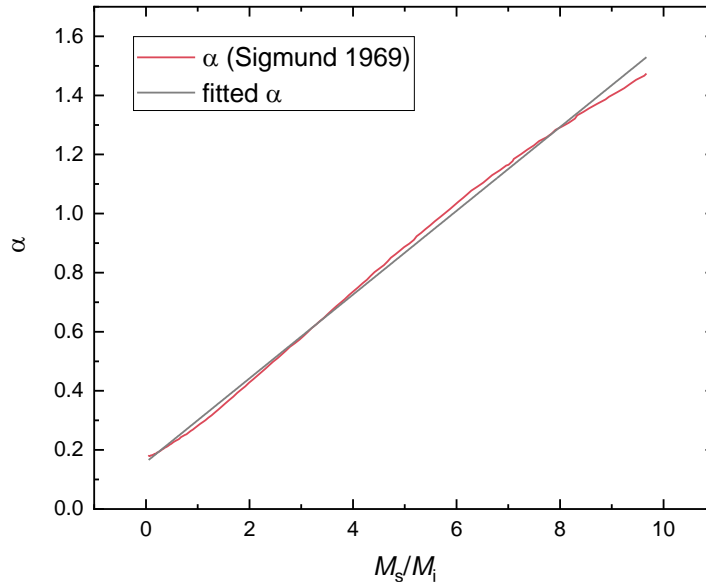


Figure 2.10: The α function in dependence on the target-ion mass ratio. The red line shows original data from Sigmund and the black line the fitted function.

The total sputtering yield is an important parameter in sputtering, but for practical applications (deposition of thin layers, measurements or analysis), the differential sputtering yield Y_d is often more relevant. The differential sputtering yield is defined as:

$$Y_d(\theta, \varphi) = \frac{d^2 Y}{d^2 \omega}, \quad (2.33)$$

where ω is a solid angle of a sphere. If the ion incidence is perpendicular, the sputtering yield does not depend on the azimuthal, but only on the polar emission angle. In Sigmund theory of sputtering, the angular distribution of the sputtered atoms is assumed to be a cosine function of the emission angle [46, 50]. Such a dependence is attributed to the isotropic flux inside the amorphous target material [41].

The integration of the differential sputtering yield over the whole hemisphere gives the value of the total sputtering yield:

$$Y = \int_{\varphi=0}^{2\pi} \int_{\theta=0}^{\pi/2} Y_d(\theta, \varphi) d\omega. \quad (2.34)$$

Chapter 3

Simulations of Sputtering

A more detailed calculation of the interaction between an ion and a solid and the sputtering of the atoms is obtained by following the motion of the particles in the solid (or their trajectories) and the motion of the particles leaving the solid. If the calculations are repeated for a large number of incident ions with different initial conditions (e.g., we randomly change the lateral distance of the collision of the ion with the first atom), then we obtain accurate data on all sputtered atoms. Such an approach became possible with the development of powerful computers and advanced simulation programs. Computer programs allow us to calculate the energy and momentum of each particle for short time steps and store all the data. In this way, we obtain a nearly complete picture of the dynamics of atoms for each ion that enters the solid.

In most cases, simulations are more accurate in providing sputtering yield and energy distribution of sputtered atoms than analytical calculations. In practice, two approaches have been established for simulating the interaction of ions with atoms in solid and the subsequent sputtering of atoms. The first, simpler approach, are the so-called *binary collision simulations*, which use the Monte Carlo method. In these simulations, the motion of particles involved in the collisions and leaving their equilibrium positions is tracked. Other atoms that are at rest in the solid are not considered in the calculations. Another, more detailed and accurate approach, are the so-called *molecular dynamics simulations*, which track the motion of all atoms in the solid, including those that are far from collisions and fluctuate only slightly around their equilibrium positions.

3.1 Molecular Dynamics Simulations

Molecular dynamics simulations consider the interactions among all atoms in a solid [60]. The simulations track the movement of the particles in discrete time steps and treat them classically by assigning motion to each particle according to Newton equation of motion:

$$m_i \frac{\partial^2 x_i(t)}{\partial t^2} = \sum_{j=1}^N \mathbf{F}_{ij} = \mathbf{F}_i(x_i(t)), \quad (3.1)$$

where m_i is the mass of an individual particle, \mathbf{F}_{ij} is the force between the particles, and N is the number of atoms in the solid.

By solving Newton equations for all three coordinates of motion and integrating over multiple time steps, the positions, velocities, and interactions between particles in the system can be tracked. Interactions between atoms are described using empirical and theoretical interatomic potentials. Various potential models exist to describe the interaction between ions and solid, with the most common ones being the Born-Mayer,

Morse, Lennard-Jones, and Coulomb potentials [29]. It is crucial to select an appropriate potential based on the kinetic energy of the simulated particles. Molecular dynamics simulations also consider the interaction with electrons, which contributes to continuous energy losses (see Chapter 2.1).

The boundary conditions must also be well-defined in order to ensure the most representative results despite the limited size of the problem. This means that the atoms designated as boundaries in the simulation should accurately simulate the interaction that would occur if the solid extends in that region. It is also crucial to accurately determine the initial position of the incident ions, ensuring that they do not all collide at exactly the same location. The results will be most similar to experimental measurements if a large number of incident ions is distributed over a representative surface area of the sputtered material (e.g., on one fundamental plane of the crystal material in the case of sputtering crystalline material).

Figure 3.1 shows a simulation of Pt sputtering by Ar ions with 5 keV energy, with the ions incident on the surface at an angle of 83° with respect to the surface normal. It is evident that sputtering of atom clusters occurs in addition to sputtering of individual atoms. This is not the case when sputtering with lower ion energies, where we only observe the sputtering of individual atoms [31].

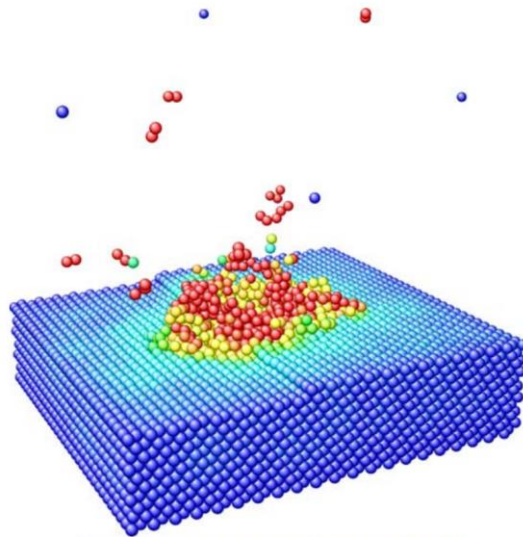


Figure 3.1: Sputtering of Pt (111) with incident Ar ions at an energy of 5 keV. The ions are incident at an angle $\alpha = 83^\circ$ with respect to the surface normal [31].

Molecular dynamics simulations are computationally demanding, often involving a smaller number of simulated particles than necessary for satisfactory accuracy. Disagreement with experimental results, in addition to insufficient statistics, can often be attributed to inappropriately chosen interaction potentials, the size of the simulated environment, or poorly defined boundary conditions. Many times, incomparable results are due to a lack of knowledge about experimental conditions, such as geometric or stoichiometric characterization of the surface. Due to these characteristics, molecular dynamics simulations are somewhat less frequently used than the Monte Carlo simulations of binary collisions, which will be presented in the next chapter.

3.2 Monte-Carlo Binary Collision Simulations

In this section, we provide a more detailed description of simulations based on the Monte Carlo approximation of binary collisions since they are the fastest when simulating a large number of incident ions. These simulations are more commonly used for simulations of sputtering and other interactions of ions with solid rather than molecular dynamics simulations.

All Monte-Carlo BCA (Binary Collision Approximation) programs are based on the TRIM code, which is a basis of the SRIM program. It is still the most commonly used program as it has a simple interface and provides relatively fast and reasonably accurate results. It was developed by Biersack, Ziegler, and colleagues [37, 61, 62]. The program tracks individual binary collisions as ions penetrate through the solid matter. For each collision of the primary ion with atoms in the material and for all subsequent collisions of atoms with other atoms in the material, the program calculates and records the positions, directions, and energies of the particles after the collision, including atoms leaving the material. With such simulations, we can present and visualize the development of collision cascades, radiation damage in the material, directions and energies of scattered and sputtered atoms, backscattered ions, and other characteristics. When simulating a multitude of ion collisions with solid we can evaluate average quantities such as the sputtering yield, and energy and angular distributions of sputtered atoms.

In SRIM simulations, it is assumed that the interaction of ions occurs with an amorphous material. The authors of the program assumed that the material becomes amorphous (i.e., disordered) after collision of a few incident ions. In the first few atomic layers, each crystalline material becomes amorphous as some atoms leave their positions in the crystal structure, and other atoms, after relaxation, occupy different equilibrium positions. In the graphical user interface of the SRIM program, simulations are performed by selecting the type, energy, and direction of ions, as well as the material being bombarded.

The single knock-on regime and the linear cascade regime can be described as a spatially separated sequence of binary collisions. The BCA is based on the assumption that atoms and ions travel in straight trajectories between individual collisions, with their direction (or momentum) changing only during elastic collisions, and they lose energy due to elastic and inelastic interactions.

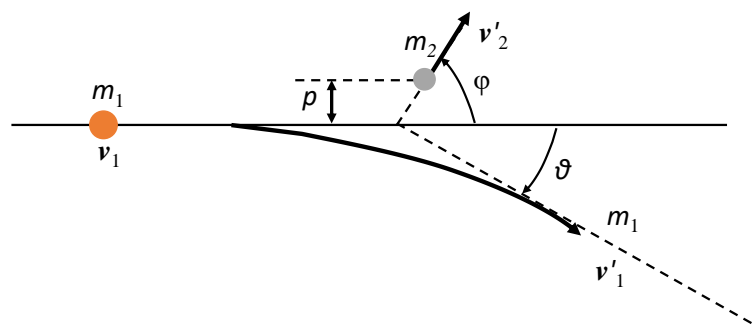


Figure 3.2: Binary collision of an incident particle of mass m_1 and velocity v_1 with a stationary atom of mass m_2 .

The direction of motion of an ion or a recoiled particle in a material can be evaluated after each collision using polar and azimuthal coordinates. The particles travel a characteristic length (mean free path λ), which is determined by the average interatomic distance in the material $\lambda = n^{-1/3}$ (n is the number density of the material). After traveling a distance λ , the ion (or atom advancing in the secondary cascade) collides again and scatters at an angle \mathcal{G} . The recoiled atom moves in the laboratory system at an angle φ after the collision (Figure 3.2). In the collision, the conservation of momentum is:

$$m_1 \mathbf{v}_1 = m_1 \mathbf{v}'_1 + m_2 \mathbf{v}'_2, \quad (3.2)$$

and can be written in components as:

$$m_1 v_1 = m_1 v'_1 \cos \mathcal{G} + m_2 v'_2 \cos \varphi \quad (3.3)$$

$$0 = m_1 v'_1 \sin \mathcal{G} + m_2 v'_2 \sin \varphi, \quad (3.4)$$

where m_1 and m_2 are the masses of the incident and recoiled particles.

The energy required for an atom to leave the solid is determined by the surface binding energy E_{sb} . This quantity is not precisely determined and is often approximated with the heat of sublimation, which depends on the type of atoms, their interatomic bonds, crystal structure and other parameters [18]. The surface binding energies for metals are a few eV (usually between 3 eV and 8 eV).

In calculations of binary collisions, we also need to consider the conservation of the kinetic energy:

$$\frac{1}{2} m_1 v_1^2 = \frac{1}{2} m_1 v'^2_1 + \frac{1}{2} m_2 v'^2_2, \quad (3.5)$$

and transform these equations from the laboratory coordinate system to the center-of-mass system (CMS). We can then express the central mass system energy E_c (i.e., the first Lagrangian function) in polar coordinates as:

$$E_c = \frac{1}{2} M_c (\dot{r}^2 + r^2 \dot{\theta}^2) + V(r), \quad (3.6)$$

where r is the distance between the particles, M_c is the reduced mass in the CMS ($1/M_c = 1/m_1 + 1/m_2$), θ is the scattering angle in the CMS, and $V(r)$ is the potential that causes discrete losses due to elastic collisions between nuclei. In BCA simulations, a screened Coulomb potential is used, which is given by Eq. (2.7).

The conservation of angular momentum in the CMS system is expressed as:

$$J_c = M_c r^2 \dot{\theta} = M_c v_1 p, \quad (3.7)$$

which represents the second Lagrangian function. This equation involves the impact parameter p , which is randomly selected by the Monte Carlo method (see Figure 3.2) as:

$$p = p_{\text{max}} \sqrt{\zeta}, \quad (3.8)$$

where ζ is a random variable equally distributed in the interval $[0,1]$. The maximum impact parameter is calculated from:

$$\pi p_{\max} \lambda = (n)^{-1}. \quad (3.9)$$

The above equation represents the shortest lateral distance at which the particles would approach each other if there were no repulsive forces between them and the path of the moving particle was a straight trajectory. Eq. (3.9) suggests that within a cylindrical volume characterized by a radius p_{\max} and a length denoted λ , a single target atom is contained, representing one collision per atomic volume n^{-1} . SRIM simulations employ the Monte Carlo approach, as some parameters are determined by randomly selecting numbers within predefined probability distributions.

Using equations Eq. (3.6) and Eq. (3.7), we can then calculate the scattering angle [15]:

$$\Theta(p, E_C) = \pi - 2p \int_{r_{\min}}^{\infty} \frac{dr}{r^2 \sqrt{1 - \frac{V(r)}{E_C} - \frac{p^2}{r^2}}}, \quad (3.10)$$

where r_{\min} is the minimum distance at which the particles approach each other during the collision. From the scattering angle, we can calculate the trajectory of the particles. The scattering angle depends on the energy of the moving particle participating in the collision and the randomly chosen impact parameter p .

Considering the conservation laws after each collision, the SRIM program calculates the new energy of the atom as:

$$E_{i+1} = E_i - T - \Delta E, \quad (3.11)$$

where E_i is the energy of the atom before the collision, T is the transferred kinetic energy, and ΔE is the energy loss due to electronic or inelastic interactions. If the transferred kinetic energy T is higher than the binding energy of the atom in the material E_b , the atom can move from its equilibrium position after the collision, and its energy is given by:

$$E_i = T - E_b. \quad (3.12)$$

The program tracks each atom and incident ion until their energy is less than the surface binding energy. These equations are important steps in any BCA program which means also in the SRIM program for tracking the trajectory and energy of the particles involved in collisions.

Figure 3.3 shows an example of a collision cascade caused by an Ar ion traveling through Ti. The simulation was made for the 1000 eV ion impinging normal to the surface. The Ar ion is represented by large spheres and Ti atoms by smaller spheres. The spheres show the positions at which binary collisions occur, either between the ion and the atom, or between the recoiled atom and another atom of the solid. It can be seen that the cascade of this ion results in the emission of two Ti atoms from the surface with energies of 27 eV and 37 eV. Note that the recoiled particles lose significant energy due to interactions between the electrons of the projectile and electrons of the solid. These losses are continuous as the projectile travels through the solid.

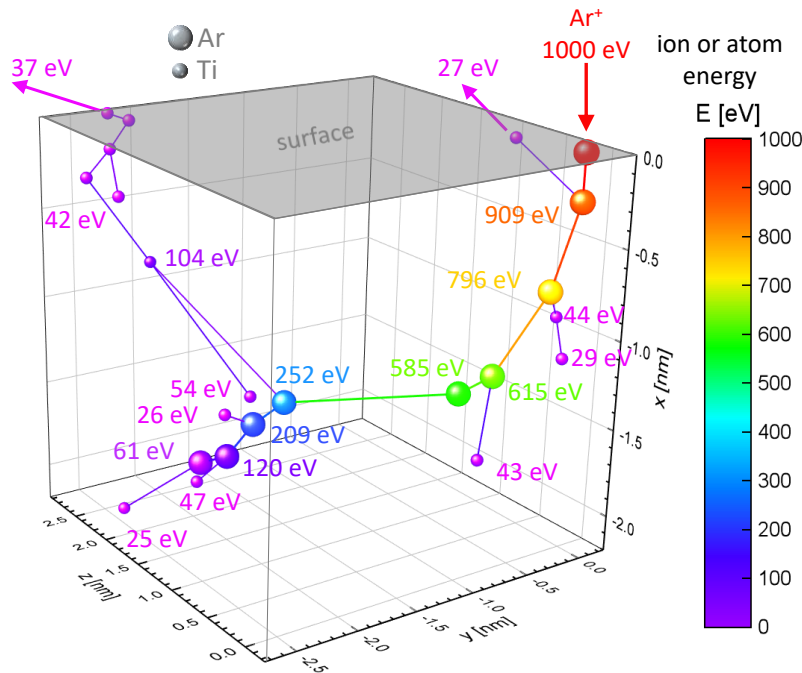


Figure 3.3: An example of a collision cascade caused by an impinging Ar ion (large spheres) in the Ti target (smaller spheres). Data was evaluated from SRIM simulation for Ar ion impinging normal to the surface with an energy of 1000 eV. The color scale shows the energy of the ion and recoiled Ti atoms. Two Ti atoms are emitted from the surface of the solid.

The Monte Carlo approach approximation with binary collision approximation is the most commonly used to simulate sputtering processes. In these simulations, the motion of particles in solid is governed by nuclear and electronic interactions, and the Monte Carlo method ensures that some quantities in the calculations are randomly generated. As mentioned, for each collision between particles, the program randomly selects the lateral distance between the two particles and then calculates the momentum and energy of the moving particles using conservation laws. The program randomly selects the distance to the next collision, which is on the order of the average distance between the grids. Such simulations allow the calculation of collision cascades, the energy and direction of atoms leaving the surface of the solid, and other parameters.

The advantage of these simulations is that a large number of incident ions (even hundreds of thousands) can be simulated with a personal computer in a relatively short time. In this way, we obtain very good statistics on the number of sputtered atoms. The main disadvantage is that binary collision simulations track only the collided atoms and are therefore less accurate than molecular dynamics simulations, which track the motion of all particles.

The existing Monte Carlo programs can be categorized and distinguished based on various factors [1, 6]. Different programs with information on data calculation (p: projectiles only; r: projectiles and recoils; d: dynamics composition changes; t: time dependence) are collected in Table 3.1 along with their references.

The first Monte Carlo code developed for simulating angular and energy distributions is called TRIM.SP (Transport and Range of Ions in Matter) [7]. Subsequently, a dynamic version of TRIM called TRIDYN (DYNAMIC version of TRIM) was developed to track changes in composition, crystallinity, and defects in the target due to scattering [8]. From

these two programs, the SDTrimSP (Static and Dynamic version of TRIM.SP) program was developed [9]. Recently, it has been expanded to enable simulations in two dimensions: SDTrimSP-2D. By adding dimension, the influence of surface roughness on scattering and sputtering can be considered, allowing for the dynamic monitoring of morphological changes.

Table 3.1: Monte Carlo programs [29].

Name	Origin	Authors	Ref.	*p, r, d
ACAT	Atomic Collisions in Amorphous Targets	Takeuchi, Yamamura	[63]	p, r
BABOUM		Abel <i>et al.</i>	[64]	p
BEST	Boltzman Equation Solving Tool	Vicanek, Urbassek	[65]	p, r
CASCADE		Pugacheva	[66]	p, r
COLLIDE		Beeler	[67]	p, r
DYACAT	DYnamical ACAT	Yamamura	[68]	p, r, t
ERPEX		Tatarkiewicz	[69]	p
EVOLVE		Roush <i>et al.</i>	[70]	p, r, d
HERAD	HEterogeneous RAdiation Damage	Attaya, Kulcinski	[71]	p, r
HIDOS		Schonborn <i>et al.</i>	[72]	p, r, d
IMPLNT		Davisson	[73]	p, r
ITMC	Ion Transport in Materials and Compounds	Hassanein, Smith	[74]	p, r
PERST	PERvaya STenka = first wall	Nikiforov <i>et al.</i>	[75]	p, r
PIBER		Adesida, Karapiperis	[76]	p
RITA	Recoil Implantation Through Amorphous	Desalvo, Rosa	[77]	p, r
ROMEO		Melker, Romanov	[78]	p, r
SASAMAL	Simulation of Atomic Scattering in Amorphous Material based on Liquid model	Miyagawa, Miyagawa	[79]	p, r
SAVOY		Jackson	[80]	p
TCIS		Cui, Li	[81]	p, r
TRIDYN	TRIM.SP DYnamical Transport of Ions in Matter	Moller, Eckstein	[82, 83]	p, r, d
TRIM		Biersack, Haggmark	[62]	p
TRIM.SP	TRIM Sputtering	Biersack, Eckstein	[43]	p, r
TRIM85		Ziegler <i>et al.</i>	[84]	p, r
TRIPOS	TRansport of Ions in Polyatomic Solids	Chou, Ghoniem	[85]	p, r, d

*p: projectiles only; r: projectiles and recoils; d: dynamics composition changes; t: time dependence

In this thesis, we focus on simulations based on the Monte–Carlo binary collision approximation, since they are in practice the most commonly used programs for simulating sputtering parameters (i.e., sputtering yield and EDFs). We chose the SRIM program that is one of the most commonly used programs probably due to its open access and relatively simple use.

Chapter 4

Stopping and Range of Ions in Matter (SRIM) Sputtering Simulations

In this chapter, the SRIM program will be presented in detail, including the simulation details and the parameter settings used in this work. We also briefly describe the method of processing the SRIM output data.

The SRIM program was developed in 1985 by J. F. Ziegler, M. D. Ziegler and J. P. Biersack. Some corrections were added later based on the experimental data, however, the program has not been changed since 2013. More than 700 scientific papers per year cite SRIM program since it is used in various research fields [37].

The program monitors the trajectories of all of the particles that are involved in the collisions (the ion and the recoiled atoms) until the energy of the moving particle drops below the threshold that is needed to cause the atom displacement or until the particle leaves the target surface. It records the locations and energies of the particles in the solid as well of the sputtered atoms. In SRIM, it is assumed that the target material is amorphous with atoms at random locations, i.e., the directional properties of the crystal lattice are disregarded. The average quantities, such as the total sputtering yield and average atom energy can be determined by simulating numerous incident ions. The different distributions, such as the energy and angular distributions of the sputtered atoms can also be calculated by post-processing of data.

The SRIM program uses the specific nuclear stopping power function to evaluate the propagation of the ions and the atoms through the solid. The authors of the program (Ziegler, Biersack, and Littmark) proposed the nuclear stopping power, which is derived from the so-called universal atomic potential that is often referred to as the ZBL potential. The ZBL universal screening function $u(r/a)$ was obtained by comparing 106 experimentally determined potentials [37]:

$$u\left(\frac{r}{a}\right) = 0.1818e^{-3.2\frac{r}{a}} + 0.5099e^{-0.9423\frac{r}{a}} + 0.2802e^{-0.4028\frac{r}{a}} + 0.2817e^{-0.2016\frac{r}{a}}. \quad (4.1)$$

The reduced nuclear stopping power in SRIM is calculated from the function:

$$\begin{aligned}
 s_n(\varepsilon) &= \frac{0.5 \ln(1 + A\varepsilon)}{\varepsilon + B\varepsilon^C + Ds}; & \varepsilon \leq 30 \\
 s_n(\varepsilon) &= \frac{\ln(\varepsilon)}{2\varepsilon}; & \varepsilon > 30
 \end{aligned}
 \tag{4.2}$$

where $A = 1.1383$, $B = 0.01321$, $C = 0.21226$, and $D = 0.19593$ are the best fitting factors to the experimental data. The ZBL potential is an improvement of the Krypton–Carbon potential. Note that there are similarities between equations Eq. (2.28) and Eq. (4.2). It should be emphasized that SRIM does not calculate the total sputtering yield from Sigmund’s equation, Equation (2.25). It uses the nuclear stopping power to calculate the interactions between the particles that are involved in the binary collisions. The total sputtering yield is determined from the ratio between the number of sputtered atoms and the number of impinging ions.

For the simulations, we used the version SRIM-2013. The number of impinging Ar ions was set to 10^6 , which generated several thousand to a million sputtered atoms, depending on the target material and the ion energy. Such numbers provided adequate statistics for the evaluation of the differential sputtering yields and energy distribution functions. The “detailed calculation with full damage cascades” type was chosen for the calculation. The default stopping powers that were provided by the program were used. We focused mainly on the evaluation of the sputtering yield for a normal ion impingement, however, several off-axis simulations were also performed.

4.1 SRIM Setup Parameters and Experimental Data

Several parameters which influence the sputtering yield can be adjusted in the SRIM program. These parameters include: the energy and angle of incident ions as well as the surface binding energy, the displacement energy, the lattice binding energy, mass density of the target material and the thickness of the target. Figure 4.1 shows the setup window of the SRIM program.

The surface binding energy presents the potential energy barrier for removing an atom from the surface. It has the greatest influence on the sputtering yield. The displacement energy is defined as the minimum energy that is required to knock a target atom far away from its lattice site so that it does not immediately return to the original position [37]. This results in the formation of a Frenkel pair, i.e., a single vacancy and a nearby interstitial atom. If the atom does not move more than one lattice spacing, it is assumed that it returns to its original position and gives up the energy to the phonons. The typical values of the displacement energy are around 15 eV for semiconductors and 25 eV for metals. The lattice binding energy is defined as the minimum energy that is needed to remove an atom from a lattice site. Hence, this energy is required to break the electronic bonds and displace an atom from a lattice site. The atom which leaves the lattice site loses this energy. The lattice binding energy is always smaller than the displacement energy, with the typical values around 1–3 eV.

TRIM (Setup Window)

Type of TRIM Calculation
 DAMAGE Detailed Calculation with full Damage Cascades

Basic Plots
 Ion Distribution with Recoils projected on Y-Plane

ION DATA

Symbol	Name of Element	Atomic Number	Mass (amu)	Energy (keV)	Angle of Incidence
Ar	Argon	18	39.962	10	0

TARGET DATA

Target Layers

Layer Name	Width	Density (g/cm ³)	Compound	Corr	Gas
Layer 1	10000	4.518	1		

Input Elements to Layer

Symbol	Name	Atomic Number	Weight (amu)	Atom Stoich or %	Damage (eV) Disp	Latt	Surf
Ti	Titanium	22	47.9	1	100.1	25	3 5.2

Special Parameters

Name of Calculation: Ar (10) into Layer 1

Stopping Power Version: SRIM-2008

AutoSave at Ion #: 10000

Total Number of Ions: 1000000

Random Number Seed: []

Plotting Window Depths: Min 0, Max 10000

Output Disk Files

- Ion Ranges
- Backscattered Ions
- Transmitted Ions/Recoils
- Sputtered Atoms
- Collision Details

Special "XYZ File" Increment (eV): []

Buttons: Resume saved TRIM calc., Save Input & Run TRIM, Clear All, Calculate Quick Range Table, Main Menu, Problem Solving, Quit

Figure 4.1: SRIM setup window.

The SRIM provides plots of the collision cascades in different projections in real time during calculations. Ion or recoil distribution, lateral range, ionizations, phonons, damage events, backscattered or transmitted ion distributions can also be plotted. The calculation window also gives information about total sputtering yield, average energy of sputtered particles, and percentage of energy loss due to ionization, vacancies or phonons.

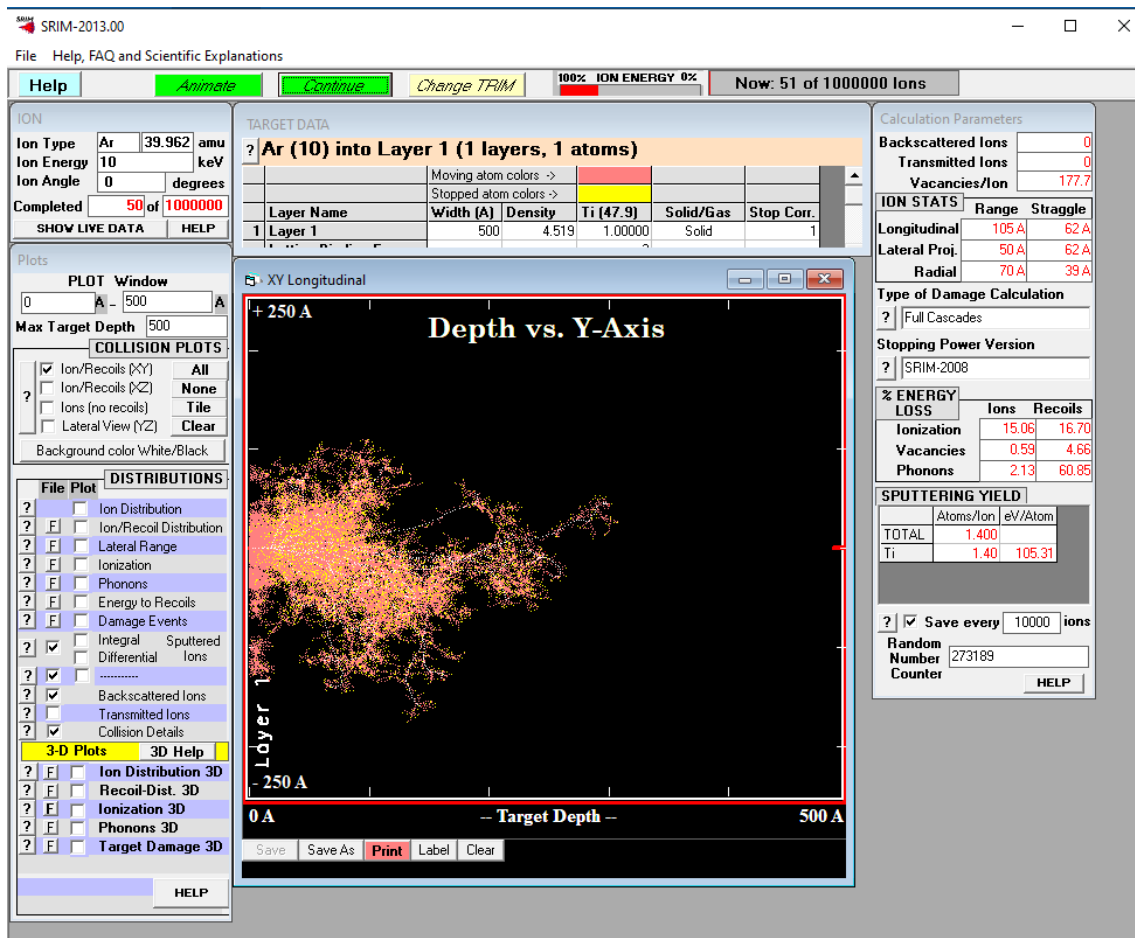


Figure 4.2: Window during calculations of a sputtering cascade.

4.2 Collision Cascades in Solid

The SRIM calculates the trajectories of the ions that enter the solid as described in Section 3.2 and plots each collision point between ions and atoms in real-time during calculation. The trajectories of incident ions and collision cascades for sputtering transition metals with 600 eV Ar ions, plotted by SRIM are shown in Figure 4.3 and Figure 4.4, respectively. For each element, the simulations were run for 10000 incident Ar ions. The side projections of the ion trajectories are plotted in red color and the trajectories of recoiled atoms are plotted in pink. The ranges of ions (red) and atoms (pink) are the largest in group 4 of the periodic table, smaller in group 5 and 11, and the smallest in group 6. The interaction volume becomes slightly wider, but not deeper with increasing period.

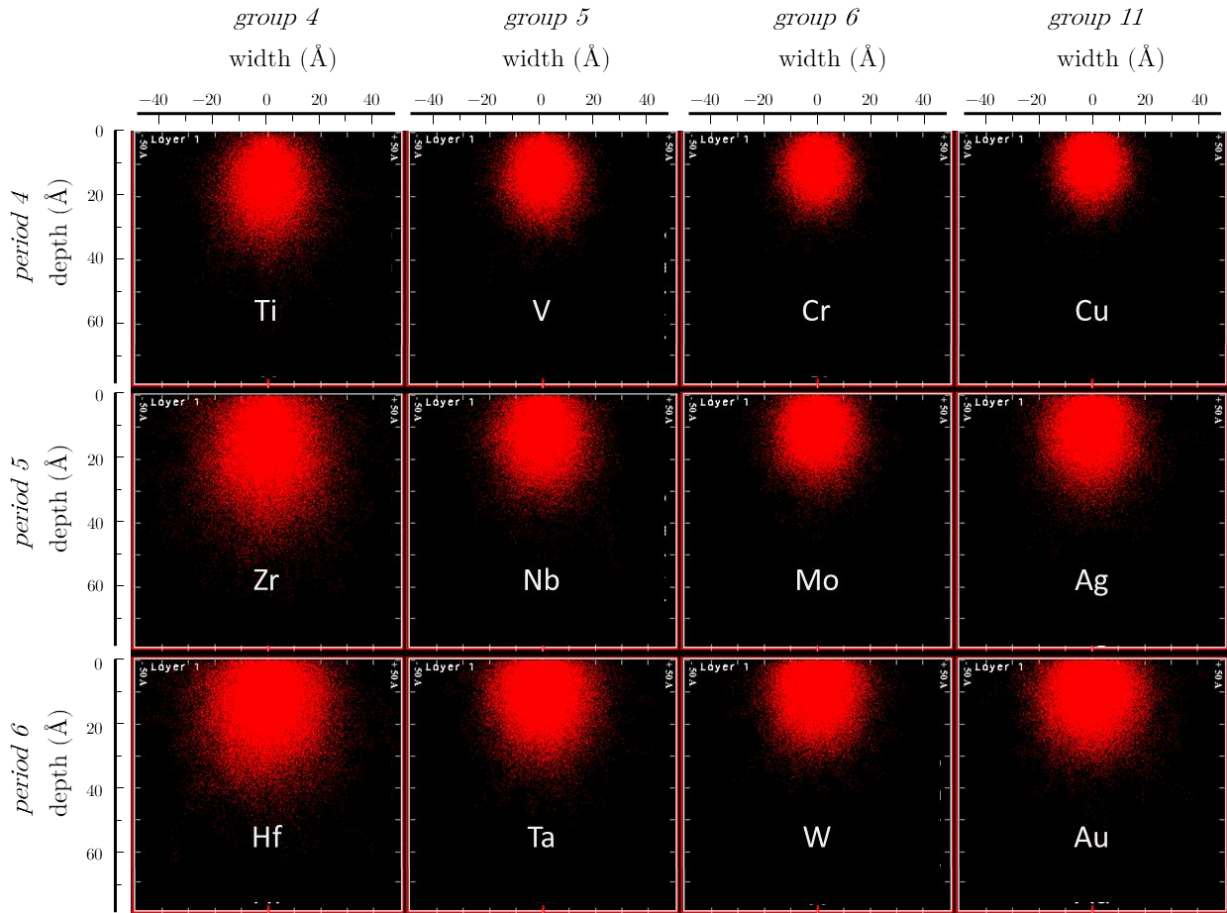


Figure 4.3: The cross-section of the ion interaction volume. 600 eV Ar ions impinging onto Ti, V, Cr, Cu, Zr, Nb, Mo, Ag, Hf, Ta, W and Au solid targets.

The cross-section of the interaction volume of transition metals for incident ions in Figure 4.3 and for the recoiled atoms in Figure 4.4 are informative. To make the comparison between individual elements more quantitative, we determined the depth and width of the interaction volumes for both – ions (red) and atoms (pink) in Figure 4.5.

The depth of the interaction volume decreases with a group in period 4 (Ti, V, Cr, Cu), while in period 5 (Zr, Nb, Mo, Ag) and 6 (Hf, Ta, W, Au), it decreases for groups 4–6 and then slightly increases for group 11 (Figure 4.5a). The depth of the interaction volume increases with a period in group 4 (Ti, Zr, Hf) and 5 (V, Nb, Ta), while groups 6 and 11 do not exhibit such behavior. The interaction volume is slightly deeper for ions than for atoms which can be understood by the fact that incident ions collide with atoms and move the recoiled atoms deeper inside the solid from their equilibrium position.

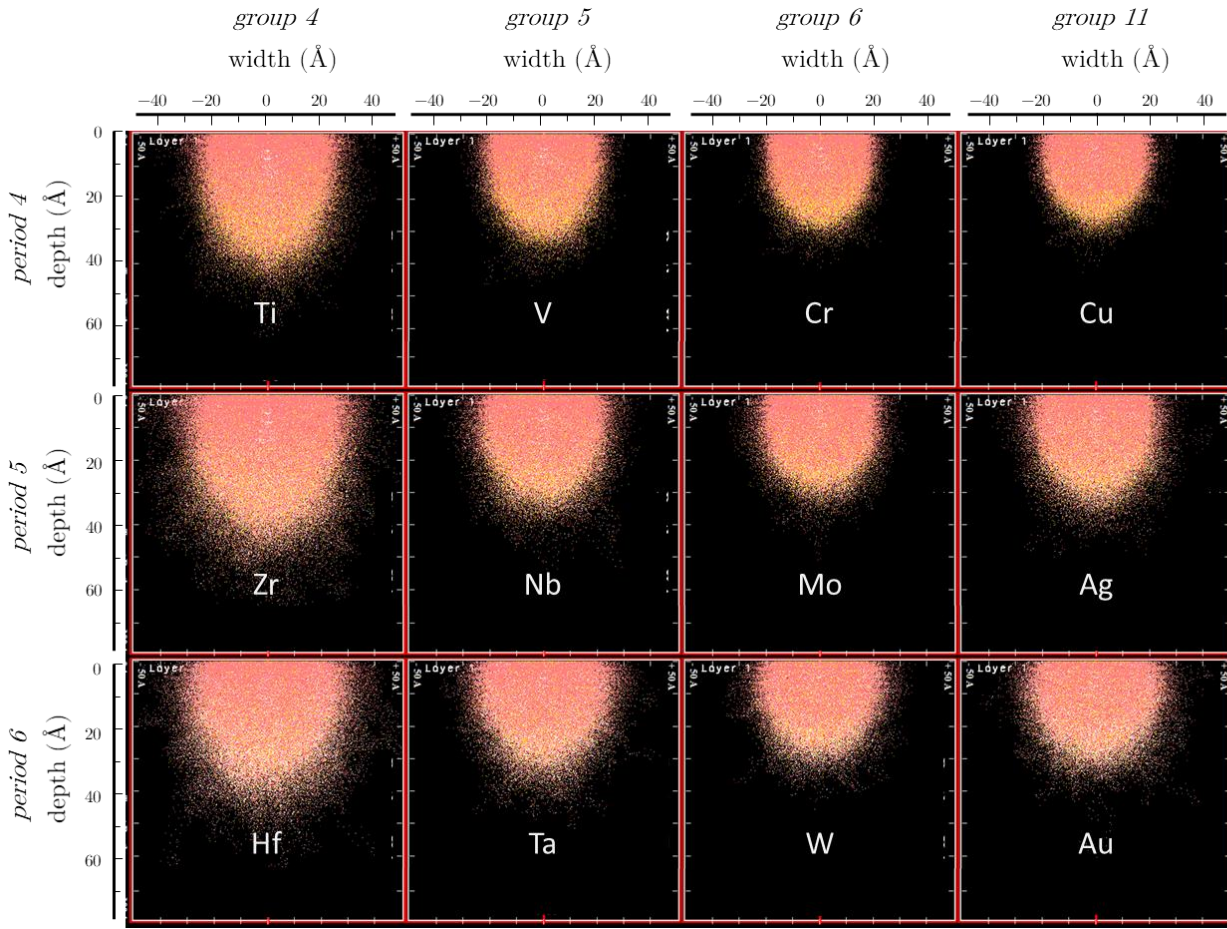


Figure 4.4: The cross-section of the recoiled atom interaction volume for 600 eV Ar ions impinging onto solid targets. The atom trajectories are plotted in pink and yellow shows the final position of an atom.

The interaction volume width of ions (red) and atoms (pink) is the largest in group 4 of the periodic table, smaller in group 5 and 11, and the smallest in group 6 (Figure 4.5b). The interaction volume becomes slightly wider, but not deeper with increasing period.

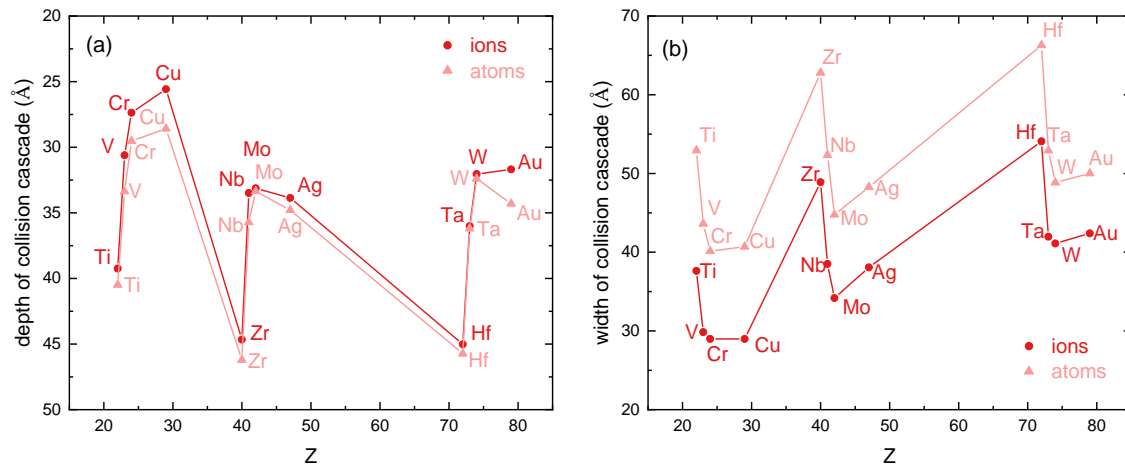


Figure 4.5: (a) Maximum depth and (b) maximum width of impinging ions and atoms. Incident ion energy was 600 eV.

4.3 Total and Differential Sputtering Yield Evaluation

The total sputtering yield (Y) is defined for the entire spatial area into which the atoms are sputtered (i.e., a hemisphere). In SRIM, the total sputtering yield is evaluated by the number of all atoms released from solid divided by number of impinging ions.

The evaluation of the differential sputtering yield requires the processing of the SRIM output data. The output file contains information on the energy, position, and direction of sputtered atoms. The position and direction are provided in the Cartesian coordinate system, and therefore, these data were first converted into a spherical system. The schematic of the geometry that was used for the evaluation of the differential yields is shown in Figure 4.6. In the coordinate system of the SRIM program, the surface normal axis is labeled as x , and it is pointing inwards into the target material. In this work, the sputtered atoms were the focus of the analysis, therefore, we positioned the x -axis in the direction of the surface normal.

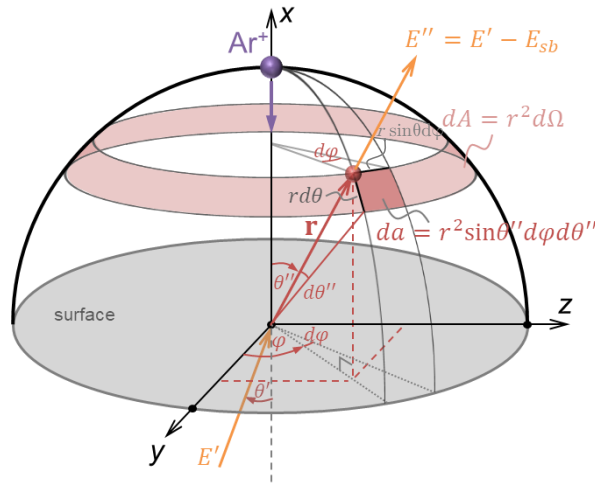


Figure 4.6: Schematic of the geometry in the evaluation of the SRIM data. Ions impact the target surface and cause the emission of sputtered atoms in different spatial directions.

For the atoms that were sputtered into a particular solid angle of a sphere ($d\omega = da/r^2$), the differential sputtering yield Y_d is defined as [2,22]:

$$Y_d(\theta, \varphi) = \frac{d^2 Y}{d^2 \omega} = \frac{1}{N_i} \frac{d^2 N}{d^2 \omega}, \quad (4.3)$$

where N_i is the number of incident ions. The integration of the differential sputtering yield over the full polar (θ) and azimuthal (φ) angles (i.e., the whole hemisphere) gives the total sputtering yield:

$$Y = \int_{\varphi=0}^{2\pi} \int_{\theta=0}^{\pi/2} Y_d(\theta, \varphi) d\omega = \int_0^{2\pi} \int_0^{\pi/2} Y_d(\theta, \varphi) \sin \theta d\theta d\varphi. \quad (4.4)$$

Here, we considered that the differential solid angle in the spherical coordinates is equal to $d\omega = \sin \theta d\theta d\varphi$. The spatial area da which determines the solid angle is marked by the dark red square in Figure 4.6. The spatial area dA and corresponding solid angle $d\Omega = dA/r^2 = 2\pi \sin \theta d\theta$, which is integrated over the azimuth, is also marked in the figure. For a normal ion incidence, sputtering is azimuthally isotropic (i.e., the number of

sputtered atoms does not depend on the azimuthal direction), therefore, we can integrate Eq. (4.4) over the azimuthal angle and write:

$$Y = 2\pi \int_0^{\pi/2} Y_d(\theta) \sin \theta d\theta. \quad (4.5)$$

The derivative of Eq. (4.5) provides the differential sputtering yield in the dependence on the polar angle:

$$Y_d(\theta) = \frac{1}{2\pi \sin \theta} \frac{dY}{d\theta} = \frac{1}{2\pi N_i \sin \theta} \frac{dN}{d\theta}. \quad (4.6)$$

To evaluate the polar distribution, we define a constant differential sputtering yield for the particular polar interval, i.e., $\bar{Y}_d[\theta_1, \theta_2]$. From Eq. (4.6), it then follows that the number of atoms that are sputtered into the polar angle interval can be calculated by the integration from θ_1 to θ_2 :

$$N_d[\theta_1, \theta_2] = 2\pi N_i \bar{Y}_d \int_{\theta_1}^{\theta_2} \sin \theta d\theta = 2\pi N_i \bar{Y}_d (\cos \theta_1 - \cos \theta_2). \quad (4.7)$$

Note that when it is integrated over the whole hemisphere (i.e., $\theta_1 = 0$ and $\theta_2 = \pi/2$), we get $\bar{Y}_d[0, \pi/2] = Y/2\pi$ since $N_d[0, \pi/2] = N$. The polar differential yield is defined as $Y_d(\theta) = d^2Y/d^2\Omega$ and therefore, it is normalized by the factor 2π .

The average differential sputtering yield into a specific polar angle interval $[\theta_1, \theta_2]$ can be rewritten from Eq. (4.7) as:

$$\bar{Y}_d[\theta_1, \theta_2] = \frac{1}{2\pi(\cos \theta_1 - \cos \theta_2)} \frac{N_d[\theta_1, \theta_2]}{N_i}. \quad (4.8)$$

Hence, the differential yield is not simply N_d/N_i , instead it needs to be normalized by the geometrical function $2\pi(\cos \theta_1 - \cos \theta_2)$. This function represents the azimuthal surface area on the hemisphere, which changes with the polar emission angle (see Figure 4.6). When counting the number of atoms for the azimuthally isotropic case, one needs to normalize the number of atoms by this surface area. The units for $\bar{Y}_d[\theta_1, \theta_2]$ are atoms/ion \times sr⁻¹.

For the azimuthally isotropic sputtering, the sum of the polar differential yields into each solid angle $\Delta\Omega_j$ provides the total sputtering yield:

$$Y = \sum_{j=1}^n \bar{Y}_{d,j} \Delta\Omega_j = \sum_{j=1}^n \bar{Y}_{d,j} 2\pi(\cos \theta_j - \cos(\theta_j + \Delta\theta)) = \sum_{j=1}^n \frac{N_{d,j}}{N}. \quad (4.9)$$

Here, we considered that:

$$\Delta\Omega_j = 2\pi \int_{\theta_j}^{\theta_j+\Delta\theta} \sin\theta d\theta = 2\pi(\cos\theta_j - \cos(\theta_j + \Delta\theta)). \quad (4.10)$$

The summation number j ranges from 1 to $n = ((\pi/2)/\Delta\theta) - 1$ with the polar angle interval $\Delta\theta$ (e.g., 10°). To calculate the total sputtering yield from the average differential sputtering yields, which are presented, one needs to multiply the values on the graph by the solid angle factors $2\pi(\cos\theta_j - \cos(\theta_j + \Delta\theta))$.

In the evaluation of the differential sputtering yield, we also considered the assumption that the atoms are refracted as they cross the surface plane due to the surface binding energy, which has already been explained in Section 2.2:

$$\sin\theta'' = \sqrt{\frac{E'}{E' - E_{sb}}} \sin\theta'. \quad (4.11)$$

Here, θ'' is the angle of an atom as it crosses the surface potential barrier and enters the space (vacuum), θ' is the angle of the atom inside the solid, before it crosses the surface, E' is the energy of atom inside the solid, and E_{sb} is the surface binding energy. The surface potential barrier causes the largest atom refraction for the low-energy atoms that are directed under a large angle with respect to the surface normal.

After the transformation that is related to atom refraction, the number of atoms sputtered into a specific polar angle interval was counted. The data were first rearranged by the polar angle, then the number of atoms that were sputtered into a polar interval $[\theta_1, \theta_2]$ was counted for all of the azimuthal angles. The differential sputtering yields were calculated according to Eq. (4.8). The data were evaluated for the 10° polar intervals. The smaller polar intervals of 5° and 3° were also considered, but they provided essentially the same distributions. We also verified that the total sputtering yield that was obtained from the SRIM interface was the same as the one obtained by summing all of the average differential sputtering yields using Eq. (4.9).

4.4 Energy Distribution Functions and Average Energy

The SRIM output data allows for the evaluation of energy distribution functions (EDF) in the whole hemisphere or into specific directions. We evaluated the EDFs by counting the number of sputtered atoms in 1 eV energy bins. Such energy resolution was selected to minimize statistical fluctuations in the number of sputtered atoms.

The EDFs of sputtered atoms in different polar angles were obtained from the energies of atoms sputtered into a particular spatial direction. The energies of atoms were counted together in 10° polar angle intervals, therefore we present sputtered atom energy distribution functions for the mean values of polar angles, such as, 5° , 15° , 25° , etc. in the same way as sputtering yields.

The *total energy distribution function* (total EDF) of all sputtered atoms does not depend on the spatial direction and is defined as

$$F(E) = \frac{dN}{dE}, \quad (4.12)$$

where N is the number of sputtered atoms with energy E .

The *angular energy distribution function* (angular EDF) into a particular solid angle depends on the spatial direction, therefore, it is defined as:

$$f(E, \omega) = \frac{d^3 N(E, \omega)}{dE d^2 \omega}. \quad (4.13)$$

The total energy distribution function $F(E)$ can be obtained from the angular energy distribution functions $f(E)$ by integrating over polar and azimuthal angles:

$$F(E) = \int_0^{\pi/2} \int_0^{2\pi} f(E, \theta, \varphi) d\theta d\varphi = \int_0^{\pi/2} \int_0^{2\pi} \frac{d^3 N(E, \theta, \varphi)}{dE d\theta d\varphi} d\theta d\varphi. \quad (4.14)$$

For a discrete differential energy distribution function, the following expression can be used $F(E) = \sum_{j=1}^n f_j(E, \theta_j)$, where n is the number of polar intervals.

For isotropic sputtering around the surface normal the solid angle ω can be replaced by Ω (see Figure 4.6). The number of atoms in a particular energy interval for the specific spatial direction provides the angular energy distribution function:

$$f(E, \Omega) = \frac{d^3 N(E, \Omega)}{dE d^2 \Omega}. \quad (4.15)$$

The equation only depends on the emission angle Ω . From Eq. (4.15) we can then calculate the total energy distribution function as:

$$F(E) = \int_0^{\pi/2} f(E, \theta) d\theta. \quad (4.16)$$

When comparing the intensity of the simulated EDFs within two different polar intervals, we should consider the spherical geometry in a similar way as for sputtering yield evaluation. Each energy distribution function into a specific polar interval (θ_1, θ_2) should therefore be normalized by a factor $2\pi(\cos \theta_1 - \cos \theta_2)$.

As discussed previously, the atom that passes through the surface is refracted toward the surface due to the surface potential barrier (i.e., surface binding energy, see Eq. (2.18) (2.19) and (4.11)).

4.5 Average Energy of Sputtered Atoms

The average energy of atoms sputtered into a hemisphere can be calculated as:

$$\bar{E} = \frac{\int_0^{\infty} E \cdot F(E) dE}{\int_0^{\infty} F(E) dE} = \frac{1}{N} \int_0^{\infty} E \cdot F(E) dE. \quad (4.17)$$

The average energy of sputtered atoms in a particular polar angle interval $\Delta\theta$ is defined by the following equation:

$$\bar{E}_{\Delta\theta} = \frac{\int_0^{\infty} E \cdot f(E, \Delta\theta) dE}{\int_0^{\infty} f(E, \Delta\theta) dE}, \quad (4.18)$$

where E is the energy of sputtered atoms and $f(E, \Delta\theta)$ is the angular EDF of sputtered atoms in the interval $\Delta\theta$.

In practice, when dealing with SRIM output data, the average energy into a particular polar interval $\Delta\theta$ is calculated from the discrete numerical values as:

$$\bar{E}_{\Delta\theta} = \frac{\sum_{j=1}^{N_{\Delta\theta}} E_{\Delta\theta,j}}{N_{\Delta\theta}}, \quad (4.19)$$

where $E_{\Delta\theta,j}$ is the energy of each atom sputtered into a particular polar interval $\Delta\theta$ and $N_{\Delta\theta}$ is the total number of sputtered atoms in the same interval.

The average energy of all sputtered atoms into the hemisphere is:

$$\bar{E} = \frac{\sum_{i=1}^N E_i}{N}. \quad (4.20)$$

Here, N is the number of atoms sputtered into the whole hemisphere.

Chapter 5

Experimental Methods

The samples upon which we conducted our measurements in order to determine the sputtering yield were prepared in a triode system and a magnetron sputtering system, both of which are described in detail in this chapter. We commence with an explanation of diode sputtering. From the literature we obtained a large amount of data from the ion beam sputtering, which were compared to simulation results, therefore the characteristics of these techniques are also highlighted. Subsequently, we also provide details about two methods used to measure the total and differential sputtering yield.

5.1 Sputter Deposition Techniques

The spatial distribution of atoms arriving on the substrate is important since it affects the uniformity of the growing thin film in terms of film thickness and its structural, physical, and chemical properties. Sputtering is in general a line-of-sight process in which the sputtered atoms travel in straight lines from the source to the substrate unless collisions with the residual gas atoms strongly influence trajectories of sputtered atoms. The spatial and energy distribution of sputtered atoms therefore depend on sputtering source of different techniques which will be presented in this subsection.

5.1.1 Diode sputtering

The simplest way of creating plasma and initiating sputtering is in the so-called diode configuration. In the *diode sputtering system*, two parallel-plate electrodes are positioned facing each other, as illustrated in Figure 5.1. One electrode is on the negative potential (cathode) and the other electrode (anode) is positive with respect to the cathode. Plasma is created by applying a high potential between the electrodes, typically a few kilovolts, at a pressure in the 100–1000 Pa range.

The breakdown process and the formation of plasma occur in the following steps. The gas breakdown occurs if there are some free electrons present in the gas. A few electrons are always present in the gas, created by natural processes such as radioactive decay or cosmic rays. The first electron that is formed near the cathode is accelerated away from the cathode toward the anode by the electric field between the electrodes. During acceleration, the electron collides with the gas and creates new pairs of ions and electrons. Hence, a cascade of new electrons is accelerated toward the anode. This ionization process is referred to as the *Townsend regime*.

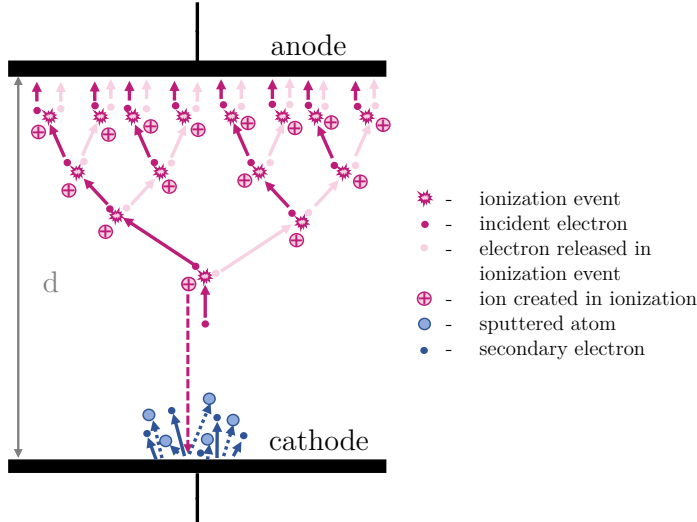


Figure 5.1: Schematics of the diode sputtering illustrating the Townsend avalanche and the sputtering process.

In the Townsend avalanche process, the atoms are ionized and the ions are accelerated toward the cathode. They collide at the energies defined by the applied voltage between the electrodes and cause sputtering of the target material. In addition to the sputtered atoms, *secondary electrons* are released from the cathode. These electrons are important for sustaining the discharge since they are accelerated away from the cathode and gain energy from the potential difference near the cathode. As long as the voltage is applied between the electrodes, the ionization process, and thus the plasma, is self-sustained. Not every ion causes a release of secondary electrons. The probability of emitting a secondary electron is defined by the secondary electron yield:

$$Y_{SE} = N_e / N_i , \quad (5.1)$$

where N_e is the number of electrons emitted by the impact of N_i ions. The emission of secondary electrons is practically independent of the ion energy. Namely, in the relatively low ion energy range, up to 2 keV, the so-called potential emission mechanism determines the secondary electron yield. In this mechanism, the electrons are liberated by an Auger electron transition, which is related to the potential energy of the arriving ion projectile and not to its kinetic energy. In a moment before high energetic ion collides with the solid, it is neutralized. This means that an ion collects an electron from the metal target. In this process, the energy is released and can cause an excitation of another electron in the target. The maximum energy that is released in the first step of this process is $E_{pot} - \phi$, where E_{pot} is the potential energy of the incoming primary ion (in most cases the ionization potential) and ϕ is the metal work function (for most metals it is in 3–5 eV range). The minimum energy needed to release an electron is equal to a work function, therefore the maximum energy of the secondary electron is $E_i - 2\phi$. In the literature, the experimental data for the secondary emission yields has been related to the work function and Fermi energy E_f . For various ions the following relations have been found [24, 86]:

$$\begin{aligned}
 Y_{SE} &= 0.032(0.78E_{pot} - 2\phi) \\
 Y_{SE} &= 0.016(E_{pot} - 2\phi) \\
 Y_{SE} &= \frac{0.2(0.8E_{pot} - 2\phi)}{E_f}
 \end{aligned}
 \tag{5.2}$$

According to the first of the above equations, secondary emission only occurs if $0.78E_{pot} > 2\phi$. For Ar ions that have $E_{pot} \approx 15.76$ eV such condition is fulfilled (see Figure 5.2). Typically, the secondary electron yield is in the range of 0.1 to 0.2. It should be noted that at higher ion energies (e.g. above 1 keV), the kinetic emission mechanism starts to play a role in the emission of secondary electrons.

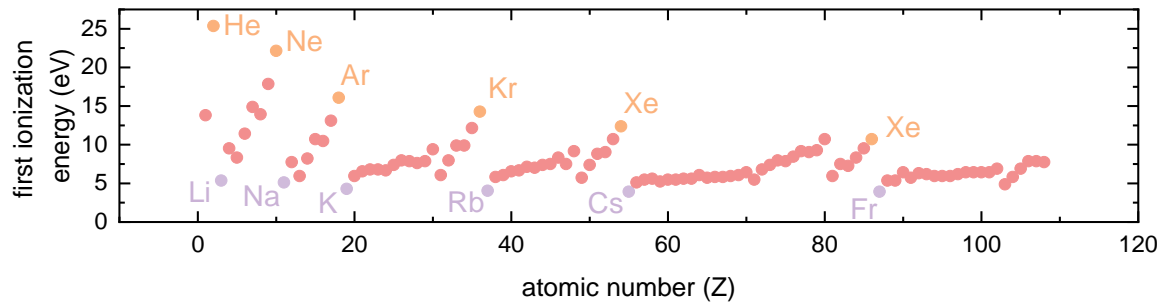


Figure 5.2: First ionization potential for atoms in the periodic system (data obtained from [87]).

5.1.2 Triode sputtering

The diode sputtering configuration has many practical drawbacks. First of all, it requires high pressures and voltages in order to sustain the discharge. This means that many collisions occur between the sputtered atoms and the surrounding gas, which significantly reduces their energy. In addition, high voltages require the use of high-voltage power supplies. However, the most important drawback of diode sputtering is a low deposition rate. Another important disadvantage of diode sputtering is the cathode-anode arrangement, which cannot be simply scaled up to industrial-sized applications. For these reasons, the diode sputtering is practically never used for the deposition of thin films.

Many of the diode sputtering drawbacks can be overcome by providing an additional plasma source. Such a configuration is called the *triode sputtering*, shown schematically in Figure 5.3. The additional plasma source is usually generated by a heated filament (red wire in Figure 5.3). Electrons emitted from the filament are accelerated in the electric field toward the anode. On their path they cause ionization and thus help to sustain the discharge. Usually, the electron beam from the filament is densified and confined by an external magnetic field (coil).

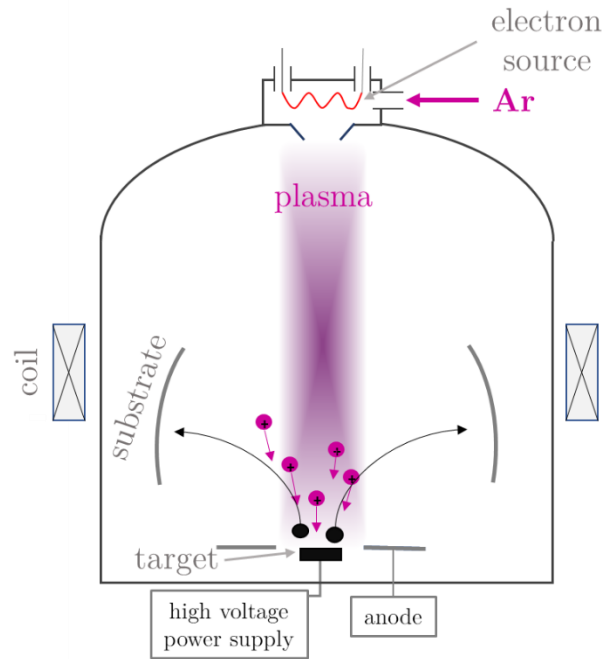


Figure 5.3: Schematics of the triode sputtering system.

An important consequence of the additional electron source is that the discharge is sustained independently of the voltage applied to the sputtering cathode (i.e. target). Due to the additional electron source, the discharge can operate at much lower gas pressures – typically in the 1 Pa range, which is several orders of magnitude lower than in the diode discharge (typically 100–1000 Pa). Lower gas pressure means that atoms experience only a few collisions with the atoms on their path toward the substrates and the atoms can arrive at the substrates with higher energies. Atoms with high energies form denser films and greatly improve the overall quality of the deposited thin films. In general, the principles of operations in the triode system are the same as in the diode system. Due to higher density of plasma, the deposition rate is higher than in the diode sputtering system. Despite advantages of the triode sputtering configuration, it is nowadays rarely used in practice because of the design of a cathode with a magnetic field, which does not require additional plasma source.

5.1.3 Magnetron sputtering

The design where a magnetic field is present near the cathode is called the magnetron sputtering and the device is called the magnetron (or the magnetron source). The discharge created by the magnetron is thus called the magnetron discharge.

In the magnetron specifically arranged permanent magnets are placed behind the cathode. Two sets of magnets with opposite magnetic polarity are used. For example, in the center of a circular magnetron there is a magnet of one magnetic polarity (e.g. magnetic south) while on the perimeter of the cathode there is a magnet of opposite magnetic polarity (magnetic north) facing the target (see Figure 5.4). In such magnet configuration, the magnetic field lines are curved above the cathode and strong magnetic fields are present near the cathode (up to 0.2 T).

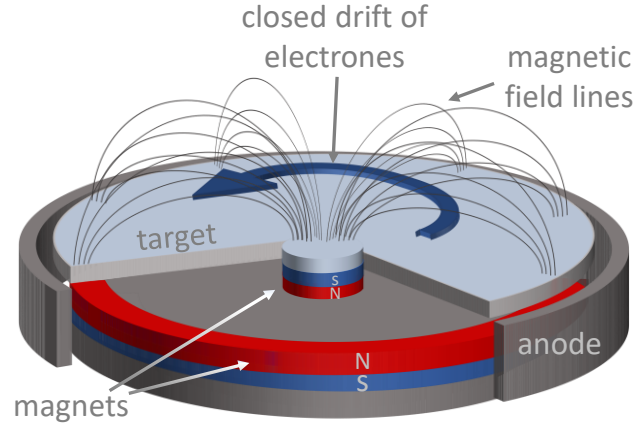


Figure 5.4: Schematic cross-section of a planar magnetron.

The reason for a very dense plasma in front of the magnetron and thus very high sputtering rate is related to the motion of electrons in the crossed electric and magnetic field. In order to understand the motion of electrons in the magnetron we first examine the motion of charged particles individually for the electric field and separately magnetic field, and then analyze their motion in the combination of the two fields.

The electric force (\mathbf{F}_e) on a particle with an electric charge (q) in the electric field (\mathbf{E}) is described by the relation:

$$\mathbf{F}_e = q\mathbf{E}. \quad (5.3)$$

Charged particles follow the direction of the electric field. By convention, the electric field is defined in such a way that positive ions move in the direction of electric field lines, while the electrons move in the opposite direction.

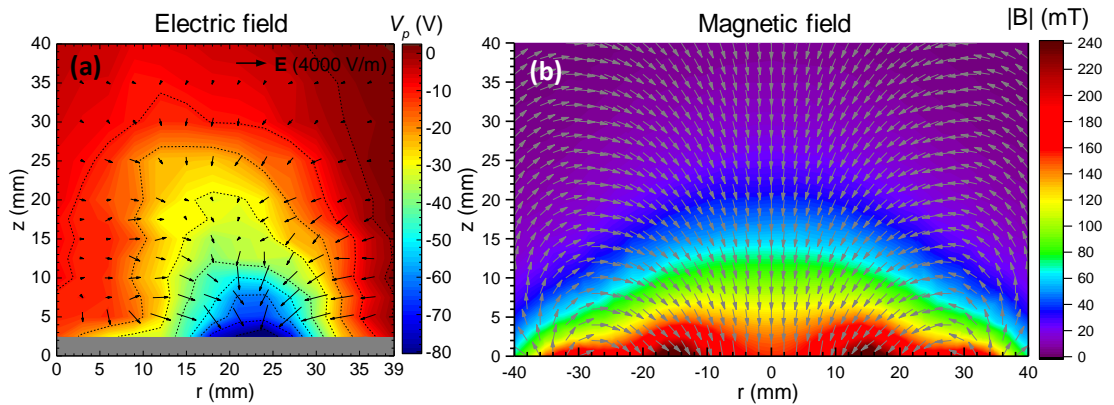


Figure 5.5: (a) Plasma potential and electric field distribution measured in magnetron plasma. (b) Magnetic field distribution in typical magnetron [88].

The motion of charged particles in the magnetic field is defined by the cross product between the velocity vector of the charged particle (\mathbf{v}) and the magnetic field vector (\mathbf{B}), that is:

$$\mathbf{F}_m = q\mathbf{v} \times \mathbf{B}. \quad (5.4)$$

The above equation states that charged particles follow orbital motion, i.e. they rotate around the magnetic field lines. If we combine Eq. (5.4) with the equation for the centripetal force ($F_c = mv^2/r$), then we can calculate the radius (r) of orbital motion:

$$r = \frac{mv_{\perp}}{qB}. \quad (5.5)$$

Here, v_{\perp} is the velocity perpendicular to the magnetic field line and B is the strength of the magnetic field. The above radius is called the Larmor radius. The direction of the particle rotation depends on the charge of the particle as defined by Eq. (5.4). Electrons rotate in one direction, while in the same magnetic field, the ions rotate in the opposite direction. The magnitude of the Larmor radius is very different for electrons and ions since it depends on the mass of the charged particle. For example, in a magnetron with a typical magnetic field strength of 100 mT, the Larmor radius for electrons with 100 eV is 0.34 mm, while for Ar ions with the same energy it is 91 mm. The Larmor radius for ions is much larger than for electrons. This has important consequences for the motion of electrons and ions in the magnetron. Electrons feel a strong influence of the magnetic field while ions are only slightly affected by it. Since a typical diameter of magnetrons is several centimeters, and because the strength of the magnetic field decreases very fast with the distance from the magnetron, the motion of ions is influenced only by the electric field. On the other hand, the motion of electrons is strongly affected by the electric and magnetic fields.

If we combine equations Eq. (5.3) and Eq. (5.4) we get the so-called Lorentz force. The equation of motion for an electron in the electric and magnetic field is therefore

$$m_e \frac{d\mathbf{v}_e}{dt} = -e(\mathbf{E} + \mathbf{v}_e \times \mathbf{B}). \quad (5.6)$$

The solution of the above differential equation is not trivial, especially in the case of highly non-homogenous electric and magnetic fields present in the magnetron. The magnitude and direction of electric and magnetic field strongly vary in the space as is demonstrated in Figure 5.5. Upon introducing an electric field between the anode and cathode, the cyclotron revolutions result in a net drift perpendicular to both the magnetic and electric field vectors, known as the $\mathbf{E} \times \mathbf{B}$ drift. This drift exhibits closed-loop behavior in the azimuthal direction within the planar magnetron geometry, effectively trapping the electrons to the magnetic field line.

The electric field between the cathode and anode is non-uniform. Following the discharge plasma formation, the voltage drop primarily occurs in the space-charge layer adjacent to the target surface, called the sheath. Only a small fraction of the voltage drop occurs outside the sheath, contingent on the magnetic field and discharge conditions. This distribution has implications for electron energy, with most energy gained by electrons crossing the sheath from the target surface, leading to highly energetic secondary electrons. On the other hand, plasma electrons, possessing lower energy (a few eV), cannot penetrate the sheath and are reflected back to the plasma.

The combination of crossed electric and magnetic field entraps electrons close to the cathode and does not allow them to easily escape the trap. Electrons follow a closed path near the cathode, which strongly increases the probability for the collision with the gas atoms. More frequent collisions therefore result in a much higher plasma density than in the case of the cathode without a magnetic field, such as in diode discharges. The specific path of electrons increases the plasma density only over a part of the cathode. Ions from

this dense plasma region are accelerated by the electric field toward the cathode, therefore, the target erosion is the highest over the area that is the nearest to the region of high plasma density. The area of erosion is usually referred to as a "racetrack" since electrons follow a similar path.

The entrapment of electrons in magnetron sources has several consequences: (1) the discharge can work at much lower pressures (typically 1 Pa or lower) and voltages (several 100 V) than in the diode sputtering, (2) the deposition rate is much higher due to enhanced ionization, (3) the geometry of magnetron can be simplified by placing an anode around the cathode, and (4) it can be easily scaled up to industrial requirements.

5.1.4 Ion beam deposition

The main advantage of ion beam deposition technique is that the ion source and the deposition chamber are physically separated. The ion beam source design and capabilities directly influence the deposition process precision, control, and uniformity. The energy, current density, and ion species in the beam can be adjusted by controlling various parameters in the ion beam source, such as gas pressure, radiofrequency (RF) power, magnetic field strength, and extraction voltage. The ions from ion beam sources impinge on the target at a precisely defined incidence angle (Figure 5.6). Some setups also allow changing the position of the ion gun or the inclination of the target, which allows changing the incidence angle of the ions.

There are different types of ion beam sources used in ion beam deposition, and each has its advantages and is used in specific applications. One source type are ion guns. These are devices that generate a beam of ions by ionizing gas atoms or molecules. They normally utilize ionization by energetic electrons to ionize the gas, creating a stream of ions with a precise energy range. The ion beam can be focused and accelerated towards the target and substrate using electromagnetic lenses and electrodes.

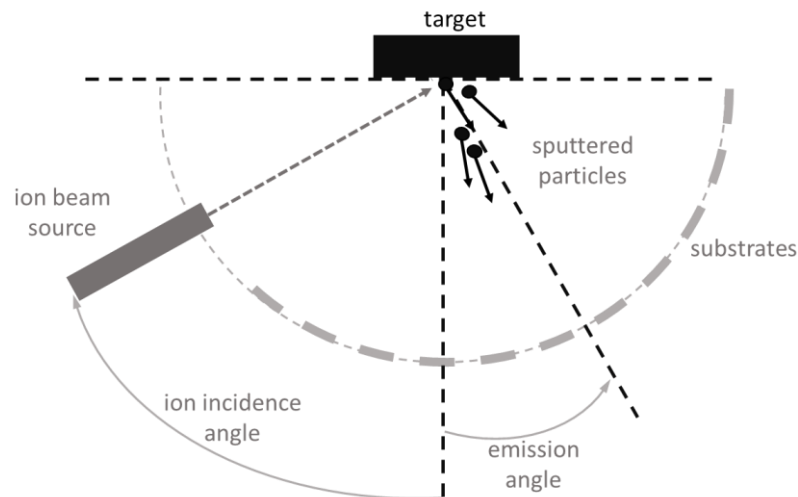


Figure 5.6: Scheme of ion beam deposition.

Another type are Kaufman-type and Freeman-type ion sources. Both types are RF ion sources that use a combination of magnetic and electric fields to generate and accelerate ions. The RF power is applied to a coil or antenna, producing a plasma within the ion source. The magnetic field confines the plasma and enhances ionization, while the electric field accelerates the ions towards the substrate. Each type uses a different geometry for the magnetic and electric fields.

Electron cyclotron resonance ion sources use microwave radiation to create a high-density plasma and ionize gas atoms or molecules. The ions are then extracted and accelerated into a beam.

Ion beam deposition is commonly used in the research field but not in industrial setting since the deposition rates are low and the configuration cannot be easily scaled up.

5.2 Measurement of the Sputtering Yield

The measurement of the sputtering yield can be carried out using different experimental techniques, both by direct and indirect measurements. In this chapter, two methods for determination of the sputtering yield used in this thesis are presented: the target mass change measurements for assessing the total sputtering yield and the layer thickness change measurements for assessing the differential sputtering yield.

5.2.1 Measurements of total sputtering yield from target mass change

A straightforward method for determining the sputtering yield is to measure the change of the target mass before and after the sputtering. Namely, the number of all sputtered atoms is in good approximation proportional to the mass change of the target material. In this method, the implanted ions and other impurities are neglected. As we have already mentioned, the sputtering yield is defined as the number of sputtered atoms per incident ion:

$$Y = \frac{N_s}{N_i}. \quad (5.7)$$

The amount of substance n in a given sample of solid is defined as a ratio between the number of elementary entities N and the Avogadro constant N_A :

$$n_s = \frac{N_s}{N_A} = \frac{m_s}{M_s}. \quad (5.8)$$

In the above equation we used the index s referring to sputtered atoms. Mass of sputtered atoms m_s in practice equals the measured loss of target mass Δm .

By combining Eqs. (5.7) and (5.8) we can calculate the sputtering yield as:

$$Y = \frac{\Delta m}{M_s N_i} N_A, \quad (5.9)$$

where Δm is the measured loss of target mass, M_s is the atomic mass of the target material, N_i is the number of incident ions and N_A is the Avogadro number.

The number of incident ions can be estimated from the ion current I on the cathode:

$$I = Q/t = q(N_i + \gamma N_i)/t, \quad (5.10)$$

where we also take into account the secondary electron yield γ . In Eq. (5.10), q is the elementary charge and t is the time of sputtering.

Assuming single-charged ions and dividing the total charge by the elementary charge q , the total number of impinging ions during the experiment is:

$$N_i = It / q(1 + \gamma). \quad (5.11)$$

By combining Eqs. (5.9)–(5.11) we get the equation for the total sputtering yield:

$$Y = \frac{\Delta m \cdot q(1 + \gamma)}{M_s It} N_A. \quad (5.12)$$

In the thesis, different target materials were sputtered in the triode sputtering system Sputron (Balzers, Liechtenstein) (Figure 5.7). Measurements of the mass change in the target before and after the sputtering were performed using the Radwag ps 750/c/2 balance with 1 mg readability value.



Figure 5.7: Sputtering Ti target with Ar ions in the Sputron deposition unit.

5.2.2 Measurements of differential sputtering yield from film thickness

An important parameter in thin film deposition is the thickness of the film for a given time interval. It is called the deposition rate, it is easy to measure and usually given in nm/min. We measured the thickness of the deposited thin layer with a Bruker Dektak XT profilometer.

The thickness of the deposited thin film also gives information about the sputtering yield. Assuming that sputtered atoms do not collide between the target and the sample and that the sputtered atoms travel in straight trajectories, one can obtain angular distribution of sputtered atoms.

In a polar position θ for a given time t , the number of sputtered target atoms deposited onto the substrate increases to a value that is proportional to the differential sputtering yield [89-91]:

$$Y_d(\theta) = \frac{R(\theta)N_Aqr^2}{M_sIA_s}. \quad (5.13)$$

Here, r is the distance between the target surface and the sample with the surface area A_s . The mass accumulation rate $R(\theta)$ in Eq. (5.13), is defined as:

$$R(\theta) = \frac{\Delta m_s}{t}, \quad (5.14)$$

and is usually given in [g/s]. Since we measured the thickness h of the deposited film instead of the mass change of the sample, we assumed that the material density of the deposited layer ρ equals the density of the pure material at room temperature and calculated the accumulation rate as:

$$R(\theta) = \frac{\rho h A_s}{t}. \quad (5.15)$$

By combining this Eq. (5.15) with Eq. (5.13) we determined the differential sputtering yields as:

$$Y_d(\theta) = \frac{\rho h N_A q r^2}{t M_s I}. \quad (5.16)$$

To calculate a differential yield, several parameters must be considered. These parameters include the molecular weight of the target atoms (M_s in g/mol), the distance from the target center to the samples r which was in our experiment 10 cm. Additionally, the sample area into which the thin film was deposited beside the electronic charge q and Avogadro's number N_A was used in our calculations. The differential yield value can be calculated when ion current and time of sputtering are known.

In practice, we measured the thickness of thin films deposited onto the substrate with a semicircular substrate with radius $r = 10$ cm, so that all measurement points were equally distanced from the region of sputtering (Figure 5.8). The samples were positioned in 10°

steps. The semicircular substrate holder was positioned at the center of origin on the target surface. The lateral position was aligned to the center of the racetrack region.



Figure 5.8: Experimental set-up. The samples are positioned in 10° steps on the semicircular holder.

In the second part of the experiments, we improved the set-up. In order to reduce the target area from which the sputtered atoms originate – to experimentally establish a point-like source of atoms – we made collimators with a length $l = 1$ cm and diameter $d = 0.6$ cm and attached them to the semicircular substrate in 10° steps as seen in Figure 5.9.



Figure 5.9: Experimental set-up with collimators for measuring the angular dependent sputtering yield.

Chapter 6

Results and Discussion

SRIM simulations were performed for a range of single-element materials from the periodic table. The goal was to methodologically explore the differences in the sputtering yields and energy distribution functions. We performed a series of simulations for target materials typically used in the sputter deposition techniques. In particular, we analyzed sputtering of elements lighter than the bombarding Ar ion ($Z = 18$) – including B, C, Al and Si (i.e., $Z = 5, 6, 13, 14$, respectively), and the transition metal elements from groups 4, 5, 6 and 11 (i.e., Ti, Zr, Hf; V, Nb, Ta; Cr, Mo, W; Cu, Ag, Au). Such material selection allowed us to explore differences for elements of the same group or period of the periodic table (see Figure 6.1). For each material, we performed more detailed simulations for Ar ion energies of 300 eV, 600 eV and 1200 eV to evaluate the differential sputtering yields as well as differential energy distribution functions. Such energies were chosen to be roughly comparable to the typical ion energies encountered in the DC magnetron sputtering (DCMS), high-power impulse magnetron sputtering (HiPIMS) and triode sputtering.

		<i>group</i>																	
		1											13	14	15	16	17	18	
<i>period</i>	1	H																	He
	2	Li	Be											B	C	N	O	F	Ne
	3	Na	Mg	3	4	5	6	7	8	9	10	11	12	Al	Si	P	S	Cl	Ar
	4	K	Ca	Sc	Ti	V	Cr	Mn	Fe	Co	Ni	Cu	Zn	Ga	Ge	As	Se	Br	Kr
	5	Rb	Sr	Y	Zr	Nb	Mo	Tc	Ru	Rh	Pd	Ag	Cd	In	Sn	Sb	Te	J	Xe
	6	Cs	Ba		Hf	Ta	W	Re	Os	Ir	Pt	Au	Hg	Tl	Pb	Bi	Po	At	Rn

Figure 6.1: Target materials investigated by SRIM simulations sputtered by Ar ions.

The simulations were performed with the latest version SRIM-2013. The number of impinging Ar ions was set to one million, which generated several hundred thousand to a million sputtered atoms, depending on the target material and ion energy. Such numbers provided adequate statistics for the evaluation of the differential sputtering yields. A "detailed calculation with full damage cascades" type was chosen for the calculation. The default stopping powers provided by the program were used. We focused mainly on the evaluation of sputtering yield for normal ion impingement, however, several off-axis simulations were also performed.

6.1 Total Sputtering Yield

Here, we examine the sputtering yields that were simulated by the SRIM program. SRIM free input parameters were optimized in order to achieve better agreement between simulations and experimental values of sputtering yield collected by Behrisch and Eckstein [31]. Further, we attempt to derive some general trends and relations between the sputtering yield, and the target- and ion-related properties as well as the order of the elements in the periodic table.

6.1.1 Surface binding energy

In Figure 6.2, we present the influence of free SRIM input parameters on the total sputtering yield: the surface binding energy (E_{sb}), the displacement energy (E_d) and the lattice binding energy (E_l). As an example, we show results for Zr sputtered by Ar ions since other elements show a similar dependence. The default values of all three parameters (E_{sb} , E_d and E_l) are written in each chart, and the results of the simulations calculated with the default values are in all three graphs plotted in purple (marked as SRIM).

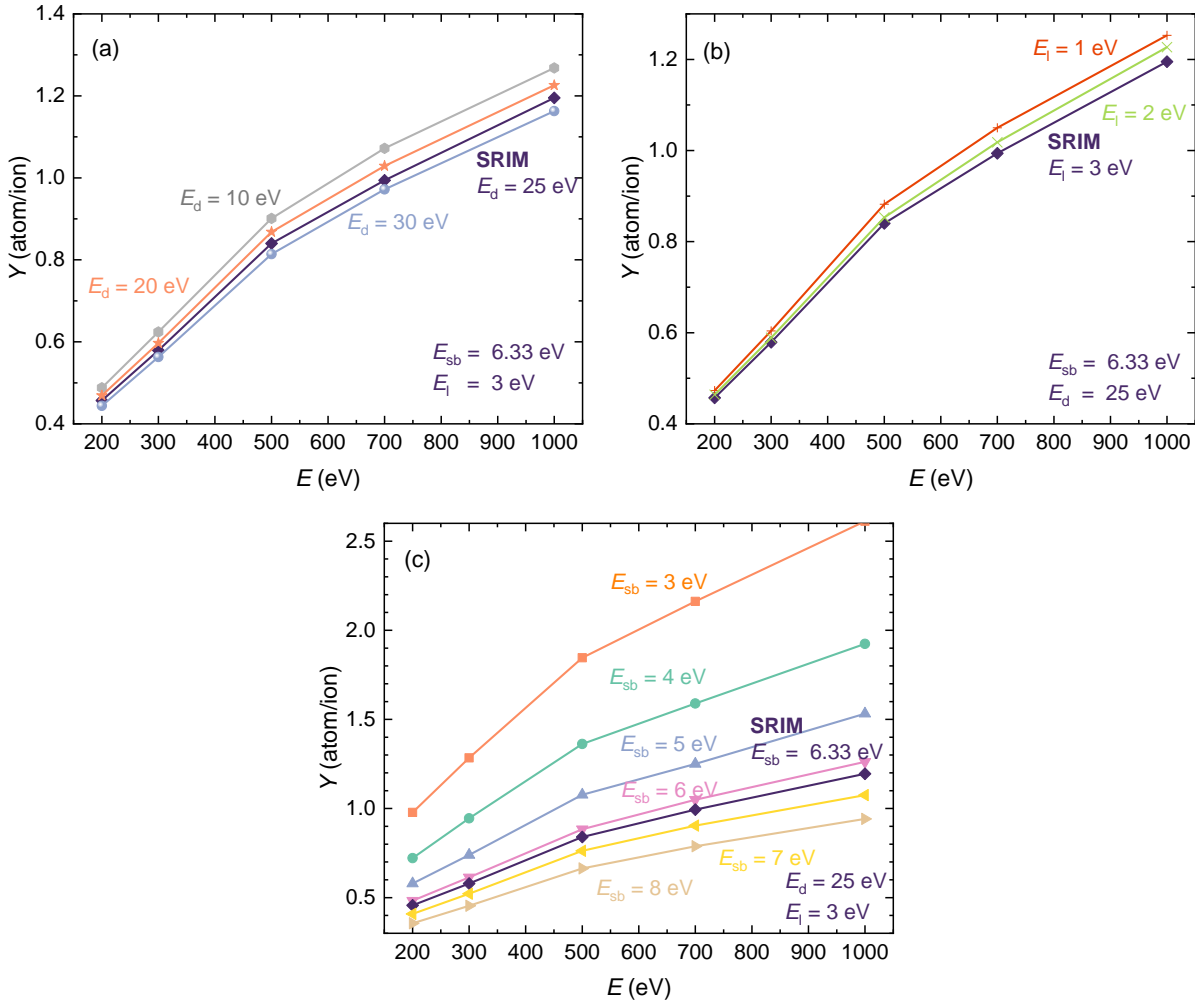


Figure 6.2: The influence of (a) the displacement energy E_d , (b) the lattice binding energy E_l and (c) the surface binding energy E_{sb} on the total sputtering yield. SRIM simulations were made using Zr target sputtered by Ar ions at different energies.

In Figure 6.2a, we show the influence of the displacement energy on the total sputtering yield. The effect is shown for different values of E_d (10–30 eV), while using default values for the lattice binding energy E_l (3 eV) and the surface binding energy (6.33 eV). The default value for the displacement energy of Zr is 25 eV. The influence of the displacement energy on the total sputtering yield is small. It slightly increases with the ion energy.

Figure 6.2b shows the role of lattice binding energy on the total sputtering yield. Values of the lattice binding energy range from 1 eV to 3 eV. The influence of lattice binding energy on the total sputtering yield is also small and increases slightly with the ion energy. The surface binding energy has the largest effect on the sputtering yield (Figure 6.2c). A small change in the surface binding energy causes a significant increase in the total sputtering yield. Differences become more pronounced at higher ion energies.

The surface binding energy (SBE) has the largest effect on the sputtering yield, while the other two parameters (the displacement energy and the lattice binding energy) have only a minor effect (a few percent). This means that the SBE is a crucial sputtering parameter. It appears in analytically derived sputtering yield equations and in the modeling of the sputtering process. Experimentally, the SBE values are not well established, therefore, in the majority of works (including the SRIM program), the heat of the sublimation is used as an approximation for the SBE. However, in the SRIM program, the surface binding energy is not defined as a simple chemical binding energy for the surface atoms; instead, the parameter also includes all of the surface non-linearities such as those which are produced by radiation damage, surface relaxation, surface roughness, surface morphology, composition, and other effects as discussed by the authors of the program [37]. The surface binding energy in SRIM is, therefore, a free input parameter, whereas the heat of sublimation is used as the default value for SBE.

To obtain sputtering yields in line with the measured values, we modified the SBE in a similar way as the authors in [92]. The displacement energy and the lattice binding energy parameters were not changed from the default SRIM values since the sensitivity analysis showed that they had a small effect on the sputtering yield. The surface binding energy was modified in such a way to obtain a good fit between the simulated and the experimental yields in the 300–1000 eV range. For the experimental data, we used the total sputtering yields that are reported in the collection by Behrisch and Eckstein [31]. In some cases, we also compared the simulated values to the experimental data that are in the study by Matsunami *et al.* [93, 94] and other more recent measurements [95]. We chose those SBE values, for which the simulated yields were closer to the experimental data rather than the fitted curves that are provided in the collections.

For sputtering of C by Ar ions, more recent sputtering yield data from Kolasinski *et al.* [96] were used. The experimental yields for B sputtering by Ar ions were not available. In this case, we relied on the experimental and simulation yield data for the sputtering of boron nitride. Chen *et al.* [97] found that simulated sputtering yields best agree with the experimental values for boron nitride if a surface binding energy of 2–3 eV is used for B. In our simulations, we use the value 2.8 eV, which is closer to 3 eV and is proportionally reduced from the default SBE by a similar amount as in the case of C. Furthermore, when performing the simulations using $E_{sb} = 2.8$ eV, we obtained a relatively good agreement with the experimental data for B self-sputtering which are reported in [31]. Nevertheless, the error between the simulated and real yields in the case of B was expected to be larger. Overall, we aimed to obtain sputtering yields which were within the 10–20 % error of the measured values for the 300–1200 eV range. However, due to the measurement and simulation uncertainties, larger errors were likely to occur.

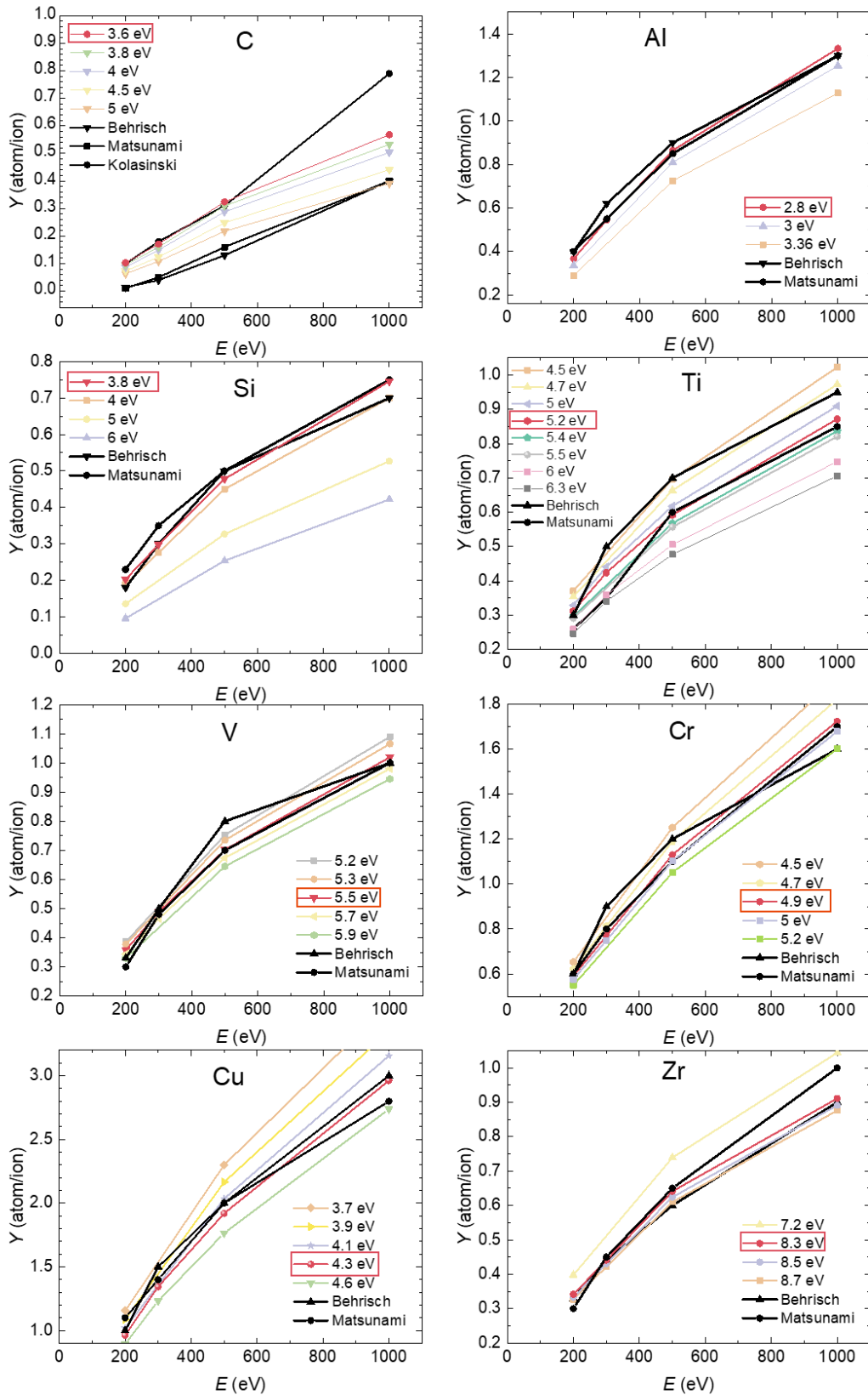


Figure 6.3: The total sputtering yield SRIM simulations and experimental data from Refs. [31, 93, 94] in dependence on ion energy for C, Al, Si, Ti, V, Cr, Cu and Zr. The values marked in red are the surface binding energy values that we chose as the best fit to the experimental values.

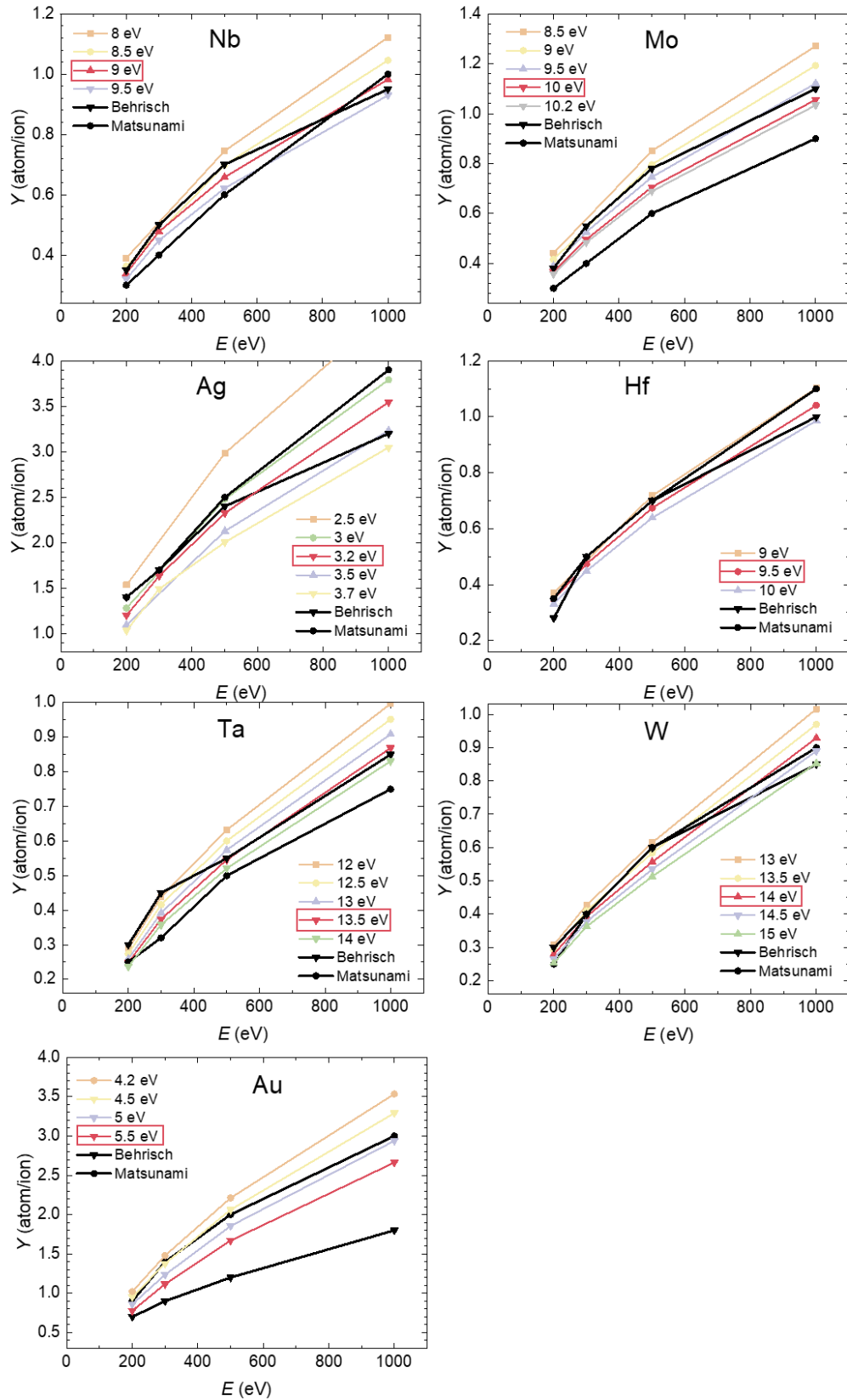


Figure 6.4: The total sputtering yield SRIM simulations and experimental data from Refs. [31, 93, 94] in dependence on ion energy for Nb, Mo, Ag, Hf, Ta, W and Au. The values marked in red are the surface binding energy values that we chose as the best fit to the experimental values.

The parameters that were chosen in the simulations are collected in Table 6.1. Note that the modified SBE for the light elements (i.e., B, C, Al, and Si) had to be decreased significantly from the default SBE values that are used by the SRIM program (i.e., the heat of sublimation). For the transition metals, particularly for the heaviest elements (e.g., Hf, Ta, W, and Au), we had to increase the SBE by a significant amount. In some cases (e.g., V and Ag), the modified SBEs were similar to the default values in the SRIM program. The lattice binding energy was 3 eV for all of the simulated elements, except for the silicon, for which it was 2 eV. The displacement energy for C was 28 eV, for Si, it was 15 eV, and for all of the other elements, it was 25 eV. These values for displacement energy and lattice binding energy are SRIM default values for each chosen element.

Table 6.1: Parameters used for SRIM simulations. Z – atomic number, M – atomic mass, ρ – mass density, E_{sb} – surface binding energy used in SRIM (i.e., the heat of sublimation), E_{msb} – modified surface binding energy. References point to the experimental data that were used for simulations of the total sputtering yield from which the modified surface binding energy was obtained. All experimental data were taken from [41], except B [97] and C [96].

Elem.	Z	M (amu)	ρ (g/cm ³)	E_{sb} (eV)	E_{msb} (eV)
B	5	10.81	2.35	5.73	2.8
C	6	12.01	2.25	7.41	3.6
Al	13	26.98	2.70	3.36	2.8
Si	14	28.08	2.32	4.70	3.8
Ti	22	47.85	4.52	4.89	5.2
V	23	50.94	5.96	5.33	5.5
Cr	24	52.00	7.20	4.12	4.9
Cu	29	63.55	8.92	3.52	4.3
Zr	40	91.22	6.49	6.33	8.3
Nb	41	92.91	8.57	7.59	9.0
Mo	42	95.95	10.21	6.83	10.0
Ag	47	107.87	10.47	2.97	3.2
Hf	72	178.49	13.31	6.31	9.5
Ta	73	180.95	16.60	8.10	13.5
W	74	183.84	19.35	8.68	14.0
Au	79	196.97	19.31	3.80	5.5

The goal was to achieve good agreement with experimental sputtering yields in the 200–1200 eV range, which is the most relevant energy range for sputter deposition processes.

Figure 6.5a shows the modified SBE, and Figure 6.5b shows the standard SBE values used by SRIM (the heat of sublimation) as a function of the atomic number (Z) of the materials studied. From the comparison, it can be seen that the SBE had to be modified significantly from the heat of sublimation values for some materials. The largest corrections had to be made for the lightest elements (B and C), where we had to decrease the value of the SBE (for C from 7.4 eV to 3.6 eV), and for the heaviest elements, where the values had to be increased (for W from 8.7 eV to 15.0 eV). Smaller changes were made for Cr, Cu, Zr, Mo, and Au, while the values for Ti, V, and Ag were close to those for the heat of sublimation.

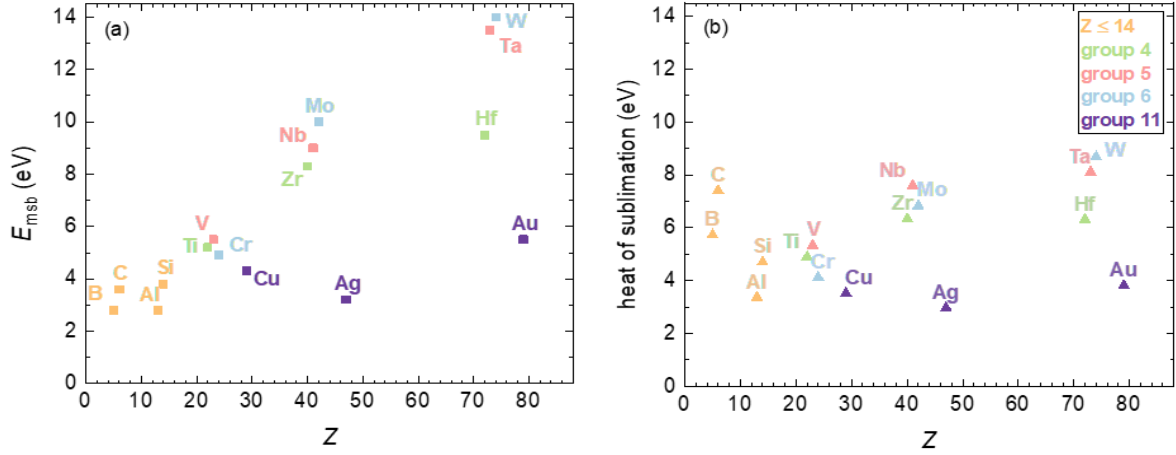


Figure 6.5: The surface binding energy in dependence on the atomic number: (a) the modified value from our SRIM simulations; (b) the heat of sublimation, which is used in SRIM as the default value for SBE.

In general, a higher atomic number is correlated with a larger SBE, whereas this is not the case for the heat of sublimation. A nearly linear relationship is observed for the elements in groups 4, 5, and 6, and for the four lightest elements (B, C, Al, and Si). For the heat of sublimation, the data are more scattered and no clear trend was observed. It should be noted that if the heat of sublimation was used in the simulations, the simulated values would differ significantly from the experimental values in some cases (sometimes even for a factor of two). The use of the modified SBE in the SRIM program was necessary and the only way to achieve good agreement between the simulated and experimental data.

Before the development of the sputtering theory, it had already been experimentally established that the total sputtering yield correlates with the reciprocal of the heat of sublimation [98]. Sigmund theoretically derived general equation for the total sputtering yield, Eq. (2.25), and its simplified form, Eq. (2.32), demonstrate such inverse proportionality. Hence, the sputtering yield is lower when the atoms near the surface are strongly bonded (i.e., a larger SBE), and it is higher when they are weakly bonded (i.e., a smaller SBE). Figure 6.6a shows the sputtering yield calculated with SRIM for different target materials as a function of the modified surface binding energies.

It can be seen that the sputtering yield is not simply an inverse function of the modified SBE. The assumption that a smaller SBE leads to a higher sputtering yield is not entirely correct. For example, the sputtering yield of group 11 elements (Ag, Au, and Cu) is much higher than the yield of the light elements (B, C, Al, and Si) and Ti, V, and Cr, even though they have very similar SBEs. Many transition metals in groups 4 to 6 have similar sputtering yields (e.g., Ti, V, Zr, Nb, Mo, Hf, Ta, and W), although they have very different SBE values. The lowest sputtering yields were observed for the light elements (B, C, and Si), which also have low SBE values. The approximate inverse proportionality with the modified SBE can be observed for the elements within the same group of the periodic table. This is true for the elements in groups 5 and 6, but not for the elements in group 4, where Y increases slightly with the SBE. In group 11, there is also a discrepancy in this trend. Thus, the relationship between sputtering yield and SBE is inconsistent.

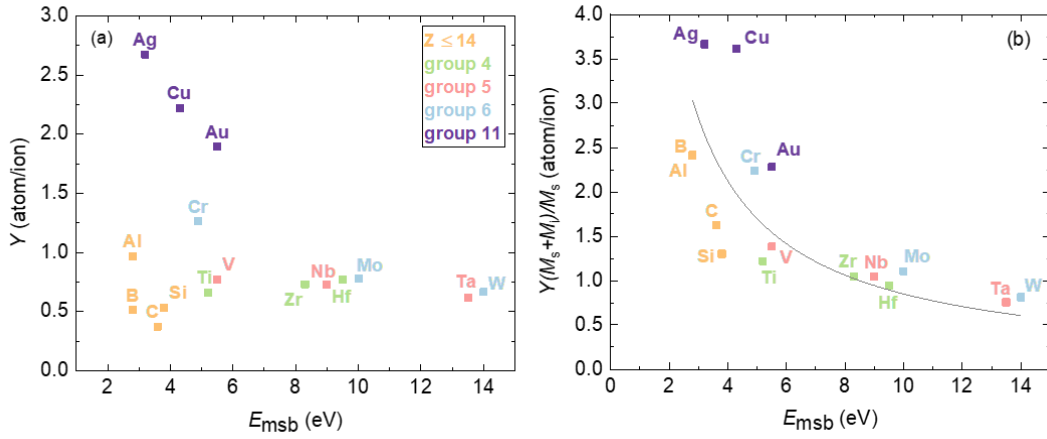


Figure 6.6: The sputtering yield in dependence on the modified surface binding energy: (a) total sputtering yield value and (b) the sputtering yield divided by the target-to-ion mass ratio for different elements. The $1/E_{\text{msb}}$ trend is found in the case of $Y / (M_s / (M_s + M_i))$ which is in accordance with the simplified sputtering yield formula, Eq. (2.32). The total sputtering yields were calculated by SRIM using Ar ions impinging normally to the surface with an energy of 600 eV.

This inconsistency in inverse proportionality can be understood by analyzing Eq. (2.32) which shows that the total sputtering yield also depends on the target-to-ion mass ratio. If the sputtering yield is normalized by $M_s / (M_s + M_i)$ and plotted as a function of the modified SBE (Figure 6.6b), then the data decrease much closer to the $1/E_{\text{msb}}$ trend. For some elements, the values deviate from this trend, therefore, it can be concluded that other factors which are contained in the complex general equation for total sputtering yield (Eq. (2.25)) must contribute to the deviations from the fitting function.

It has been reported in the literature that the total yield is also correlated with the filling of the d-shells [99]. Namely, the elements with filled s and d outer shells have the highest sputtering yield – these are the group 12 elements (Zn, Cd, and Hg). The group 11 elements (Cu, Ag, and Au) have similar shell filling (with one electron missing in the d shell). This effect, together with a low SBE, may explain the large sputtering yields observed for the group 11 elements.

6.1.2 Mass ratio

The atomic masses of the impinging ion and the target material also influence the total sputtering yield. A simplified view suggests that the sputtering yield is higher when the atomic mass of the ion is close to the atomic mass of the target material. The difference between the masses of the two colliding particles is described by the energy transfer factor Λ (Eq. (2.22)). For similar atomic masses, the Λ is close to one, and for very different masses, it is well below one (typically closer to 0.5 for Ar ions). For example, when sputtering a Ti target with Ar ions, the Λ is 0.992 ($M_{\text{Ti}} = 47.88$ and $M_{\text{Ar}} = 39.95$, similar masses), while the energy transfer factor Λ for sputtering a W target is 0.587 ($M_{\text{W}} = 183.84$, different masses). In the case of sputtering with the same ions as the target material (self-sputtering $M_i = M_s$), the energy transfer factor equals one.

The total sputtering yield as a function of the energy transfer factor is shown in Figure 6.7a. It can be seen that a similar mass of the impinging Ar ion and the target material does not necessarily result in a higher total sputtering yield; for example, the yields for Si, Ti, and V have a similar Λ . Therefore, the proximity of atomic masses is not the best indicator of higher sputtering yield. Moreover, there is no clear trend between the total sputtering yield and the energy transfer factor. For group 6 elements, the sputtering yield increases with Λ but not in the other groups. The opposite trend was observed in group 4 (i.e., Y decreases slightly as Λ approaches 1), while no clear trend is seen in group 12. The reason for the lack of trends can be understood from Eq. (2.30), where Y also depends on the factor α , which is a function of the target-to-ion mass ratio as well as the SBE (as already explained in Section 6.1.1).

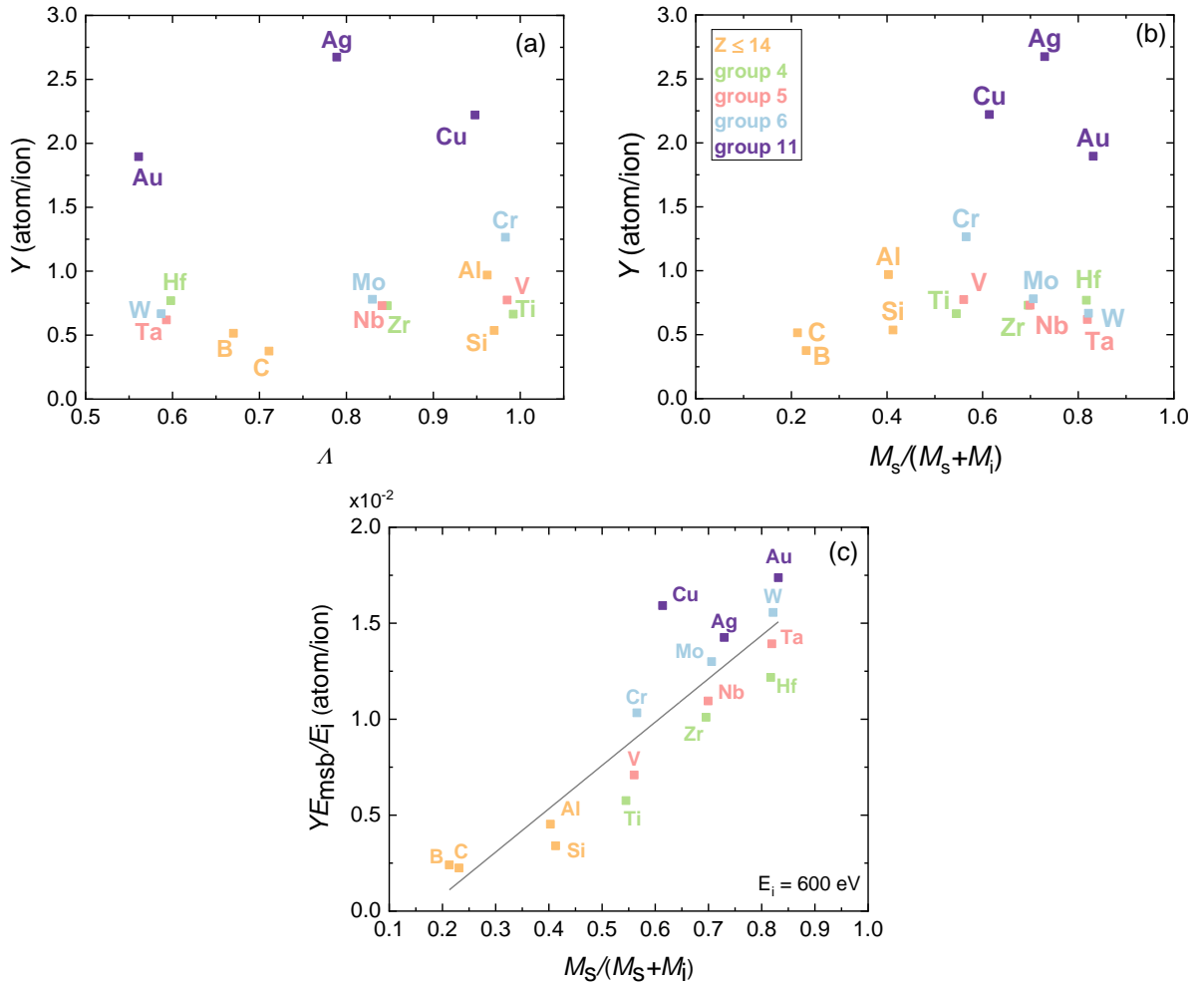


Figure 6.7: Sputtering yields (a) in dependence on the energy transfer factor Λ and (b) in dependence on the $M_s/(M_s + M_i)$, which is a product of the energy transfer factor and the dimensionless factor α . (c) Sputtering yield normalized by the E_i/E_{msb} ratio in dependence on the $M_s/(M_s + M_i)$ with a near-linear relation. Sputtering yields were calculated by SRIM using Ar ions with an energy of 600 eV.

The product of the energy transfer factor Λ and the factor α is approximately $\Lambda\alpha \approx M_s/(M_s + M_i)$. According to Eq. (2.32), the total sputtering yield linearly depends on the $M_s/(M_s + M_i)$. Therefore, for a given ion, the heavier elements should generally have a higher sputtering yield than the lighter elements. Figure 6.7b shows the total sputtering yield for the investigated target materials in the dependence on the $M_s/(M_s + M_i)$ ratio for sputtering by Ar ions with 600 eV. The trend of the sputtering yield increasing with the atomic mass is more obvious than in Figure 6.7a, however, the relationship is not unambiguous. For example, the sputtering yield increases for the elements with $Z \leq 14$ and the elements in group 11, but it decreases for the elements within groups 5 and 6. This inconsistency is a result of the surface binding energy, which strongly influences the sputtering yield. For this reason, in Figure 6.7c, we present YE_{msb}/E_i in the dependence on the $M_s/(M_s + M_i)$ as suggested by Eq. (2.32). In this case, a relatively good linear trend can be observed. It should be noted that the quantities on the y -axis are related to the SRIM simulations (i.e., Y and E_{msb}), while the values on the x axis correspond to the material properties. These plots show that the presented simple equation for the sputtering yield (Eq. (2.32)) can provide a reasonable estimate for the total sputtering yield, but the influence of the ion energy should also be analyzed as we will see in the next section.

6.1.3 Incident ion energy

The number of atoms sputtered depends strongly on the energy of the impinging ions. Higher ion energies generally lead to higher sputtering yields. The ion energy is of particular interest for sputter deposition techniques because it can be tuned to a large extent. In magnetron sputtering, the ion energy is controlled by the cathode potential. Typical cathode voltages range from 250 to 400 V for DCMS, 450 to 600 V for HiPIMS, and 1000 V or more for triode sputtering. In ion beam deposition, the ion energy is determined by the ion beam source, and it is also in the range of 1000 eV.

Simulations for the total sputtering yield were performed for ion energies in 200 eV to 1200 eV range with a step size of 100 eV (Figure 6.8). The energy dependence was fitted to a power law equation using the modified surface binding energy:

$$Y = a^* \left(\frac{E_i}{E_{\text{msb}}} \right)^{b^*}, \quad (6.1)$$

where a^* and b^* are the fitting parameters. The results are presented in Table 6.2. For most of the elements, the data are best fitted with b^* between 0.60 and 0.75, which somewhat deviates from the square root function, while for the lightest elements (B and C) a nearly linear function fits the data best. The coefficient of determination R^2 was in all of the cases better than 0.98. The total sputtering yields at three different energies are also presented in Table 6.2.

Table 6.2: Parameters obtained by fitting the sputtering yield Eq. (6.1) to the sputtering yield simulations in dependence on ion energy. We also present the coefficient of determination R^2 , the atomic number Z , the energy transfer factor A , and the simulated sputtering yields at three different energies.

Elem.	Z	A	a^*	b^*	R^2	Y (300 eV)	Y (600 eV)	Y (1200 eV)
B	5	0.670	0.0024	0.831	0.985	0.28	0.52	0.85
C	6	0.711	0.0011	0.904	0.987	0.17	0.38	0.64
Al	13	0.962	0.0104	0.699	0.983	0.55	0.97	1.40
Si	14	0.970	0.0045	0.744	0.988	0.30	0.54	0.85
Ti	22	0.992	0.0126	0.616	0.993	0.42	0.66	0.98
V	23	0.985	0.0153	0.608	0.992	0.49	0.77	1.10
Cr	24	0.983	0.0201	0.644	0.993	0.77	1.27	1.88
Cu	29	0.948	0.0319	0.658	0.993	1.34	2.22	3.29
Zr	40	0.847	0.0145	0.603	0.993	0.44	0.73	1.04
Nb	41	0.841	0.0135	0.621	0.996	0.48	0.73	1.08
Mo	42	0.830	0.0137	0.628	0.995	0.50	0.78	1.15
Ag	47	0.789	0.0429	0.639	0.993	1.64	2.67	3.86
Hf	72	0.598	0.0113	0.655	0.992	0.47	0.77	1.15
Ta	73	0.593	0.0059	0.724	0.996	0.37	0.62	0.99
W	74	0.587	0.0064	0.721	0.995	0.39	0.67	1.06
Au	79	0.561	0.0191	0.715	0.993	1.12	1.90	2.94

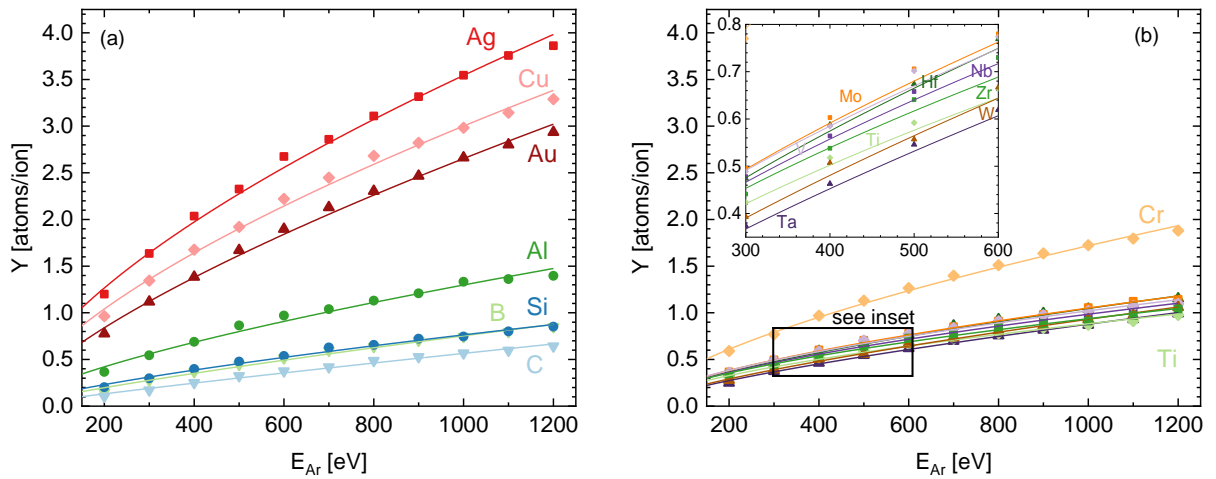


Figure 6.8: The total sputtering yield in dependence on Ar ion energy simulated by the SRIM program for different elements at normal ion impingement. For clarity, the elements are shown in two separate graphs at identical scales: (a) elements from groups 11, 13, and 14; (b) elements from groups 4–6. Due to minor differences, an inset is shown at an enlarged scale.

Figure 6.8 presents simulations of the total sputtering yield along with the fitting curves. The elements of groups 11, 13, and 14 are shown in Figure 6.8a, while elements from groups 4–6 are presented in Figure 6.8b at an identical scale to allow comparisons. In the latter case, an enlarged inset is shown. The behavior of the total sputtering yield of various elements can be compared at different energies. The power parameter is similar for the evaluated elements, with the exception of B and C, so the relative values of the sputtering yield are comparable regardless of the ion energy. In the following description, only the values at 1200 eV are discussed.

For the elements of group 11, the total sputtering yields are larger than for the elements of the other groups analyzed. They range from 3.0 (Au) to 4.0 (Ag). Surprisingly, the remaining elements in groups 4–6 have very similar sputtering yields, with values close to 1.0; an outlier is Cr, with a sputtering yield of 1.9. The lightest elements (groups 13 and 14) generally have lower sputtering yields than the transition metals, except for Al, which has a sputtering yield of about 1.4. C has the lowest sputtering yield among the elements studied at 0.64. C and B show a nearly linear dependence, while the other elements show a parabolic dependence on the ion energy.

In [63], a similar fitting approach was used as described by Eq. (6.1). Both of the fitting parameters a and b were free parameters, but their values are different from those in this work because there are some differences. In this work, we used the modified SBE values (instead of the heat of sublimation) and considered the power equation $(E_i/E_{msb})^{b^*}$ as opposed to E_i^b . We also fitted the data to a lower energy range (up to 1200 eV). Therefore, the coefficients a^* and b^* reported in Table 6.2 should be more in line with the experimental values of the sputtering yield.

The simplified Sigmund equation (Eq. (2.30)) suggests that Y increases linearly with the ion energy. However, the results of the SRIM simulations, shown in Figure 6.8, indicate that Y deviates from the linear relationship in the low-energy range (i.e., 200–1200 eV). The same is observed in the experimental data [22]. When calculating the sputtering yield using Eq. (2.30) and comparing them with the experimental values, a large overestimation of the sputtering yield is observed for most elements. In order to account for the deviation from the linear relation with ion energy, we fitted the simulated sputtering yields to the power law Eq. (6.1) using parameters a^* and b^* . In Table 6.2 and Figure 6.8, we used both free parameters to obtain the best fit to the simulated data.

Another approach would be to use only power parameter b as the fitting parameter, while parameter a can be obtained from the analytical Eq. (2.32). From the comparison of Eq. (6.1) and (2.32) it follows that:

$$a = \frac{0.45}{\pi^2} \frac{M_s}{M_s + M_i}. \quad (6.2)$$

This approach reduces the number of fitting parameters and makes the allometric Eq. (6.1) fall more in line with the sputtering theory that was developed by Sigmund. By combining the allometric Eq. (6.1) and the simplified analytical equation derived by Sigmund, we can modify the equation for the sputtering yield to account for the nonlinear behavior with ion energy:

$$Y \approx \frac{0.45}{\pi^2} \frac{M_s}{M_s + M_i} \left(\frac{E_i}{E_{msb}} \right)^b. \quad (6.3)$$

Table 6.3 shows factor a , power coefficient b , and the coefficient of determination R^2 . The comparison of R^2 in Table 6.2 and Table 6.3 proves that the new fitting approach still provides a good agreement with the simulated data. The coefficient of determination is above 0.97 for most materials, and it is slightly lower for C, Cu, and Ag.

Table 6.3: Parameters obtained by fitting the sputtering yield Eq. (6.3) to the sputtering yield simulations in dependence on ion energy.

Element	Z	a	b	R^2
B	5	0.0097	0.7381	0.978
C	6	0.0105	0.7031	0.957
Al	13	0.0184	0.7248	0.982
Si	14	0.0188	0.6623	0.980
Ti	22	0.0249	0.6806	0.987
V	23	0.0256	0.7116	0.975
Cr	24	0.0258	0.7707	0.973
Cu	29	0.0280	0.8627	0.943
Zr	40	0.0317	0.7103	0.974
Nb	41	0.0319	0.7317	0.977
Mo	42	0.0322	0.7611	0.970
Ag	47	0.0333	0.8169	0.952
Hf	72	0.0373	0.7183	0.987
Ta	73	0.0373	0.7342	0.996
W	74	0.0375	0.7748	0.984
Au	79	0.0379	0.8192	0.982

Eq. (6.3) should give more accurate results for the total sputtering yield than the linear equation Eq. (2.32) can. It is valid for Ar ion energies up to 1.2 keV. This semi-empirical relationship depends on two empirical parameters: the modified surface binding energy derived from SRIM simulations (fitted to the experimental yield data), and the power coefficient b derived from fitting the energy-dependent sputtering yields (simulated by SRIM using the modified SBE). The power coefficient b depends on the particular target material and ion type. For a given target material, the same value of b cannot be used for the other ion types because the sputtering yield as a function of energy depends on the mass of the ions. The experimental data and the SRIM simulations show a more linear relationship for sputtering by heavier ions (e.g., Kr and Xe) and a more parabolic relationship for sputtering by lighter elements (e.g., He and Ne) (see Figure 6.9). The power coefficient clearly depends on the ion mass. The usefulness of Eq. (6.3) should be verified for other ion types by performing the same fitting approach as for Ar ions in this work.

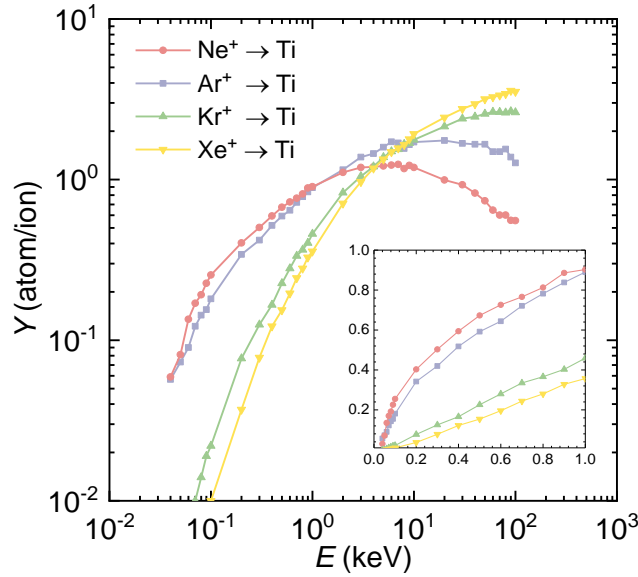


Figure 6.9: Total sputtering yield in dependence on the ion energy for sputtering Ti target with Ne^+ , Ar^+ , Kr^+ and Xe^+ ions.

When we analyze parameter b , we can observe some interesting trends which demonstrate the soundness of the second fitting approach. Figure 6.10 shows fitting parameter b as a function of atomic number Z (a similar graph is obtained when it is plotted against the $M_s/(M_s + M_i)$ ratio). Surprisingly, a sequential trend can be observed for the transition metal elements. Parameter b increases practically linearly over the individual periods of the periodic table. For example, in period 4, parameter b increases from 0.68 (Ti) to 0.86 (Cu), while in period 5, it increases from 0.71 (Zr) to 0.82 (Ag). On the other hand, very similar values for parameter b are found within the individual groups of the periodic table. The elements of group 6 have values of b that are close to 0.77. In group 5, a slight upward trend is observed, although the values of b are close to 0.73. The elements of group 4 show the strongest parabolic behavior with the ion energy, while the elements of group 11 show the least parabolic behavior (see Eq. (6.1)). Thus, for the transition metals, the trend shows a linear increase with group number. However, for the lightest elements of groups 13 and 14 with $Z \leq 14$, the opposite trend is observed – the value of b for the elements of a single group decreases with atomic number (e.g., the values for B and C are different for Al and Si).

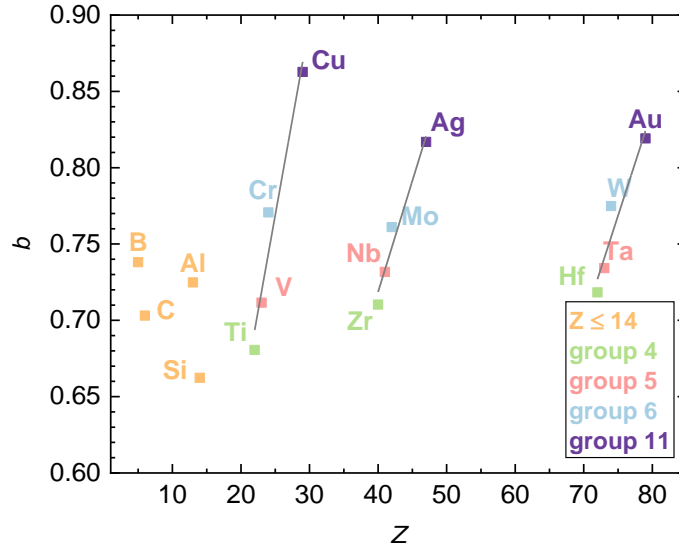


Figure 6.10: Fitting parameter b calculated from Eq. (6.2) in dependence on the atomic number.

The linear increase in parameter b for the transition metals gives us the confidence to estimate the fitting parameters for other elements of the periodic table not studied in this thesis. From the linear increase of b as a function of Z within each period, we can estimate the values of b for all elements in that period. For example, following the trend in period 4: Mn, Fe, Co, and Ni must have values between those of Cr and Cu (note the fitted linear curves in Figure 6.10 for periods 4, 5, and 6). Table 6.4 shows the calculated values of the total sputtering yield for the transition metals and some other elements. Parameter α was obtained from Eq. (6.2), and fitting parameter b was extrapolated from the linear functions in each period shown in Figure 6.10. Comparing the calculated sputtering yields with the experimental values, we find a fairly good agreement for most elements. Indeed, the transition metals not studied in this work (i.e., Mn, Fe, Co, Ni, and Zn; Ru, Rh, Pd, and Cd; Re, Os, Ir, and Pt) show relatively good agreement between the calculated data and the experimental data when available. The agreement is good for all three energies analyzed (i.e., 300 eV, 600 eV, and 1000 eV). This means that valuable sputtering yields could also be obtained at other ion energies.

The results in Table 6.4 demonstrate that the simple semi-empirical Eq. (6.3) is useful for a quick evaluation of the total sputtering yield when using Ar ions with energies up to 1200 eV. It should be noted that the simplified Sigmund equation for the total sputtering yield (Eq. (2.32)) was derived from the Thomas-Fermi potential, which is too high at lower ion energies. However, by using power parameter b for the ion energy, we can compensate for this discrepancy. In deriving Eq. (2.30), it is assumed that sputtering occurs in the linear cascade regime. This is true for higher ion energies, where the ion penetrates deeper into the solid and causes many collisions, which then lead to the emission of atoms.

At lower ion energies (e.g., below 300 eV), the surface atoms are often sputtered through a single knock-on collision as shown in the simulations of Biersack and Eckstein [43]. For this reason, it is expected that the sputtering yield values simulated with SRIM and calculated with Eq. (2.32) may differ more at lower ion energies than at higher ones. The single-knock-on regime becomes even more important when the material is bombarded at higher incidence angles. For oblique ion impingement, the α -function also depends on the ion incidence angle [57], which means that Eq. (2.30) cannot be simply reduced to Eq. (2.32). For all the above reasons, noteworthy deviations between the calculated and

experimental values can be expected, especially at lower ion energies. Other discrepancies can be attributed to the uncertainties associated with the parameters in the SRIM simulations and the experimental methods used to measure the sputtering yield.

Table 6.4: The experimental and semi-empirical values of the total sputtering yield sputtered by Ar ions with energy 300 eV, 600 eV and 1000 eV.

Elem.			300 eV		600 eV		1000 eV	
	a	b	Exp.	Semi-emp.	Exp.	Semi-emp.	Exp.	Semi-emp.
B	0.00971	0.7381	N/A	0.31	N/A	0.51	N/A	0.74
C	0.01054	0.7031	0.20	0.24	0.40	0.38	0.60	0.55
Al	0.01838	0.7248	0.60	0.54	1.10	0.90	1.50	1.30
Si	0.01882	0.6623	0.30	0.34	0.70	0.54	0.80	0.75
Ti	0.02485	0.6806	0.40	0.39	0.70	0.63	0.95	0.89
V	0.02555	0.7116	0.45	0.44	0.75	0.72	1.00	1.04
Cr	0.02578	0.7707	0.80	0.61	1.20	1.05	1.60	1.55
Mn	0.02640	0.766	N/A	0.90	N/A	1.53	N/A	2.26
Fe	0.02658	0.7941	0.70	0.77	1.20	1.34	1.50	2.01
Co	0.02717	0.8192	0.80	0.86	1.20	1.52	N/A	2.32
Ni	0.02713	0.8443	0.90	0.94	1.40	1.70	2.00	2.60
Cu	0.02800	0.8627	1.50	1.09	2.10	1.98	3.00	3.08
Zn	0.02830	0.8945	N/A	3.44	N/A	6.40	N/A	10.11
Zr	0.03171	0.7103	0.45	0.41	0.70	0.66	0.90	0.95
Nb	0.03188	0.7317	0.40	0.41	0.70	0.69	1.00	1.00
Mo	0.03219	0.7611	0.55	0.43	0.85	0.73	1.10	1.07
Tc	0.03239	0.76234	N/A	1.48	N/A	2.51	N/A	3.70
Ru	0.03268	0.7769	0.70	0.63	1.10	1.07	N/A	1.60
Rh	0.03284	0.79146	0.85	0.75	1.30	1.29	N/A	1.93
Pd	0.03315	0.80602	1.20	1.10	2.10	1.92	3.00	2.90
Ag	0.03327	0.81690	2.10	1.36	3.10	2.39	3.60	3.63
Cd	0.03364	0.83514	N/A	3.38	N/A	6.04	N/A	9.25
Hf	0.03726	0.71830	0.50	0.44	0.80	0.73	N/A	1.06
Ta	0.03735	0.73420	0.40	0.36	0.60	0.61	0.90	0.88
W	0.03746	0.77480	0.40	0.40	0.60	0.69	0.95	1.02
Re	0.03754	0.76853	0.60	0.60	1.00	1.03	N/A	1.52
Os	0.03768	0.78239	0.60	0.64	1.00	1.09	N/A	1.63
Ir	0.03775	0.79625	0.70	0.76	1.20	1.32	N/A	1.98
Pt	0.03785	0.81011	0.90	0.91	1.40	1.60	2.00	2.42
Au	0.03791	0.81920	1.10	1.00	1.90	1.77	2.70	2.69

The semi-empirical equation, Eq. (6.3), has several limitations, and it does not capture all of the complex relations included in the general sputtering yield equation, Eq. (2.25). Therefore, the most accurate approach for evaluating the total sputtering yield is to use a general equation derived by Sigmund, with corrections for sputtering at lower ion energies provided by other authors.

6.1.4 Sputtering under oblique incident angles

The descriptions have been so far limited to the perpendicular impact of the impinging ions. In some cases, sputtering is also performed at non-perpendicular angles of incidence. Figure 6.11 presents the total sputtering yield at 600 eV in 10-degree increments from the perpendicular incident angle (0°) to the grazing incident angle (89.9°). Although the absolute values of the sputtering yield are important for sputter deposition (Figure 6.11a, b), it is more informative to analyze the relative values with respect to the perpendicular ion incidence to determine the dependence for the different elements (Figure 6.11c, d). This is explained in more detail below.

For the transition metals (Figure 6.11a), the total sputtering yield remains essentially unchanged at an incidence angle of less than about 30° , whereas this angle is about 20° for the lighter elements, $Z \leq 14$ (Figure 6.11b). Behind the plateau, the sputtering yield begins to increase with incidence angle until about 70° , where the maximum peak is reached for most elements. As the incidence angle continues to increase, the total sputtering yield decreases for all elements.

In the middle range (i.e., at about $50\text{--}80^\circ$), the largest differences between the elements are observed. In contrast to the absolute values (Figure 6.11a and b), the main parameter affecting the normalized values (Figure 6.11c and d) is the atomic mass rather than the group in the periodic table. For the elements with $Z \geq 22$ (Figure 6.11c), it can be seen that the lighter elements (Ti, V, and Cr) have a clear peak in sputtering yield, which is up to 2.6 times larger than at perpendicular incidence. This is followed by the heavier elements of the next period (Zr, Nb, and Mo), where the sputtering yield is at most 1.6 times greater. For the last period (Hf, Ta and W), there is hardly any difference compared to the perpendicular incidence. The elements of group 11 follow a similar pattern but with a slight shift. The lighter elements (Figure 6.11d) show significantly more variation in total sputtering yield with ion incidence angle than the transition metals. The two lightest elements (B and C) show the largest variations, followed by Si and Al. According to the simulations, the sputtering yield for B and C at an ion incidence angle of 70° is more than eight times higher than at normal ion incidence. In absolute terms, the elements with $Z \leq 14$ (Figure 6.11b) have a higher sputtering yield at 70° than the transition metal elements, including the group 11 elements, which have the highest sputtering yield (Figure 6.11a).

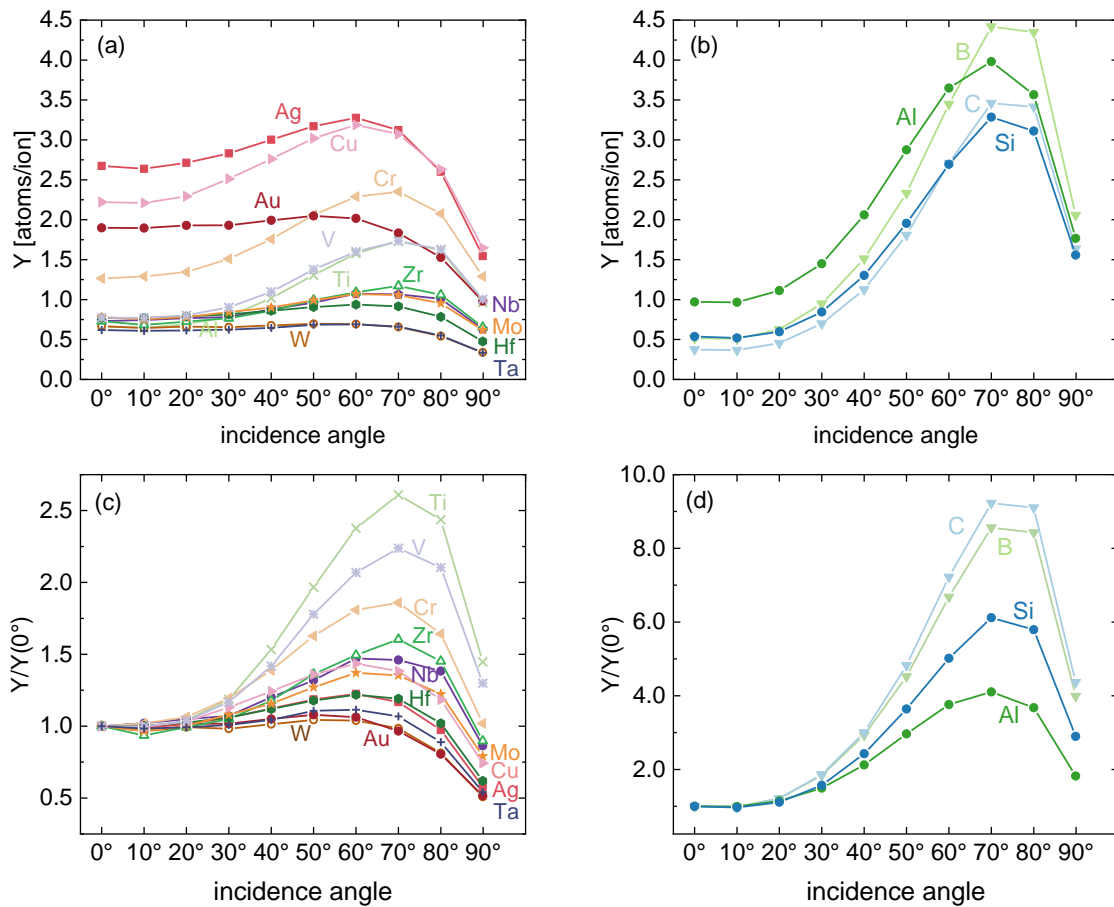


Figure 6.11: Total sputtering yield in dependence on the ion incidence angle for (a) selected transition metals and (b) selected elements with $Z \leq 14$. Normalized values against the normal ion impingement for the same elements are shown in graphs (c,d). Calculations were made by SRIM using Ar ions with 600 eV.

The total sputtering yield for sputtering under an oblique angle also depends strongly on the atomic masses of the ion and the target material. In Figure 6.11a, the total sputtering yield for the target material is the highest at oblique angles between 60° and 70°. The largest differences between the sputtering yield at an ion incidence angle of 70° and perpendicular ion sputtering are observed for the lightest elements B, C, Al, and Si (see Figure 6.11d). Among the transition metals, the lighter elements (Ti, V, and Cr) exhibit the largest relative sputtering yields when sputtered with Ar ions at an incidence angle of 70° (see Figure 6.11c). In contrast, for the heaviest transition metals (i.e., Au, W, and Ta), it is observed that the total sputtering yield remains nearly the same up to an incidence angle of about 60–70°. There is practically no increase in sputtering yield at greater incidence angles. At incidence angles above 70°, the sputtering yield begins to decrease sharply for all materials.

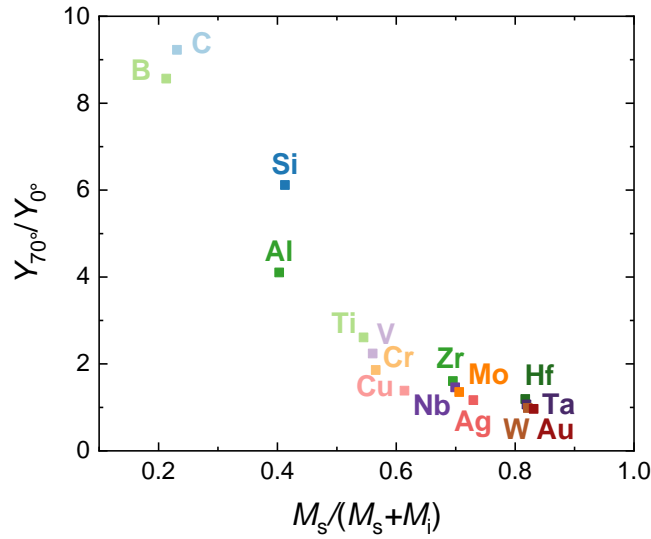


Figure 6.12: The sputtering yield at 70° Ar ion incidence normalized by the perpendicular sputtering yield in dependence of the $M_s/(M_s + M_i)$ ratio.

The atomic mass of the target material has a significant influence on the total sputtering yield for oblique ion sputtering. To further analyze this influence, we show in Figure 6.12 the relative sputtering yield $Y(70^\circ)/Y(0^\circ)$ in the dependence on $M_s/(M_s + M_i)$. A clear inverse proportionality is observed, i.e., the $Y(70^\circ)/Y(0^\circ)$ ratio decreases with the mass ratio. Figure 6.11 and Figure 6.12 demonstrate that the lighter elements sputter more intensively at the oblique ion angles than at normal ion incidence. This difference becomes smaller with increasing atomic mass of the target material and it practically disappears for the heaviest elements. Therefore, a viable approach to increase the sputtering yield of the lighter elements, which generally have the lowest sputtering yield at normal ion incidence, is to sputter them at higher angles or to use targets with high surface roughness.

The experimental sputtering yield data for ion bombardment under an oblique angle are rather scarce. In the collection by Behrisch and Eckstein [31], the data are available for several elements that were analyzed in this work (Al, Ti, Cu, Zr, Ag, Ta, W, and Au) which were sputtered by 1.05 keV Ar ions. In Figure 6.13, we show a comparison between the simulated and empirical data for the selected elements. In general, the agreement is good for most of the materials except for Al and Ti, where larger deviations from the experimental data are observed. Overall, the simulated data show the same trends with regard to the ion incidence angle as the experimental data. For example, the experimental data also demonstrate that the heavier elements have much smaller variations in the dependence on the ion incidence angle than the lighter elements. Furthermore, the highest experimental values for the sputtering yield are also observed between the 60° and 70° incidence angles, as demonstrated by the SRIM simulations.

The sputtering yield at a normal incidence is usually considered to be the most reliable value, and it is generally used to obtain information on the sputtering yields at an oblique incidence using semi-empirical models. The evaluation of the sputtering yields under an oblique angle as an overview of the semi-empirical fitting equations is well presented in Table 3 of [58].

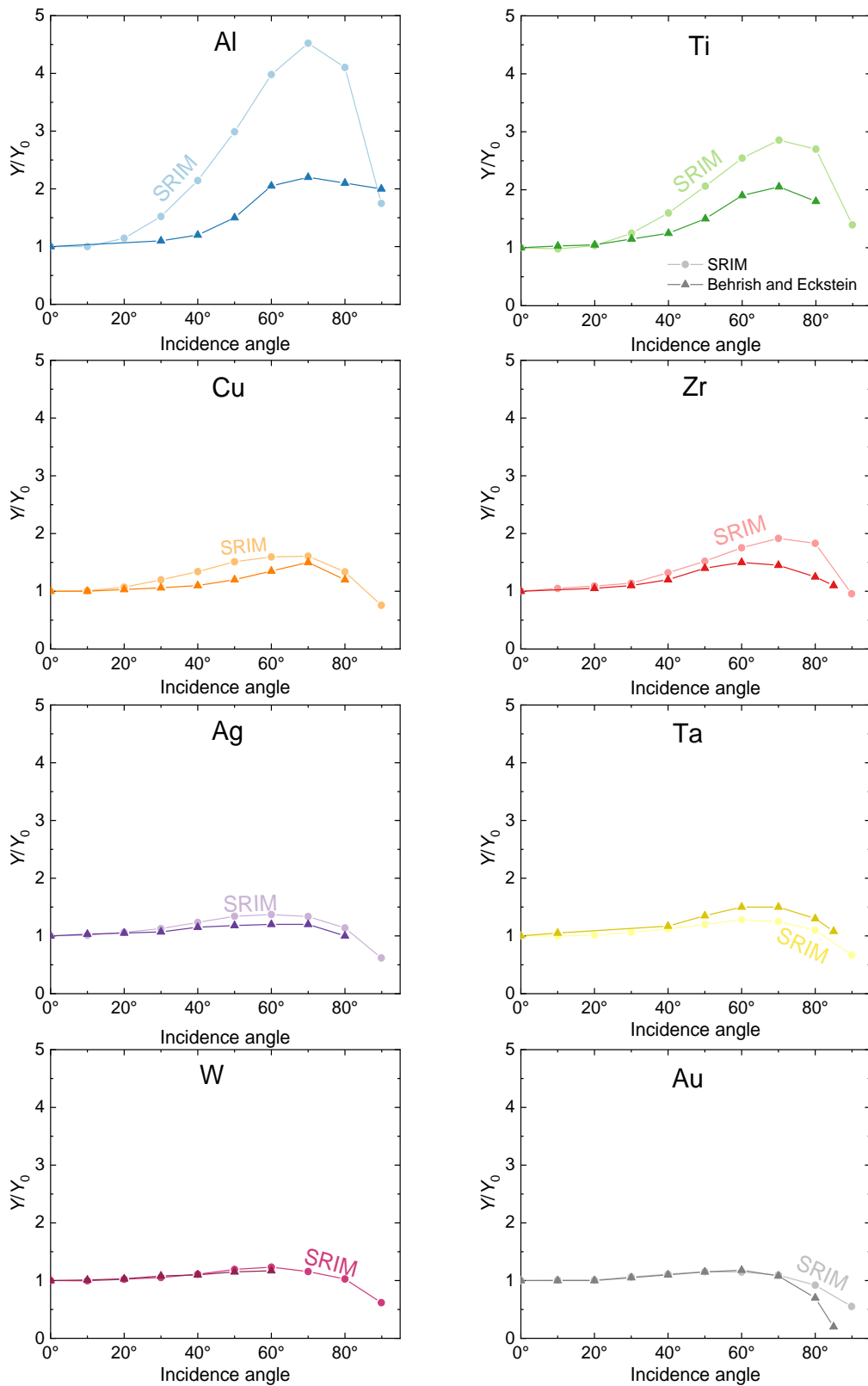


Figure 6.13: The total sputtering yield for sputtering under an oblique ion angle using Ar ions with energy 1.05 keV. Experimental data was taken from the collection of Behrish and Eckstein [31].

6.2 Differential Sputtering Yield

The total sputtering yield is defined as the number of sputtered atoms per incident ion into whole hemisphere. It is an important parameter for sputtering, but for practical applications, the differential sputtering yield is often more relevant. It can be calculated as the number of sputtered atoms into a chosen polar and azimuthal angle.

The growth of thin films is determined by the deposition rate, which depends linearly on the differential sputtering yield (see Eq. (4.3)) [91]. The atom flux from the sputtering sources directed to a specific region of the substrate determines the film growth process. All of the target and ion properties discussed in the previous section also affect the differential sputtering yield, but are not again discussed in this chapter. Instead, the general trends in differential sputtering yield of the elements studied will be discussed.

The analysis of the differential sputtering yield simulation data was made for three ion energies: 300 eV, 600 eV, and 1200 eV, which roughly correspond to the typical ion energies in DCMS, HiPIMS, and triode sputtering.

The differential sputtering yield represents the polar distribution of sputtered atoms when multiplied by the number of impinging Ar ions (10^6). The points in the polar diagrams represent the intervals in 10-degree steps. Thus, the value at 5° includes the emission of the target atoms in the predominantly normal direction, i.e., in the interval below 10° .

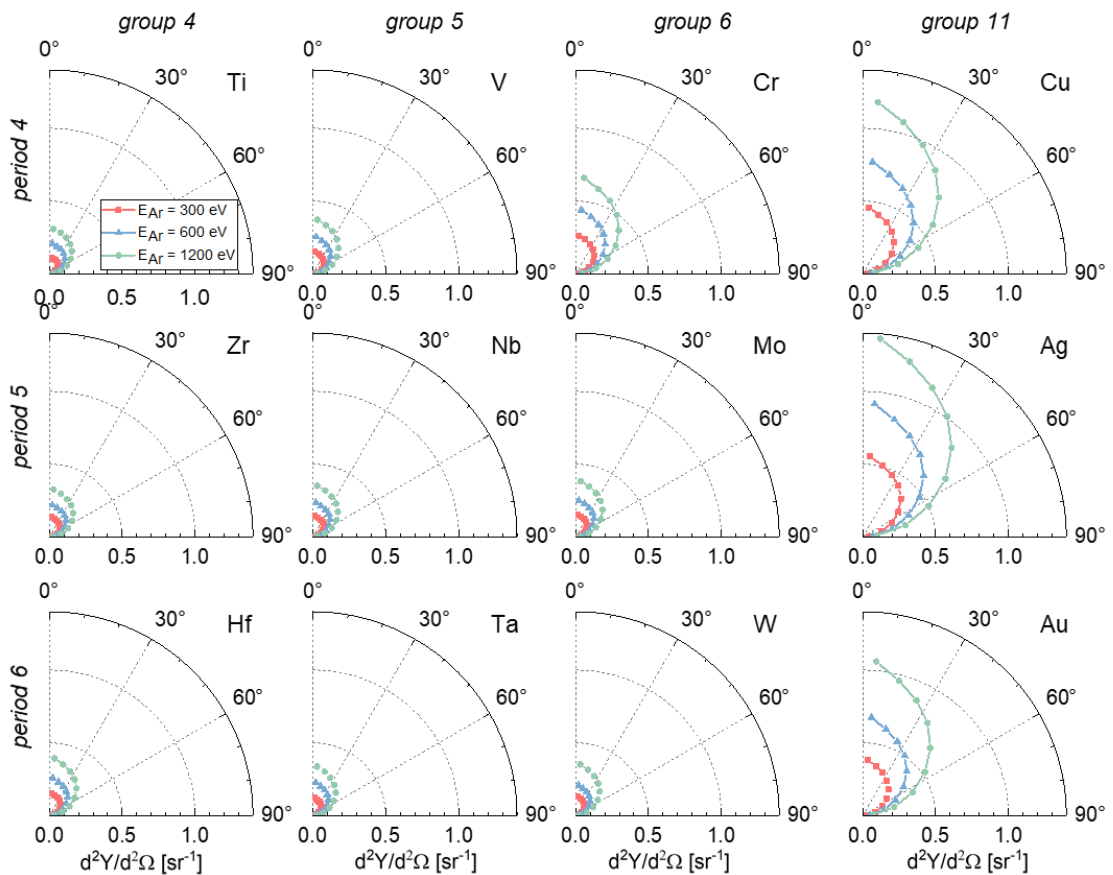


Figure 6.14: Angular distribution of sputtered metallic elements (groups 4–6 and 11) with 300 eV (red), 600 eV (blue), and 1200 eV (green) energy Ar ions at perpendicular incidences. The graphs show the number of sputtered atoms in a particular polar angle interval.

Figure 6.14 presents the differential sputtering yields for each of the transition metal elements studied. They are arranged as they are found in the periodic table. Integrating the individual values over the polar and azimuthal angles gives the total sputtering yield at each energy, as shown in Figure 6.8. In agreement with the results from Figure 6.8 and the accompanying discussion, the absolute values of the differential sputtering yield are very similar for the elements in groups 4-6. The values are slightly lower for Ti and higher for Cr; however, the values for the group 11 elements are much higher. At least visually, the angular dependence shows no particular difference between the individual elements.

For the light elements in groups 13 and 14, the results are not straight-forward (Figure 6.15). For Si, the results appear to be comparable to the angular distribution observed for the transition metals. In contrast, the other three light elements (B, C, and Al) show unusual distributions. For the smaller emission angles, i.e., those pointing in the perpendicular direction, the simulated differential sputtering yield is much higher than expected. This is especially the case for angles that are below 10° , with results that are as high as 2.09 sr^{-1} (for boron at 1200 eV), 2.54 sr^{-1} (for Al at 600 eV), and even 3.70 sr^{-1} (for Al at 1200 eV).

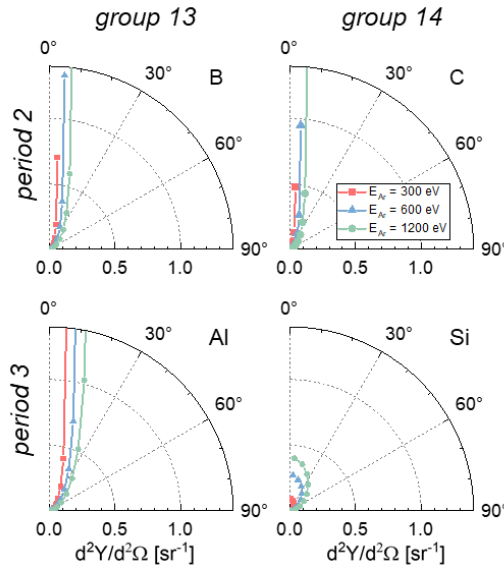


Figure 6.15: Angular distribution of sputtered light elements (groups 13 and 14) with 300 eV (red), 600 eV (blue), and 1200 eV (green) energy Ar ions at perpendicular sputtering directions. The graphs show the number of sputtered atoms in a particular polar angle interval.

While the polar graphs in Figures 6.14 and 6.15 are informative, the emission angle dependence can be better extracted from the standard cartesian graphs. Figure 6.16a presents the transition elements from groups 4-6 and 11. As in the total sputtering yield, the group 11 elements have a far higher differential sputtering yield in comparison to those from groups 4-6. Aside from Cr (higher) and Ti (slightly lower), all of the remaining elements from these three groups essentially behave in an identical way, with negligible differences between them. The angular dependence is monotonously decreased, with a slight change of slope at around 40° . Among the light elements (Figure 6.16b), Si has a similar angular dependence as the group 4-6 elements. However, for B, C, and Al (Figure 6.16b), the simulations gave unexpectedly high values of the differential sputtering yield in the emission angles that were below 40° . While one can accept the somewhat higher values at 35° and 25° (possibly also at 15°), the values at 5° are not realistic. Thus, the results that are presented in Figure 6.16b should be taken as an output of the simulation only, rather than a verified conclusion.

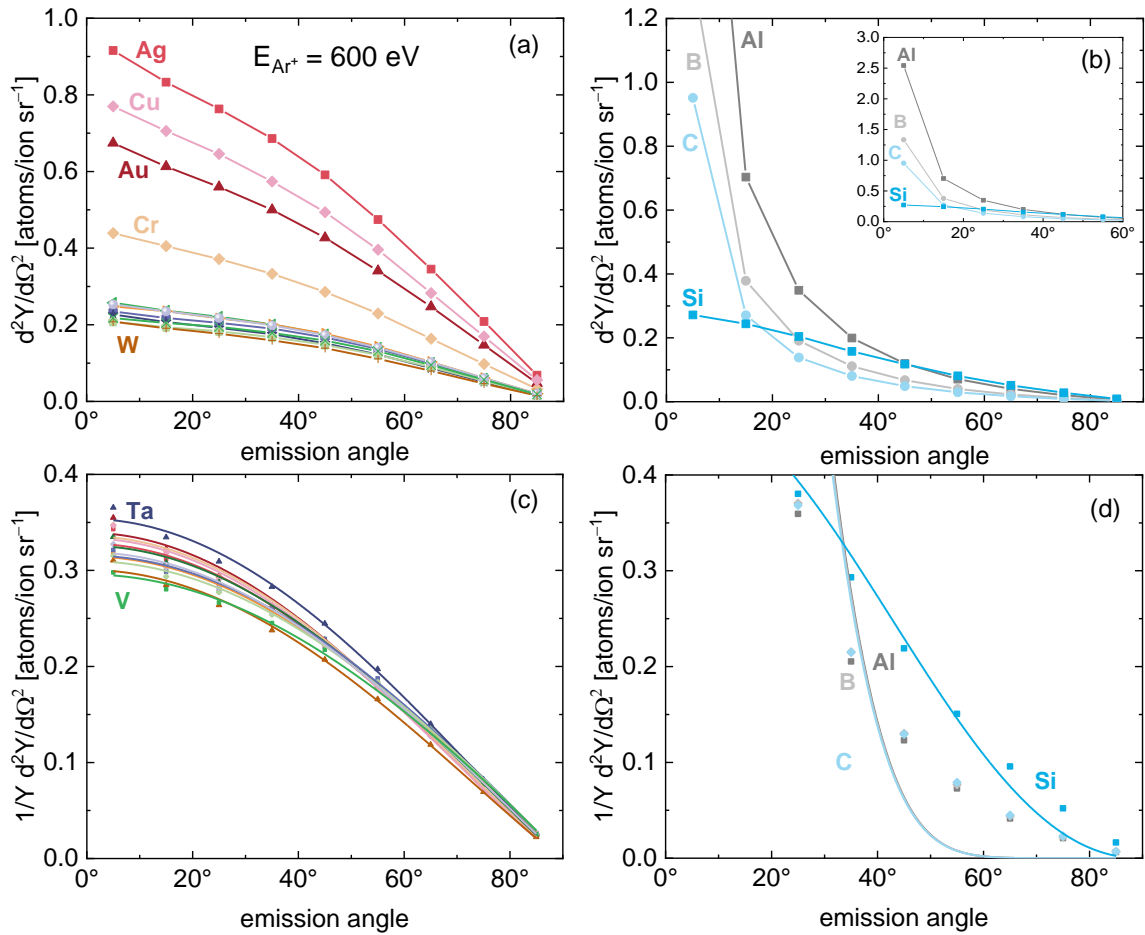


Figure 6.16: Polar distribution of the differential sputtering yield for metallic elements (a) and light elements (b) for sputtering with 600 eV Ar ions. Normalized distributions for the two collections are given in (c,d). Graphs for both collections have identical scales; in the case of light elements, the inset also shows excessively high values at low emission angles.

Another way of presenting the angular dependence of the sputtered atoms is to divide the differential sputtering yields by the total sputtering yield of the respective element. For the transition metals, these results are shown in Figure 6.16c. Surprisingly, all of the studied elements, including group 11, essentially follow the same curve. There are only slight variations among them, thus, only the lowest (V) and the highest (Ta) ones are marked. This suggests that the emission angle dependence of the differential sputtering yield is the same regardless of the metal type. Normalizing the already questionable differential sputtering yields of the light elements does not make much sense; nevertheless, even Si deviates significantly in comparison to the metals (Figure 6.16d). Therefore, we believe that even the results for Si should be taken with reservation.

The differential sputtering yields were also fitted according to the cosine law:

$$\frac{1}{Y} \frac{d^2Y}{d\Omega^2} = A \cos^y \theta, \quad (6.4)$$

where A and y are the fitting parameters. The results are given in Table 6.5. In line with the data from Figure 6.16, there is not much variation between the elements.

Table 6.5: Fitting parameters for cosine approximation of the differential sputtering yield curves; the coefficient of determination R^2 is also given.

Element	A	y	R^2
Si	0.487	2.172	0.989
Ti	0.308	0.973	0.998
V	0.319	1.035	0.998
Cr	0.336	1.116	0.997
Cu	0.333	1.132	0.996
Zr	0.296	0.951	0.998
Nb	0.316	0.980	0.998
Mo	0.315	1.004	0.999
Ag	0.328	1.101	0.995
Hf	0.326	1.060	0.998
Ta	0.329	1.077	0.997
W	0.325	1.087	0.997
Au	0.340	1.141	0.995

In Sigmund's theory of sputtering, the angular distribution of the sputtered atoms is assumed to be a cosine function [46, 50]. Such a dependence is attributed to the isotropic flux inside the amorphous target material [41]. A cosine distribution is usually not observed experimentally, especially when measuring at very low or very high ion energies. The angular distribution of the sputtered material is often fitted using the power fitting parameter y [100]:

$$\frac{1}{Y} \frac{d^2Y}{d^2\Omega} \propto \cos^y \theta. \quad (6.5)$$

Our simulations of angular distribution show that the fitting parameter y is close to one for the majority of the investigated materials (see Table 6.5). Therefore, the SRIM simulations show essentially a cosine angular distribution of the sputtered atoms. The exception is Si, where y was 2.172, while for elements B, C, and Al, we could not determine the power fitting factor because the simulations show a highly directed flux near the surface normal. Such an unrealistic atom distribution for the elements with $Z < 14$ was also observed by other authors [101-103].

Several possible reasons were suggested as the source of this error. Shulga [101] suggested that highly directed atom emission for the light elements results from errors in the calculations of particle trajectories within the material. Wittmaack [102] identified several problems in the earlier versions of the SRIM program (specifically, the 2000 and 2003 versions). The author attributed the sputtering yield artifacts to an incorrect approximation of ion-target scattering and too low electronic stopping power in the low-energy range. Furthermore, they identified the differences between the detailed and quick calculation mode, which are still present in the latest version of SRIM. Wittmaack also suggested that the problems in simulations might be caused by the assumed non-random atom spacing in the solid. As a result, the sputtering yields that were simulated by earlier SRIM versions were compared to experimental values, and they were too large for $Z_i/Z_s < 0.7$ and too small for $Z_i/Z_s > 2$. Hofsäss *et al.* also noticed that SRIM simulations of differential sputtering yield do not agree with experimental data for targets with

$Z < 14$ [103]. They concluded that SRIM is optimized for ion ranges, straggling, energy loss and damage profiles, but the results of sputtering are not exact, only rudimental.

In our work, we compensated for any differences between the calculated and the experimental values by modifying the surface binding energy parameter. Other authors proposed additional sources of the error in the SRIM, such as the algorithm for searching the collision partners when an ion approaches the surface [104] or ignoring the extremely small scattering angles [105]. We examined the collision cascades in the SRIM simulations for all of the investigated target materials (see Section 4.2), but we did not find any preferential direction for scattering in the case of the elements with $Z < 14$. The nuclear stopping powers that are essential in SRIM simulation are uncertain for lower ion energies and could be the source of error in the simulation. We cannot identify the specific source of the error in SRIM, which results in highly directed atom emission in the case of light elements.

In the literature, under-cosine, over-cosine, and cosine angular distributions of sputtered material are reported. In one of the earliest reports, Wehner and Rosenberg [106] measured the angular distribution of Ni, Ge, Fe, Mo, and Pt for normal Hg^+ ion bombardment with energies that were between 100 eV and 1 keV. Their experiments demonstrate an under-cosine angular distribution. More material was ejected to the sides than in the direction normal to the target. Tsuge *et al.* [107] also measured an under-cosine distribution for the Au, Al, and NiFe targets, which were bombarded by 1 keV Ar ions. They related the under-cosine spatial distribution to the crystallographic orientation. Oyarzabal *et al.* [108, 109] performed measurements of an angular distribution for a very low ion energy range (75–225 eV) by analyzing the sputtering of C and Mo. Their measurements show a heart-like distribution. The differential sputtering yields which were measured for several metals using heavier ions (Kr and Xe) also showed a heart-like distribution [89]. Turner *et al.* [110] measured the angular distribution for Cu which was sputtered by Ar ions with an energy of 510 eV. The distribution differed from the cosine distribution as more particles were sputtered near the target normal (between -10° and 10°) and at approximately 45° . Surla *et al.* [111] measured an under-cosine distribution for Mo which was sputtered by Ar ions with an energy of 750 eV. Chini *et al.* [112] analyzed the sputtering of a Ge target with Ar ions between 600 eV and 4000 eV. The authors found the distribution best fitted to an over-cosine function, with the power parameters between 1.25 and 1.32.

Computer simulations that were performed by Yamamura *et al.* [100] using the Monte Carlo simulation program ACAT showed that the degree of the over-cosine distribution depends on the energy of the incident ions. By analyzing a Fe target, they simulated over-cosine angular distributions for higher ion energies (above 2000 eV) and under-cosine angular distributions for lower ion energies (below 500 eV). They claim that the over-cosine angular distribution is due to the geometrical asymmetry near the surface, while the under-cosine distribution for low ion energy sputtering was explained by an anisotropic velocity distribution of the cascade near the surface. Feder *et al.* [113] measured and simulated the sputtering of Ag with Ar ions. The shape of the angular distribution also qualitatively agreed with their simulations. The same authors sputtered Ge with Ar and Xe ions and compared the measurements with the simulations that were performed using the TRIM.SP code [114]. They measured a cosine-like angular distribution for 1 keV Ar ions and an under-cosine distribution for the sputtering with 1 keV xenon ions. Hence, very different angular distributions were observed experimentally and by simulations. According to the SRIM simulations that were performed in this work, the angular distributions of the sputtered atoms are cosine for all of the elements (except for the elements with $Z < 14$), and they do not change with an increasing ion energy in the 300–1200 eV range.

It should be noted that the sputtering is also influenced by the roughness, composition, and crystallinity of the target material [43], however, these parameters are not included in the SRIM program, but they often cannot be avoided in the experimental studies. Recent measurements and simulations by Cupak *et al.* [12] show that when rather rough surfaces were bombarded by ions under large incidence angles, a more-or-less uniform distribution of the atoms resulted around the normal of the surface. On the other hand, the earlier simulations where the atomic-scale surface roughness had been implemented in the TRIM code show that the roughness significantly affected the total sputtering yield for the low ion energies and the non-normal angles of incidence [115]. Similarly, Yamamura *et al.* [100] emphasize the importance of roughness. Based on their sputtering simulations, authors concluded that the roughness reduces the degree of the over-cosine distribution since the rougher surfaces have a larger effective surface area in comparison to the flat surfaces. Schlueter *et al.* [116] found that polycrystalline metals with randomly oriented grains do not sputter with the same sputtering yield as amorphous materials. They explained that the key reason for this is attributed to the linear collision sequences rather than the channeling effect. All of the above-discussed effects can influence the significant discrepancies between the experimentally determined angular distributions and the ones simulated by the SRIM program.

6.2.1 Angular distribution for oblique ion incident angle

The discussion on the differential sputtering yield has so far been limited to a perpendicular incidence of the bombarding ions. Here, we discuss the results of the simulations for oblique ion incidence angles. In Figure 6.16, we present the polar graphs of the sputtered atoms, which are similar to Figure 6.14 and Figure 6.15. While yet another parameter (incidence angle) to the existing ones (element and energy) would further increase the complexity of the topic, we limited our work to one incidence angle (60°). At these conditions, we analyzed the angular distribution for the selected elements at one ion energy (600 eV) and separately for three different ion energies for sputtering Cr.

Several trends can be recognized for the sputtering at oblique ion incidence angles. Figure 6.17 shows the angular distribution for the sputtered elements in groups 4, 5, and 6 by Ar ions impinging at a 60° angle with an energy of 600 eV. The symmetry of the atom distribution depends on the group of the periodic table. The elements in group 4 (Ti, Zr, and Hf) appear to have a more asymmetric distribution than the elements in group 5 (Cr, Mo, and W) despite them having similar masses (for the elements in the same period). The most symmetric distribution is expressed by the elements in group 11 (Cu, Ag, and Au). However, the distribution also depends on the atomic mass of the target material. Within an individual group of elements, the lightest elements show the most asymmetric distribution (see columns in Figure 6.17). For example, the lightest element in group 4 (Ti) experienced the largest asymmetry, while the most symmetric distribution can be observed in the heaviest element (Hf). Similar observations are valid for the other two analyzed groups of elements. The most symmetric distribution is observed in the sputtering of the heaviest analyzed element (Au). On the other hand, the asymmetry of the distribution does not appear to be associated with the surface binding energy. For example, Ti and Au have similar surface binding energies, but very different angular distributions of sputtered atoms.

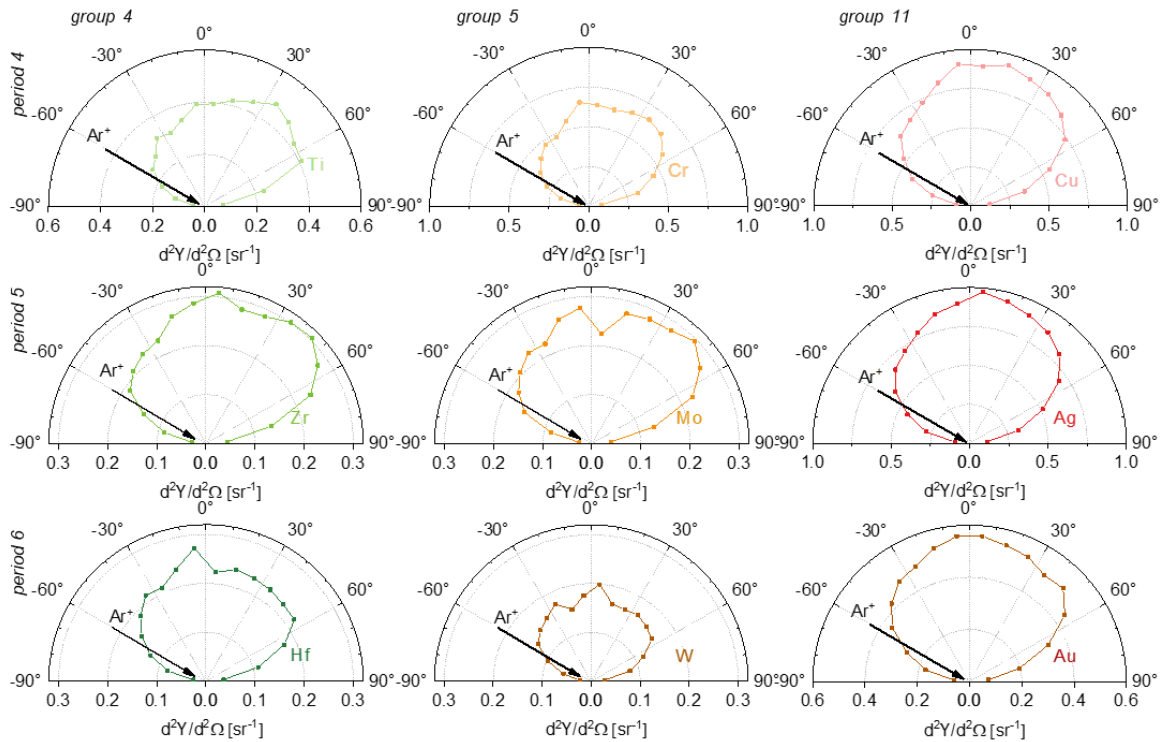


Figure 6.17: Angular distribution of sputtered atoms for selected elements (Ti, Cr, and Cu; Nb, Mo, and Ag; Hf, W, and Au) bombarded by Ar ions at 60° angle and energy of 600 eV.

Finally, we look at the situation of the same element (Cr) at three different energies. Figure 6.18 shows an example of the Cr distribution when it was sputtered by Ar ions at a 60° angle at 300 eV, 600 eV, and 1200 eV. Figure 6.18a shows the absolute values of the differential sputtering yield. As these values substantially depend on the energy, the angular asymmetry is more visible if the values are normalized to the total sputtering yield. This is shown in Figure 6.18b, where it can be observed that the symmetry increases with the ion energy, i.e., the sputtering at lower ion energies causes a more asymmetric distribution of the atoms than at higher energies.

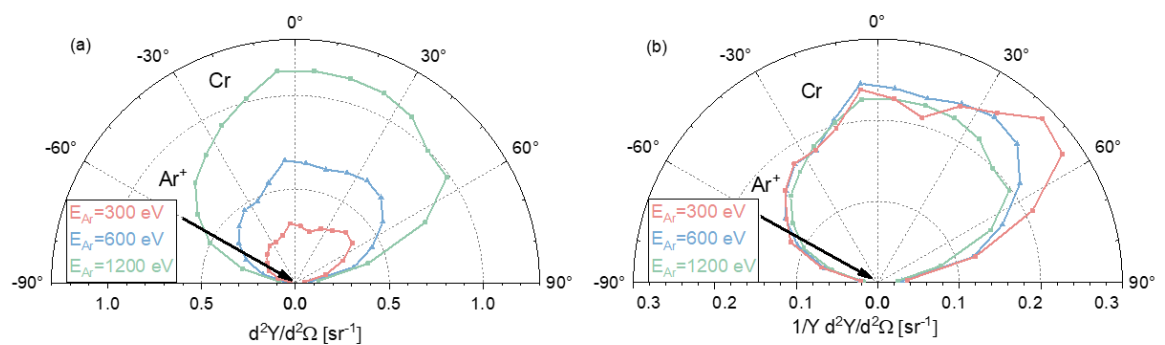


Figure 6.18: (a) Angular distribution of Cr atoms sputtered by Ar ions at 60° ion incidence for different ion energies. (b) Angular distribution normalized with the total sputtering yield.

This trend could be explained by the deeper penetration of the ions when a solid is bombarded by ions of higher energy. Higher-energy ions cause more collisions in the solid, which results in a more uniform distribution of the collision cascades, while the lower-energy ions cause fewer cascades with a more asymmetric distribution, and consequently, an asymmetric emission of the atoms from the surface (see Figure 6.19).

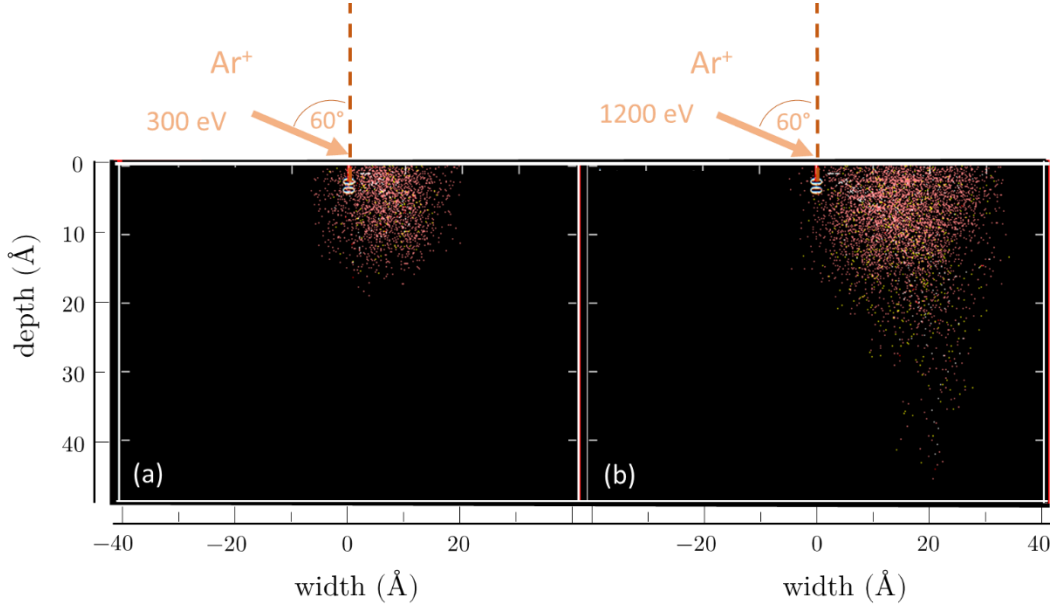


Figure 6.19: Cross section of collision cascades for sputtering a Cr target with (a) 300 and (b) 1200 eV Ar ions at 60° incident angle.

Lautenschläger *et al.* [117] measured the angular distribution of Ti atoms. They sputtered the target material perpendicularly and at 30° and 60° with 1 keV Ar. Authors also performed measurements and simulations for different Ar ion energies. They showed that sputtering is more isotropic for higher energies of incident ions and for lower incidence angles of the ions. Such sputtering enables more collisions inside the solid material. Consequently, this leads to fully developed collision cascades which result in a more isotropic distribution of the sputtered particles.

6.3 Energy Distribution of Sputtered Particles

The energy distribution functions (EDF) of sputtered atoms were evaluated for the same elements as the sputtering yield. We analyzed the energy distribution of sputtered atoms for a hemisphere (i.e., total EDF), the energy distribution functions for specific polar intervals (i.e., angular EDF), and the corresponding average energies of sputtered particles.

The total and angular energy distribution data were evaluated for three Ar ion energies impinging normal to the surface. Figure 6.20 shows a typical EDF in logarithmic and linear scales with labeled different features of the function. Typically, the function has a low-energy peak, located at approximately $E_{sb}/2$, and an energy tail, which decreases as approximately E^{-2} and extends up to the maximum atom energy. In some EDFs, there can also be one or two broad high-energy peaks present. For each distribution, we evaluated the peak of EDF and the full-width at half-maximum (FWHM), which are more clearly visible in linear scale (Figure 6.20b). We will analyze the tail of EDF, the maximum energy

of sputtered atoms, and the high-energy peaks if present. These parameters are discussed in dependence on the element position in the periodic table (i.e., group and period), and in dependence on the ion energy.

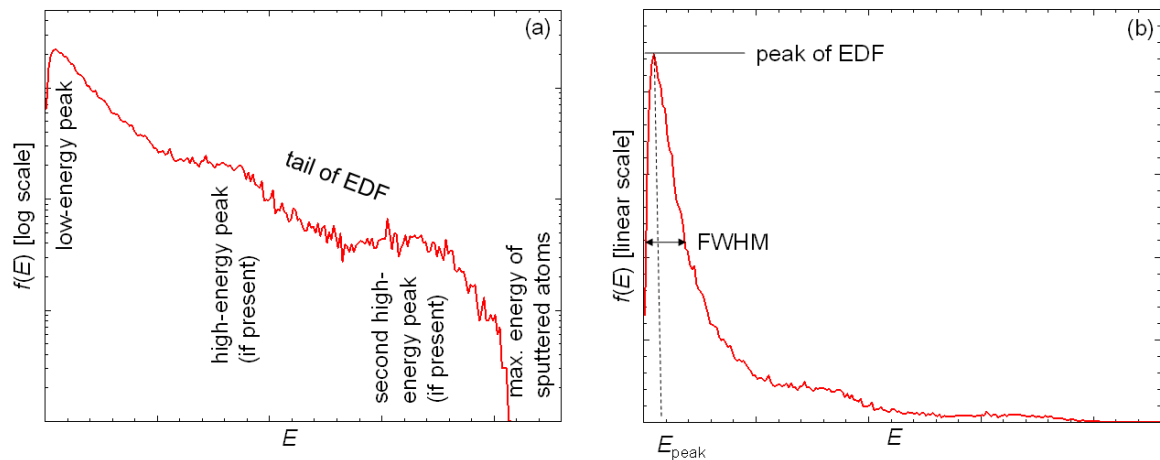


Figure 6.20: An example of an EDF in (a) logarithmic and (b) linear scale.

The total and angular EDF for ions impinging with 300 eV, 600 eV and 1200 eV are shown in Figures 6.21–6.23, respectively. The black lines represent the total EDF and the colored ones the angular EDFs. The angular distributions show the EDFs for atoms sputtered in 10° intervals (e.g., the interval between 0° and 10° is denoted as 5°). The graphs in each figure are arranged in the same order as the elements in the periodic table. We also fitted the simulated distributions to the analytical equations for the total EDF derived by Thompson and Sigmund. The dashed black line in the graphs shows the fit using the Thompson EDF [45] and the dotted black line using the Sigmund EDF fitted to simulated total EDFs. When fitting Sigmund and Thompson EDFs to the simulated ones, the normalization factors (A_T and A_S) and the power parameters in the functions were free parameters (see Chapter 2.2).

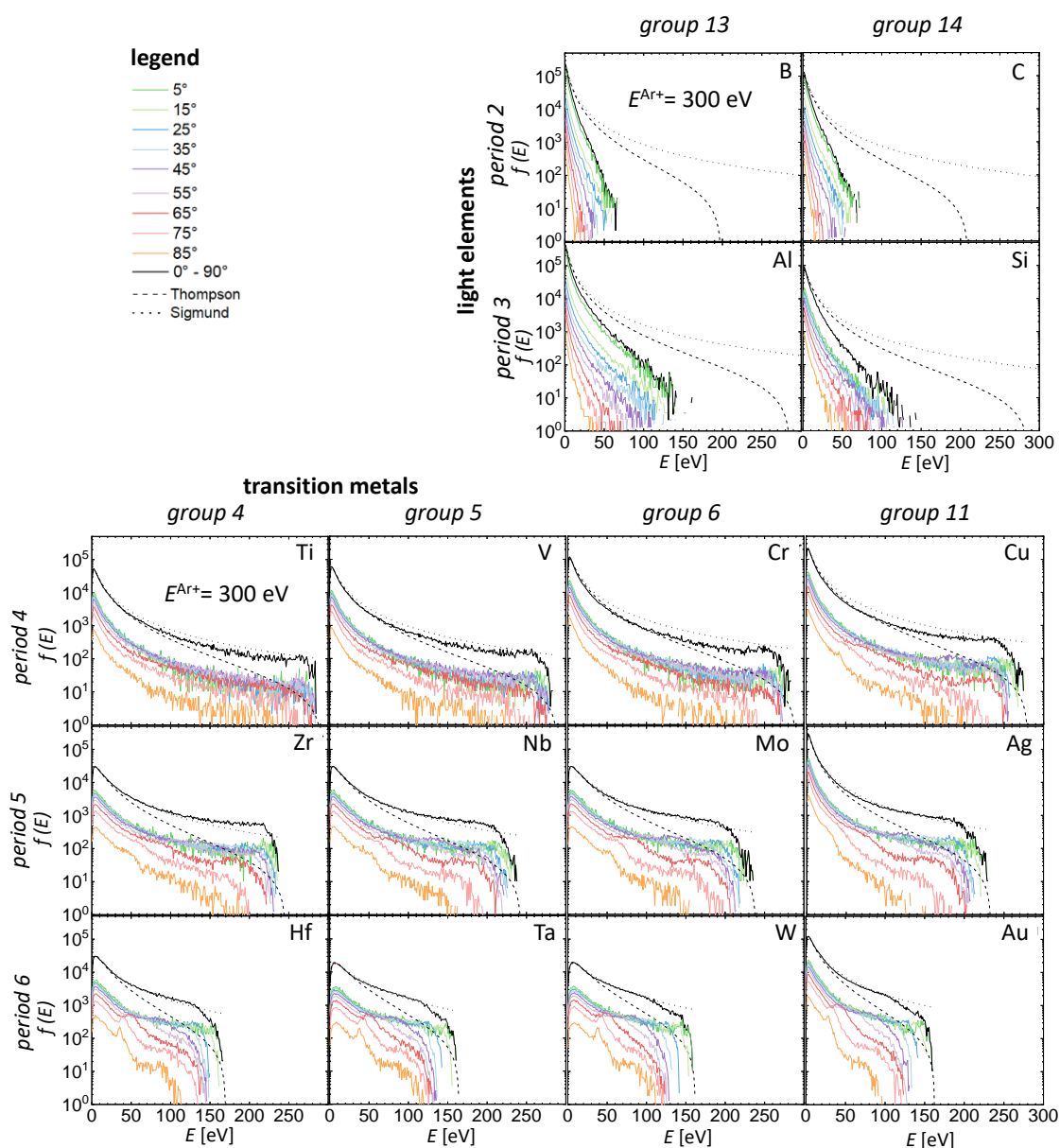


Figure 6.21: EDFs for selected elements obtained from SRIM simulations and analytical functions of Sigmund and Thompson for Ar ions impinging perpendicularly on the surface with the energy of 300 eV. The simulated total EDFs are plotted with a black line while the angular EDFs are shown in colored lines. Thompson and Sigmund EDFs are plotted with black dashed and dotted lines, respectively.

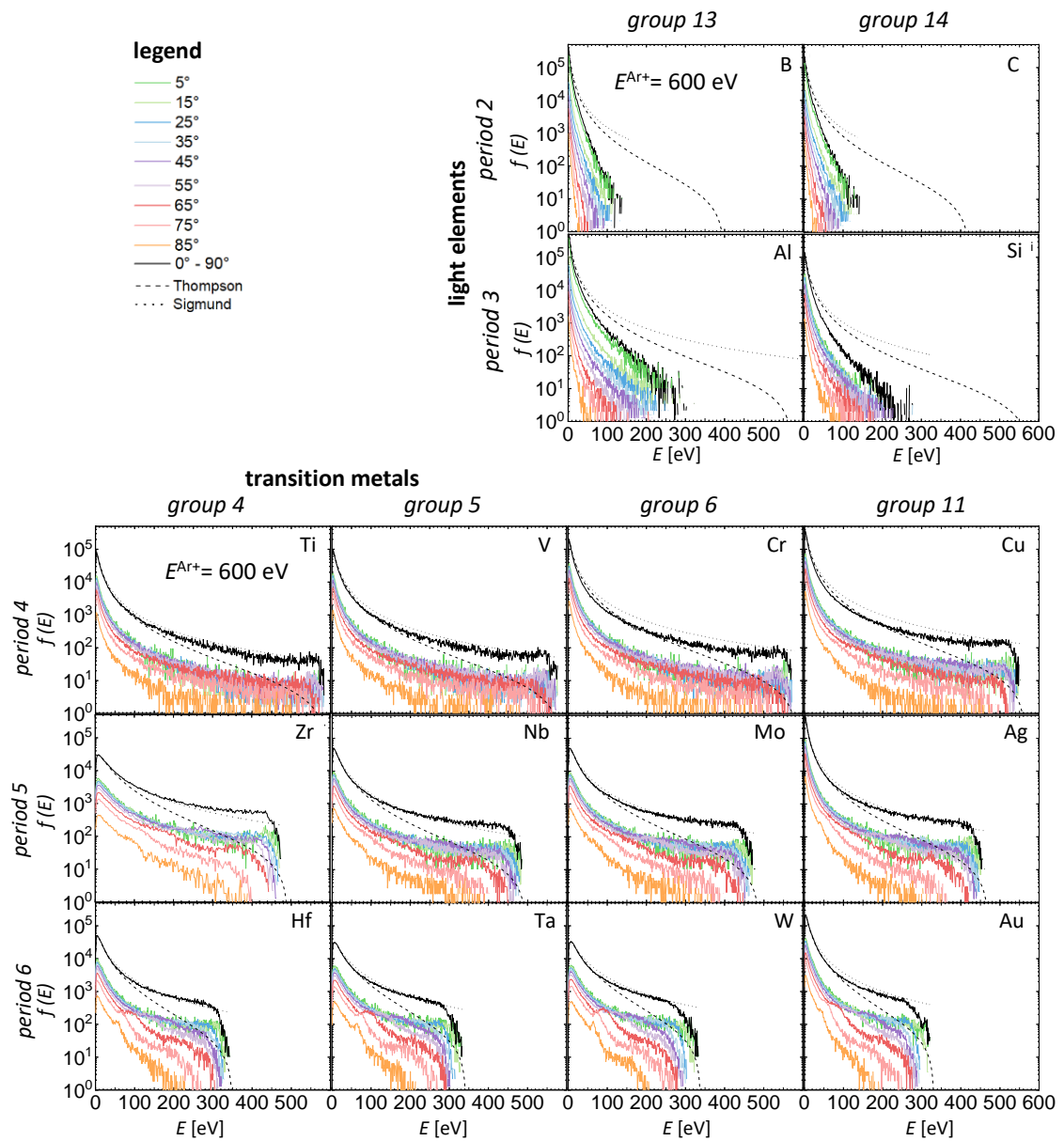


Figure 6.22: EDFs for selected elements obtained from SRIM simulations and analytical functions of Sigmund and Thompson for Ar ions impinging perpendicularly on the surface with the energy of 600 eV. The simulated total EDFs are plotted with a black line while the angular EDFs are shown in colored lines. Thompson and Sigmund EDFs are plotted with black dashed and dotted lines, respectively.

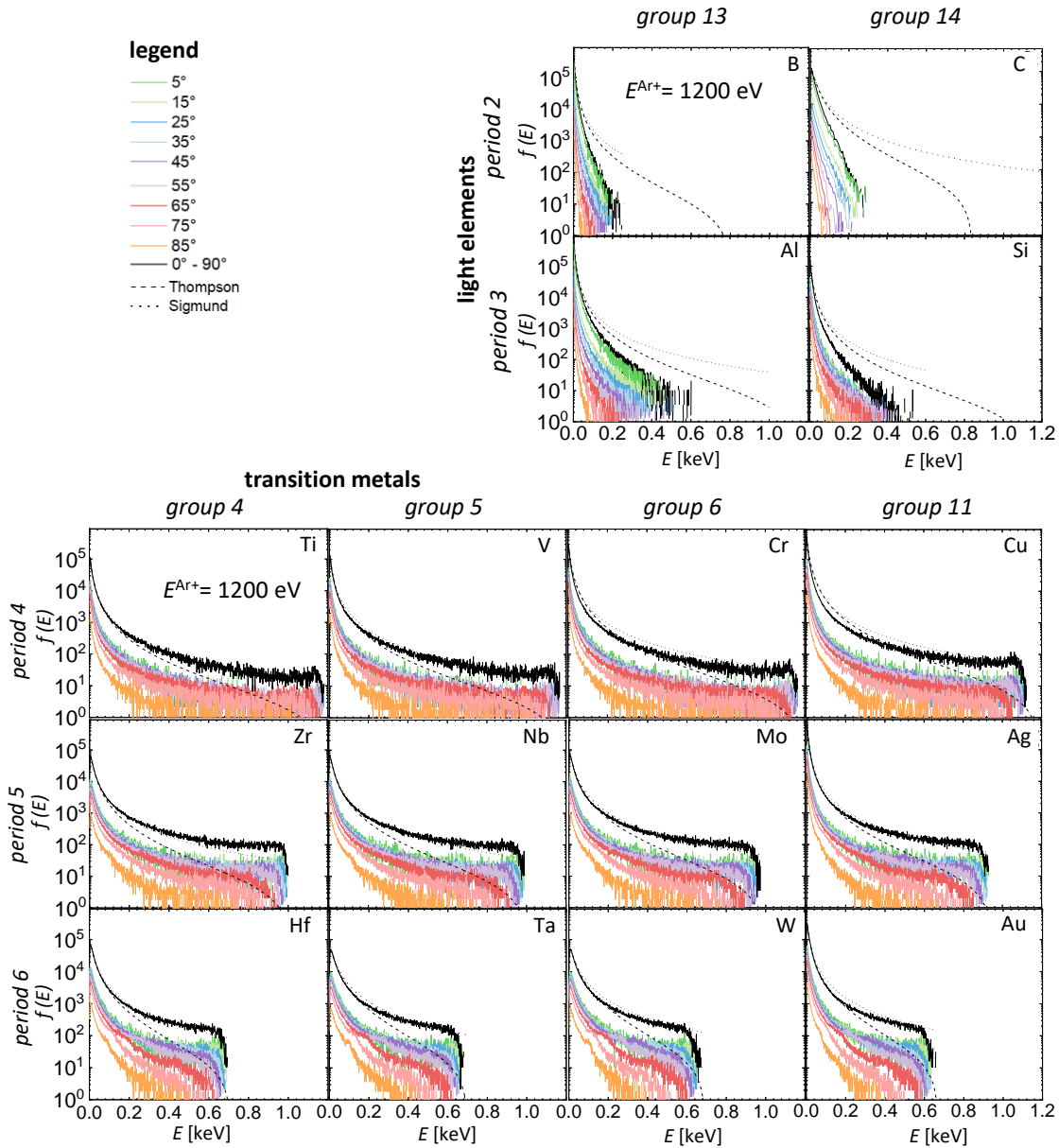


Figure 6.23: EDFs for selected elements obtained from SRIM simulations and analytical functions of Sigmund and Thompson for Ar ions impinging perpendicularly on the surface with the energy of 1200 eV. The simulated total EDFs are plotted with a black line while the angular EDFs are shown in colored lines. Thompson and Sigmund EDFs are plotted with black dashed and dotted lines, respectively.

6.3.1 Total energy distribution functions

In the analysis, we discuss different parts of total EDFs: the overall shape of distributions, the low-energy peak, FWHM, the energy tail and the maximum energy of sputtered atoms. Furthermore, we attempt to find correlations between these parameters and the element arrangement in the periodic table.

Figures 6.21–6.23 show a relatively good agreement between the simulated total EDFs and analytical Sigmund and Thompson distributions. In general, the agreement is good for the transition metals but not for the investigated light elements (B, C, Al, Si). For the

transition metals, the Sigmund distribution better fits the simulated EDFs than the Thompson distribution. The largest differences are in the energy tail where the Thompson distribution decreases faster than simulated EDFs and the Sigmund function. For lighter transition metals (Ti, V, Cr), the differences in the energy tail are smaller than in heavier elements. The larger deviation between the Thompson distribution and simulated EDFs occurs due to fitting restrictions in the tail of the function (see Eq. (2.21)) while the Sigmund distribution does not have such a restriction.

All total EDFs presented in Figures 6.21–6.23 exhibit a low-energy peak, positioned at approximately $E_{sb}/2$ and a high-energy tail decreasing as E^{-2} . In order to compare the position of the low-energy peak and FWHMs for EDFs of different elements we normalized the total EDFs for sputtering with 300 eV and 1200 eV Ar ions (Figure 6.24). The EDFs for selected materials show approximately the same shape of EDF at 300 eV and 1200 eV, therefore we do not present the EDFs for sputtering with 600 eV ions. Hence, the general shape of the total EDFs according to SRIM simulations (and also Sigmund and Thompson EDFs) does not change with the ion energy. The light elements in groups 13 and 14 (B, C, Al, Si) show sharper low-energy peaks than the transition elements.

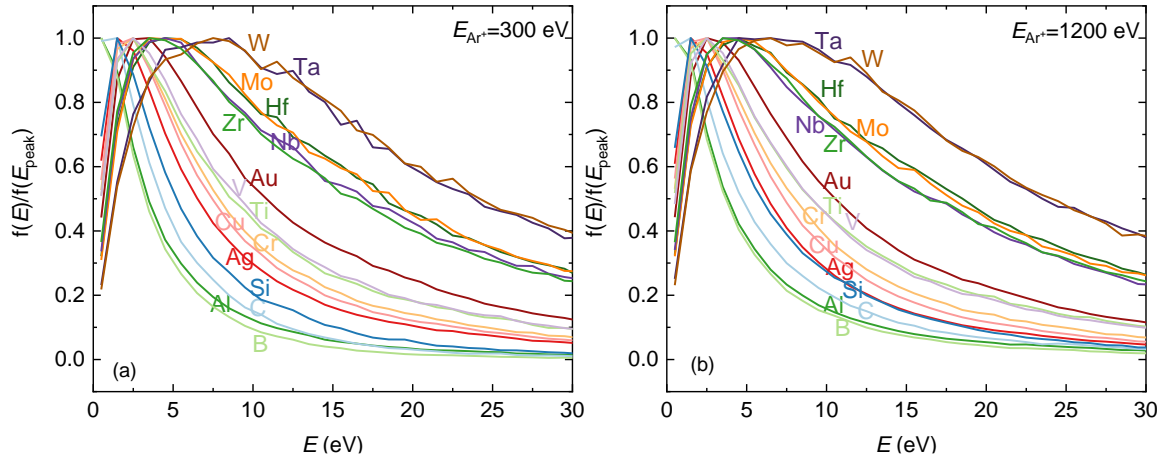


Figure 6.24: Normalized EDFs simulated by SRIM for sputtering with (a) 300 eV and (b) 1200 eV Ar ions.

In Figure 6.25, we present the position of the low-energy peak in dependence on the atomic number. Several trends with regard to the position of the element in the periodic table can be recognized. The low-energy peak moves towards higher values with increasing atomic number for elements within individual groups. The change is the highest for elements in group 6, somewhat lower for the ones in group 5 and lower for elements in group 4. The changes are the smallest for elements in group 11 – these elements have the lowest values due to the lowest surface binding energy, since $E_{peak} \approx E_{msb}/2$. When comparing elements in individual periods, the low-energy peak increases with the group in a somewhat inconsistent manner – the lowest peaks are observed in elements of group 11, the peaks then increase sequentially with increasing group from 4 to 6. The light elements in groups 13 and 14 do not show any specific trends. It should be mentioned that for all elements, the peak position is practically independent of the energy of impinging Ar ions.

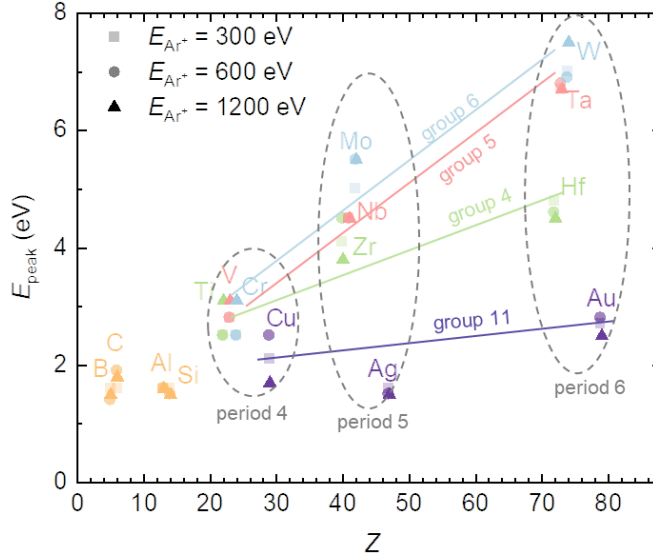


Figure 6.25: Low-energy peak in dependence on the atomic number. Elements in the same group are colored with the same color and with different shades and symbols for different energies (300 eV, 600 eV and 1200 eV Ar ions).

In the low-energy part, both analytical distributions fit well to the simulated EDFs. The positions of the low-energy peaks in total EDFs simulated by SRIM are collected in Table 6.6 together with peak positions calculated from the Sigmund-Thompson distribution (i.e., $E_{\text{msb}}/2$). The differences between the peak positions obtained from simulated EDFs and from Sigmund-Thompson distribution are the largest for the light elements (B, C, Al and Si). The simulated EDFs show a very narrow FWHM and a rapid decrease in the distribution behind the peak, which differs significantly from the Sigmund or Thompson distributions for light elements. In section 6.2, we analyzed the differential sputtering yields obtained from SRIM simulations. The results showed a highly preferential sputtering of the light elements (B, C, Al and Si) in the normal direction. Such unrealistic spatial distribution was also observed in simulations performed by Hofsäss *et al.* [103]. Based on our simulations (analysis of differential sputtering yield and energies) and based on similar findings of other authors [101, 102] we conclude that SRIM does not produce accurate simulation results for elements with $Z < 14$.

The analysis of the low-energy peak positions for transition metals obtained from SRIM simulations and the Sigmund-Thompson distribution also show some differences (see Table 6.6). The peak positions from SRIM simulations show a small dependence on the ion energy. For all transition elements, the peak position for sputtering with 300 eV ions is up to 8 % higher than for sputtering with 600 eV and 1200 eV ions. The peak positions for sputtering with 600 eV and 1200 eV are closer together than the peak positions for sputtering with 300 eV and 600 eV. Overall, SRIM simulations suggest that the peak position slightly decreases with Ar ion energy, however, results are ambiguous with regard to the position of the element in the periodic table. On the other hand, the peak position in the Sigmund-Thompson distribution is solely determined by the surface binding energy (i.e., the peak is close to $E_{\text{sb}}/2$). Hence, according to the Sigmund and Thompson sputtering theory, the peak position depends neither on the ion energy nor the ion mass (see e.g. Chapter 2 in [41]). In order to compare peak positions obtained by SRIM and Sigmund-Thompson distribution, we calculated the average energy of the peak position from SRIM simulations for three analyzed ion energies: 300 eV, 600 eV and 1200 eV (see Table 6.6). The comparison is shown in Figure 6.26. In general, the correlation is good, however, the peak positions obtained by SRIM are overall about 10 % lower than the peak positions

from the Sigmund-Thompson distribution (note that the slope of the fit in Figure 6.26 is approximately 0.9). The discrepancy is larger for the light elements (B, C, Al, Si), therefore, we excluded them from the analysis.

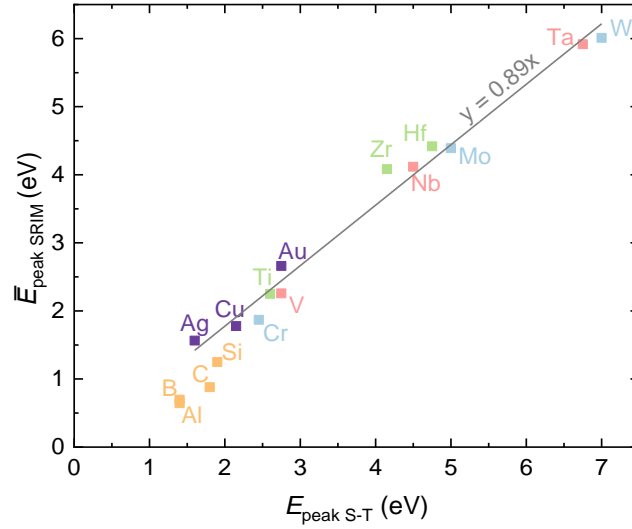


Figure 6.26: Comparison between the peak positions calculated from the Sigmund-Thompson distribution and the ones obtained from SRIM simulations.

Table 6.6: The low-energy peak positions calculated from the Sigmund-Thompson (S-T) distribution and obtained from SRIM simulations for sputtering with 300 eV, 600 eV and 1200 eV Ar ions. Element parameters: Z – atomic number, M – atomic mass, E_{msb} – modified surface binding energy.

Elem.	Z	M (amu)	E_{msb} (eV)	E_{peak} (eV)		$E_{\text{peak}}^{300\text{eV}}$		$E_{\text{peak}}^{600\text{eV}}$		$E_{\text{peak}}^{1200\text{eV}}$	
				S-T	SRIM	SRIM	SRIM	SRIM	SRIM		
B	5	10.81	2.8	1.4	0.49	0.72	0.72	0.72	0.64		
C	6	12.01	3.6	1.8	0.75	0.94	0.95	0.88			
Al	13	26.98	2.8	1.4	0.65	0.72	0.72	0.70			
Si	14	28.08	3.8	1.9	1.15	1.25	1.35	1.25			
Ti	22	47.85	5.2	2.6	2.25	2.25	2.25	2.25			
V	23	50.94	5.5	2.8	2.27	2.25	2.25	2.26			
Cr	24	51.99	4.9	2.5	1.95	1.83	1.83	1.87			
Cu	29	63.55	4.3	2.2	1.83	1.75	1.75	1.78			
Zr	40	91.22	8.3	4.2	4.15	4.05	4.05	4.08			
Nb	41	92.91	9.0	4.5	4.25	4.05	4.05	4.12			
Mo	42	95.95	10.0	5.0	4.55	4.35	4.27	4.39			
Ag	47	107.87	3.2	1.6	1.61	1.55	1.53	1.56			
Hf	72	178.49	9.5	4.8	4.55	4.35	4.35	4.42			
Ta	73	180.95	13.5	6.8	6.25	5.75	5.75	5.92			
W	74	183.84	14.0	7.0	6.35	5.85	5.83	6.01			
Au	79	196.97	5.5	2.8	2.72	2.71	2.55	2.66			

Figure 6.27 shows FWHM of investigated total EDFs. The FWHM exhibits similar behavior as the low-energy peak position, i.e. FWHM moves towards higher values with the atomic number within specific groups of the periodic table. In group 6, the FWHM increases from 9.5 eV for Cr to 26 eV for W. The increase is similar in group 5, while in group 4, slightly lower increases between periods are observed (from 10 eV to 18 eV). On the other hand, in group 11, the FWHM does not change significantly; the values are between 6 eV and 10 eV. The trends for elements in particular periods are inconsistent. For example, in period 6, the lowest value of FWHM is found for Au (group 11), while FWHM increases with the group from group 4 (Hf) to group 6 (W). Such sequence, i.e., group 11→4→5→6, is observed for all three periods, not only in FWHM but also in the low-energy peak position. The FWHM for the same elements does not change significantly when the energy of incident Ar ions is increased from 300 eV to 1200 eV.

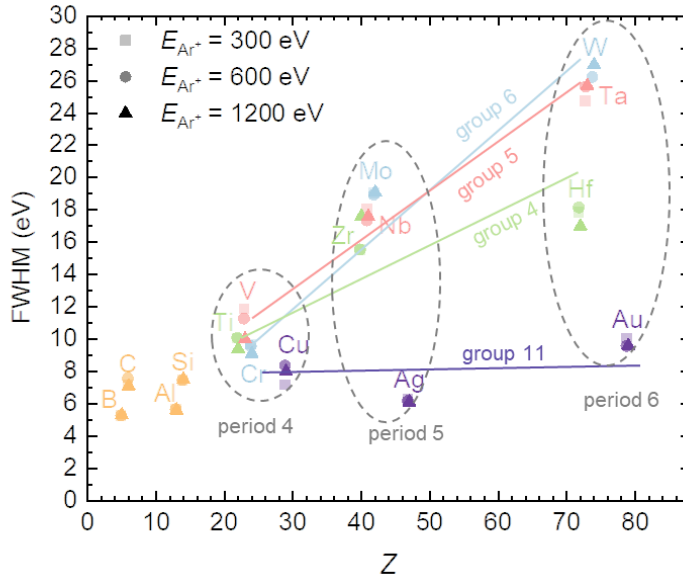


Figure 6.27: Full width at half maximum (FWHM) of EDFs in dependence on the atomic number. Elements in the same group are colored with the same color, and with different shades and symbols for different energies (300 eV, 600 eV and 1200 eV Ar ions).

The Thompson distribution in Figures 6.21–6.23 shows a faster decrease in energy tail than SRIM simulations for all of the simulated transition elements. On the other hand, the Sigmund energy distribution decreases similarly to the SRIM simulations, but it does not decrease to zero at maximum transfer energy as in Thompson distribution and in simulated EDFs. The EDFs simulated for light elements (B, C, Al and Si) show significantly different shapes than other elements: a high peak at low energies is followed by a fast decrease in the energy tail (Figures 6.21–6.23). Sigmund and Thompson energy distribution functions for light elements show a different shape. There is a much slower decrease in the energy tail and overall more atoms are sputtered at higher energies.

The Sigmund-Thompson distribution predicts that the tail of the distribution decreases as $1/E^2$. In order to verify this dependence, we fitted the Sigmund equation $A_S E_{\text{msb}} E / (E_{\text{msb}} + E)^n$ to the simulated tail of total EDFs where the exponent n was a free parameter. The best-fit values of n for sputtering with Ar ions of 300 eV, 600 eV and 1200 eV energy are collected in Table 6.7. The coefficient of determination was in all cases higher than 0.994. Results show that the fitting parameter n is almost independent of the ion energy. For all investigated target materials with $Z > 14$, exponent n is close to 3, which is in agreement with the Sigmund and Thompson analytical equations.

The experimentally obtained EDFs reported in the literature do not always fit to $n = 3$. For example, Dembowski *et al.* [118] measured EDFs for Cu, V and Nb sputtered by Ar ions at 600 eV, 1000 eV and 2000 eV. For normal Ar ion incidence with 600 eV they found that values of $n = 3.3$ best fitted the measurements for Cu and V and $n = 2.7$ for Nb. At higher energies (2 keV) the authors found a closer match to $n = 2$ for all three analyzed elements. For ion energies below 2.0 keV and for other angle combinations, the measurements deviated significantly from $n = 2$ dependence. Authors suggested that deviations from theoretical predictions could originate from the incomplete development of the sputtering cascades.

Table 6.7: The fitting parameter n for the equation $A_S E_{\text{msb}} E / (E_{\text{msb}} + E)^n$ at Ar ion energies of 300 eV, 600 eV and 1200 eV.

	Z	A	E_{msb}	n $E_i=300$ eV	n $E_i=600$ eV	n $E_i=1200$ eV
Si	14	0.970	3.8	3.63	3.48	3.35
Ti	22	0.992	5.2	3.21	3.21	3.15
V	23	0.985	5.5	3.26	3.27	3.25
Cr	24	0.983	4.9	3.33	3.34	3.32
Cu	29	0.948	4.3	3.24	3.27	3.27
Zr	40	0.847	8.3	3.02	3.04	3.02
Nb	41	0.841	9.0	3.08	3.14	3.14
Mo	42	0.830	10.0	3.13	3.20	3.20
Ag	47	0.789	3.2	3.07	3.12	3.04
Hf	72	0.598	9.5	3.07	3.12	3.10
Ta	73	0.593	13.5	3.12	3.23	3.23
W	74	0.587	14.0	3.15	3.25	3.27
Au	79	0.561	5.5	3.03	3.09	3.09

The maximum energy of sputtered atoms is another characteristic of EDFs that is also influenced by the atomic number. The cut-off of the EDFs changes significantly within individual groups but very little within the period (see Figures 6.21–6.23). Sputtered atoms in period 4 reach the highest maximum energies. The maximum energy for the elements decreases with increasing period number. For sputtering with 300 eV Ar ions, the maximum energies of sputtered atoms are approximately 280 eV in period 4, 240 eV in period 5 and 160 eV in period 6 (Figure 6.21). The maximum energy of sputtered atoms depends on the energy of ions as is visible in Figures 6.21–6.23.

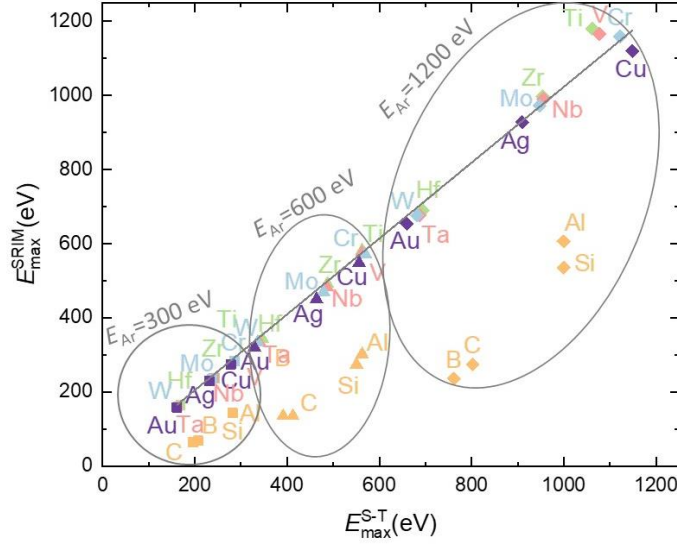


Figure 6.28: The maximum energy of sputtered particles for sputtering with 300 eV, 600 eV and 1200 eV calculated with SRIM and predicted by the Thompson model.

The maximum energy of sputtered atoms is obtained from the Thompson sputtering theory as $E_{\max} = \Lambda E_i$. The values of energy transfer factor (Λ) can be found in Table 6.1. Figure 6.28 shows the maximum energy calculated from $E_{\max} = \Lambda E_i$ and the one obtained from SRIM simulations. The agreement between the simulated and theoretical values is good for the transition metals at all ion energies (the slope of the fitted curve is close to 1). On the other hand, for light elements (B, C, Al, Si), the maximum energies of sputtered atoms obtained from SRIM simulations are almost a factor of two lower than the maximum energies calculated from $E_{\max} = \Lambda E_i$. This again demonstrates that SRIM simulations for light elements are not reliable as discussed earlier.

6.3.2 Angular energy distribution functions

The experimental techniques measure the atom energies only in a specific angular range, therefore, they provide data on the angular EDFs and not on the total EDFs. For comparison between experiments and simulations the angular EDF is more relevant than total EDF.

The angular EDFs obtained from SRIM simulations are shown in Figures 6.21–6.23 in colored lines, while the total EDFs are shown in black lines. In general, the shape of angular EDFs is similar to the total EDFs, however, with several noticeable differences. The number of atoms at the peak position of the angular EDFs decreases with the polar emission angle. Most atoms are sputtered close to the normal direction which was also observed in our analysis of differential sputtering yields (see Figure 6.14). The high-energy tail decreases similarly for all emission angles, which is demonstrated in the normalized angular EDFs for Ti and Ag in Figure 6.29.

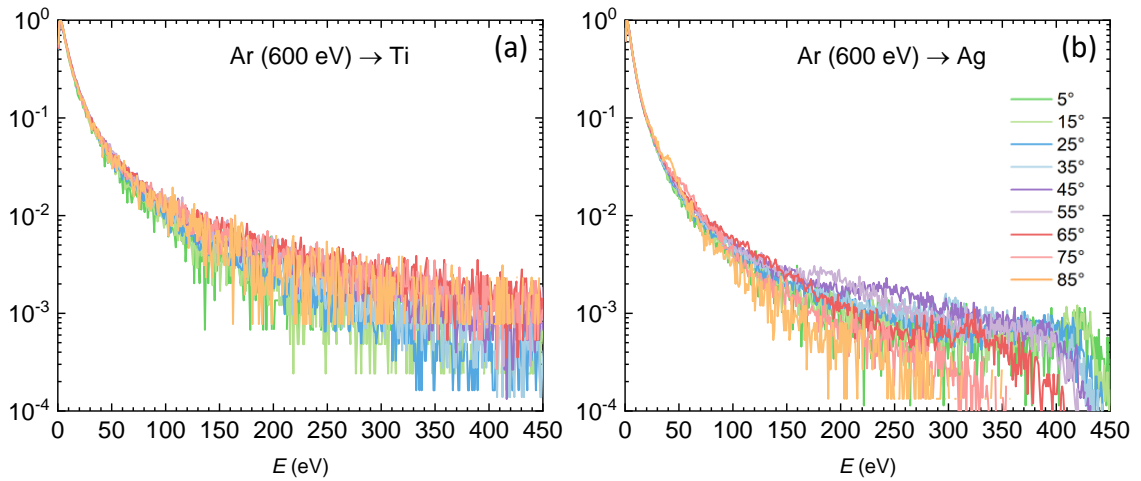


Figure 6.29: Normalized angular EDFs obtained from SRIM simulations for Ti (a) and Ag (b) sputtered with 600 eV Ar ions. The tail of the distribution has a similar shape at different emission angles.

The Sigmund and Thompson sputtering theories provide an equation for the total EDF of sputtered atoms. The authors suggested adding a cosine factor to the total EDF to obtain the angular EDF; this is based on the assumption that the angular distribution of recoils is isotropic [51]. To analyze the viability of such approach we used the Sigmund distribution with the cosine factor (i.e. $A_s E_{sb} E / (E + E_{sb})^3 \cos \theta$) to fit the simulated angular EDFs. In Figure 6.30, we demonstrate such fits for sputtering Ti with 600 eV Ar ions (the Sigmund angular EDFs are presented by smooth lines with a color corresponding to the simulated angular EDFs). The Sigmund function was first fitted to the total EDF and then multiplied by cosine for investigated polar angles. For all polar angles the Sigmund EDFs with the cosine factor are one or two orders of magnitude higher than the simulated angular EDFs. It can be assumed that either the Sigmund cosine distribution overestimates the simulated angular EDFs or the simulated distributions underestimate the angular EDFs.

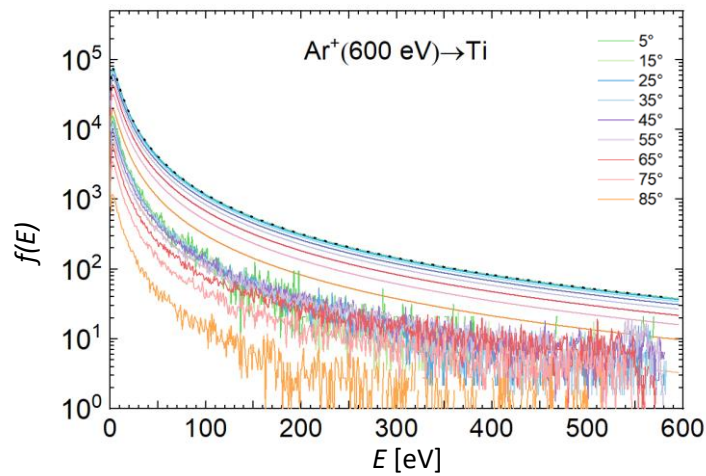


Figure 6.30: Angular and total EDFs for Ti bombarded by 600 eV Ar ions.

The experimental results in the literature suggest that the Sigmund distribution overestimates the measured angular EDFs. For example, Lautenschläger *et al.* [117] measured angular EDFs of Ti sputtered by Ar ion with 1 keV normal to the surface. They observed a faster decrease in the energy tail than was obtained from the Sigmund equation with a cosine factor. The authors performed SDTrimSP simulations and obtained a reasonable fit with the experimental data. Similarly, Bundesmann *et al.* [119] measured angular EDFs for sputtering Ag with Ar ions of 1 keV. They also compared the measured angular EDFs to simulations performed by TRIM.SP program. In general, they found a decent agreement between experimental and simulated EDFs. However, the authors noted some differences. For instance, the distributions appeared narrower due to direct sputtering and more pronounced in the simulated curves than in the measured EDFs. They attributed this to non-realistic assumptions of TRIM.SP program, such as an amorphous target with randomly distributed particles, an idealized flat surface and mono-energetic primary particles. Interestingly, they did not observe much variation in the EDFs at different polar angles when the material was bombarded by Ar ions normal to the surface. In our simulation of angular EDFs we also see less variation in EDFs with regard to the polar angle when sputtering Ag and other transition metals with Ar ions of higher energies (e.g., 1.2 keV). More variation is observed when the material is sputtered at lower ion energies (see Figure 6.21).

In an earlier work, Eckstein [120] used TRIM.SP to investigate simulated total and angular EDFs of sputtered atoms. The simulations showed that the shape of the EDFs depends on the emission angle. At low emission angles, the EDFs showed a deficiency in sputtered atoms both at low energies and at high energies but not in the middle energy range, and more intensity above the maximum of the distribution (see Fig 3 in Ref. [120]). At large emission angles the distributions showed a strong deficiency at high energies, and a surplus at low energies. This was explained by the change in angle that occurs when the particle passes through the surface due to surface binding energy. At medium emission angles, there was mainly a surplus at high energies.

Angular EDFs were also investigated by a semi-empirical model developed by Stepanova and Dew [121]. The authors took into account anisotropies by introducing the correction factor for sputtering in the sub-keV region. They also observed that the EDF was narrower around the low energy peak when the energy of incident ions decreased. Our SRIM simulations did not show such narrowing.

Brizzolara *et al.* [122] measured EDFs for Cu sputtered by Ar ions with energies in the 40–1000 eV range. The angle of incidence of the Ar ion beam and emission of the sputtered particles were normal to the target surface. Measurements showed that the EDFs were comparable in shape for different sputtering energies. The Sigmund-Thompson distribution fitted well to the experimental EDFs when the energy of impinging ions was above 600 eV. When the energy of incident ions was lower than 600 eV, the distributions decreased faster and the peak shifted to the lower energy values.

In another work, Goehlich *et al.* [123] observed that for normal Ar impingement, EDFs at higher emission angles broaden and the low-energy peak shifts toward higher energies. Such behavior was significant for Ti whereas for W only weak changes in the EDFs with the emission angle were found. The broadening of EDF and shift of the low-energy peak toward higher energies with increasing emission angle were not observed in our SRIM simulations. Namely, we observe that the peak position for all transition metals remains practically unchanged for different emission angles.

A distinct feature in angular EDFs is the presence of high-energy peaks that typically exhibit a hump-like shape (see Figure 6.21 and Figure 6.22). In Figure 6.21, which shows EDFs for sputtering with 300 eV Ar ions, a broad high-energy peak can be seen for elements in period 6 for emission angles higher than 45°. These peaks can be observed also for elements in period 5 where they are wider but less pronounced than in period 6. The high-

energy peaks for Nb and Ta in period 5 are present in the 40–60 eV range. In the EDFs of elements in periods 5 and 6, there is also a second high-energy peak near the end of the energy tail. This second high-energy peak is very wide and extends between 100 eV and 200 eV depending on the emission angle and sputtered material. At the emission angle of 45° , it is wider than at higher angles. In some elements, the first and the second high-energy peak at 45° appear to overlap (see e.g. Zr, Nb, Mo and Hf). In period 6, the second high-energy peaks are more pronounced (higher and narrower) compared to the ones in period 5. For the highest emission angle (85°) in the period 6, the first high-energy peak appears at approximately 40 eV and the second peak at approximately 90 eV. The position and the shape of the high-energy peaks do not change significantly within the elements of the individual period (cf. peaks in period 6). On the other hand, high-energy peaks of elements within individual groups have different widths. The heavier elements have sharper high-energy peaks than the lighter elements (compare e.g. peaks for W and Mo), while the lightest transition metal elements do not exhibit any high-energy peaks (see EDFs for Ti, V and Cr).

The high-energy peaks are also noticeable for some elements when bombarded by Ar ions with 600 eV (see Figure 6.22). In period 6, the second high-energy peaks are still noticeable, while they are much less pronounced in period 5. When increasing the ion energy to 1200 eV (Figure 6.23), the high-energy peaks are visible only for elements in period 6, while for all other elements, they are not present.

Broad high-energy peaks have also been observed experimentally when sputtering Si [124, 125], Ag [113, 125], Ge [126] and Ti [117, 123] by Ar and Xe ions. In these works, the authors measured angular EDFs for different incident angles of bombarding ions and for different emission angles of sputtered atoms. They observed a high-energy hump-like peak when the sum of the incident and emission angle was higher than 90° – the higher the difference, the more pronounced the peak [123]. Authors attributed the presence of high-energy peaks to the directly recoiled atoms. Namely, the directly sputtered atoms have higher energies than atoms that are sputtered after the collision cascade is fully developed. The SDTrimSP simulations performed in these works qualitatively recreated the presence of high-energy peaks although the hump in the simulation appeared more pronounced in comparison to the measurements. Some differences between the experimental and simulation results were attributed to the underestimated energy losses in the simulation program.

Goehlich *et al.* [123] observed experimentally the high-energy peak at approximately 45 eV for the emission angle of 60° when sputtering Ti with 225 eV Ar ions at normal incidence. However, when sputtering W at similar conditions, the high-energy peak was not observed. Our SRIM simulations show the opposite: when sputtering with 300 eV Ar ions, the high-energy peaks are not observed in Ti but in W, the first high-energy peak is present for emission angles higher than 55° . The high-energy peak in our SRIM simulations was positioned at approximately 100 eV for the 45° emission angle and at 40 eV for the 85° emission angle.

The maximum energy of sputtered atoms in angular EDFs depends significantly on the period but very little on the group as was also observed in total EDFs. The maximum energy of sputtered atoms is the lowest for elements in period 6 and the highest for elements in period 4. For example, in period 4, the maximum energies of sputtered atoms near the surface normal are up to 580 eV and decrease to around 500 eV at high emission angles for sputtering with 600 eV ions. On the other hand, for elements in period 6, the atoms sputtered near the surface normal have a maximum energy of 350 eV and the atoms sputtered at the highest emission angle have a maximum energy of 200 eV. In general, elements within individual periods have similar angular EDFs in terms of shape, high-energy peaks and maximum energy of sputtered atoms, while there are considerable differences when comparing angular EDFs of elements within individual groups.

6.4 Average Energy of Sputtered Particles

The average energy can be evaluated for atoms sputtered in the entire space above the surface (i.e. hemisphere) or in particular angular intervals. The average energies of atoms sputtered in specific angular directions are relevant for experimental reasons. Namely, the diagnostic tool (such as an energy-resolved mass spectrometer) is usually positioned in a specific direction and therefore measures angular EDFs and corresponding angular average energy. In the case of isotropic sputtering, such measurements can provide polar average energy of sputtered atoms. We first analyze the average energies of atoms sputtered into the whole hemisphere and then analyze average energies for specific polar intervals.

6.4.1 Total average energy of sputtered atoms

The total average energy of sputtered atoms is the average energy of all atoms sputtered in the area above the surface. It can be calculated from the Sigmund-Thompson distribution by inserting Eq. (2.23) into Eq. (4.17). The integration is performed up to the maximum atom energy (i.e., $E_{\max} = \Lambda E_i$). Detailed evaluation of the integrals can be found in the appendix of Ref. [127]. With several reasonable simplifications, the following equation is obtained for the average energy of sputtered atoms:

$$\bar{E}_{\text{S-T}} = 2E_{\text{msb}} \ln(\Lambda E_i / E_{\text{msb}}) - 3E_{\text{msb}}. \quad (6.6)$$

Here, E_i is the energy of the incident ion, E_{msb} is the modified surface binding energy and Λ is the energy transfer factor. Note that the average energy of sputtered atoms only depends on the (modified) surface binding energy and maximum energy of sputtered atoms. Eq. (6.6) is useful for comparing the theoretical average energies to the ones obtained from SRIM simulations.

The total average energy of sputtered atoms was obtained by simulating normal Ar ion impingement for 100–1200 eV range in 100 eV steps, from the SRIM interface. The ion energy dependence of the total average energy of sputtered atoms was fitted to the following logarithmic equation [59]:

$$\bar{E} = aE_{\text{msb}} \ln\left(\frac{\Lambda E_i}{E_{\text{msb}}}\right) - bE_{\text{msb}}, \quad (6.7)$$

where a and b are the fitting parameters, E_{msb} is the modified surface binding energy, E_i is the ion energy and Λ is the energy transfer factor. The above equation was chosen as a fitting relation because it is obtained from the Sigmund distribution when evaluating the average energy of sputtered atoms (see appendix of [127]). We introduce two fitting parameters a and b to fit the average energies of sputtered atoms simulated by SRIM. The fitting parameters for the investigated materials are presented in Table 6.8. The coefficient of determination R^2 was in all cases better than 0.97.

Figure 6.31 presents simulations of the average energies of sputtered particles and fitted curves with parameters from Table 6.8. The average energies follow the logarithmic function in dependence on the ion energy. For transition metals, the average energies of sputtered particles in groups 4–6 are significantly higher than in group 11. Among the elements from groups 4–6, the elements from period 5 (i.e., Zr, Nb, Mo) exhibit the highest average energies. The elements in period 6 (i.e., Hf, Ta, W) demonstrate slightly lower average energies, whereas elements in period 4 (i.e., Ti, V, Cr) display the lowest average energies among the elements within groups 4–6. Among the transition metals, elements in

group 11 (i.e., Cu, Ag, Au) exhibit the lowest average energies. The lightest elements (groups 13 and 14) have significantly lower average energies than the transition metals according to SRIM simulations.

Table 6.8: Parameters a and b were obtained when fitting the total average energy to Eq. (6.7). Other relevant parameters are also shown: atomic number Z , the energy transfer factor A and modified surface binding energy E_{msb} .

Elem.	Z	A	E_{msb}	a	b
B	5	0.670	2.8	0.82	1.90
C	6	0.711	3.6	0.77	1.62
Al	13	0.962	2.8	1.09	2.54
Si	14	0.970	3.8	0.87	1.76
Ti	22	0.992	5.2	2.18	3.88
V	23	0.985	5.5	1.93	2.97
Cr	24	0.983	4.9	1.41	1.47
Cu	29	0.948	4.3	1.15	0.37
Zr	40	0.847	8.3	2.40	3.34
Nb	41	0.841	9.0	1.87	1.92
Mo	42	0.830	10.0	1.75	1.85
Ag	47	0.789	3.2	1.59	1.24
Hf	72	0.598	9.5	1.66	1.56
Ta	73	0.593	13.5	1.36	0.92
W	74	0.587	14.0	1.26	0.74
Au	79	0.561	5.5	1.14	0.25

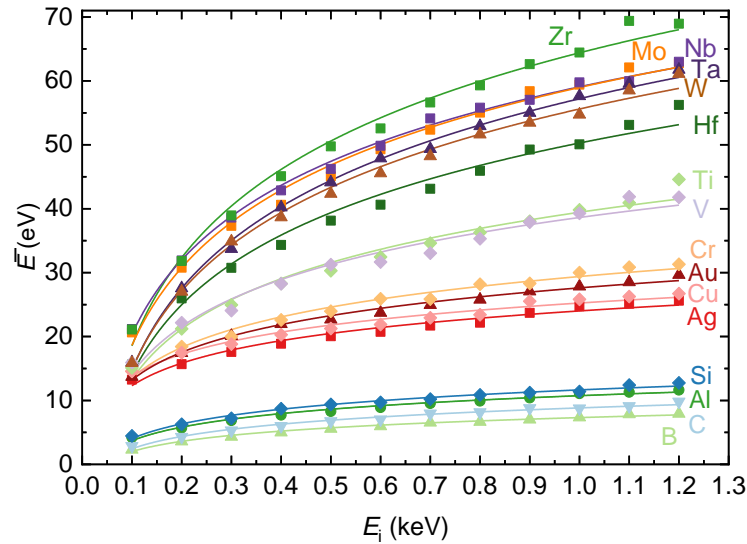


Figure 6.31: The total average energy of sputtered atoms as a function of Ar ion energy obtained from SRIM simulations and fitted to Eq. (6.7).

Figure 6.32 shows a comparison between the average energies from SRIM simulations and the average energies calculated from Eq. (6.6). In general, the average energies obtained by SRIM are higher than the analytically calculated average energies. The linear function that best fits the data is $y \approx 1.3x$. Hence, the average energies obtained from SRIM simulations are approximately 30 % higher than the theoretically predicted ones. The largest difference is observed for Zr and Nb. The accuracy of theoretical and simulated total average energies could be verified by comparing the data with the measurements from the literature. However, experimentally measured average energies are measured only in specific spatial directions and should therefore be compared to the angular average energies. This is discussed in Section 6.4.2.

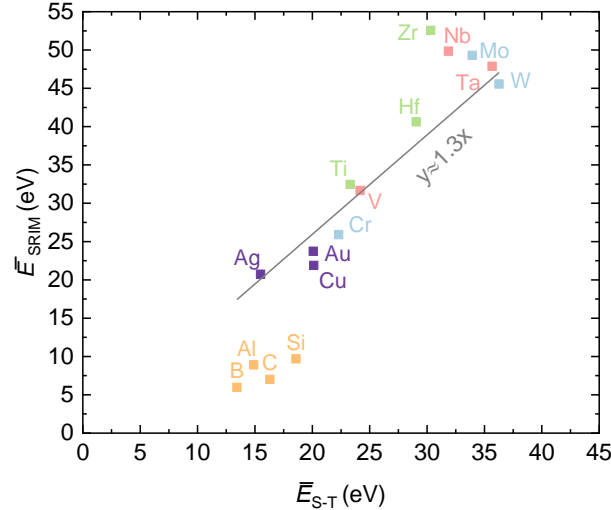


Figure 6.32: Comparison of the average energies obtained from SRIM simulations and the ones calculated with Eq. (6.6) for Ar ions with 600 eV energy.

The SRIM simulations performed in this work show that elements in group 11 (Cu, Ag, Au) have the lowest total average energies. Higher total average energies are observed for the transition metals in groups 4, 5 and 6 (see Figure 6.32) among which the lowest average energies have the lightest three transition metal elements in period 4, i.e. Ti, V and Cr. In Figures 6.21–6.23, the EDFs of Cu, Ag, and Au exhibit stronger (i.e., more intense) low-energy peaks and weaker high-energy tails. The opposite is the case for the elements in groups 4 and 5 (Ti, Zr, Hf; V, Nb, Ta). These elements have smaller low-energy peaks and longer high-energy tails, which results in higher average energies. The peak of total EDFs for those same elements is positioned at higher energies (see Table 6.6) which also results in higher average energies. The total average energy increases logarithmically with the ion energy as shown by the SRIM simulations (Figure 6.31) and the Sigmund-Thompson theory for the average energy of sputtered atoms (see Eq. (6.6)).

If the total average energy of sputtered atoms is plotted in dependence on the total sputtering yield, then an inverse correlation can be observed for the transition metals (Figure 6.33). To our knowledge, there is no theoretical expression in the literature that would correlate the average energy of sputtered atoms to the sputtering yield, therefore we provide an empirical equation that best fits our data. The average energies in dependence on sputtering yield show similar trends for sputtering with ions in the 300–1200 eV range. For the transition metals, the relation between the total average energy of sputtered atoms and the sputtering yield can be fitted to a simple function:

$$\bar{E} \approx 0.06 \frac{E_i}{Y^{0.5}}, \quad (6.8)$$

The numerical factors in the equation (i.e., the leading constant and the power coefficient) were obtained by fitting data to results obtained for all three ion energies, i.e., 300 eV, 600 eV and 1200 eV. For clarity, we present in Figure 6.33 only results for sputtering with 600 eV Ar ions. Note that in Eq. (6.8), the total average energy of sputtered atoms is linearly dependent on the ion energy and is approximately inversely proportional to the square root of the sputtering yield.

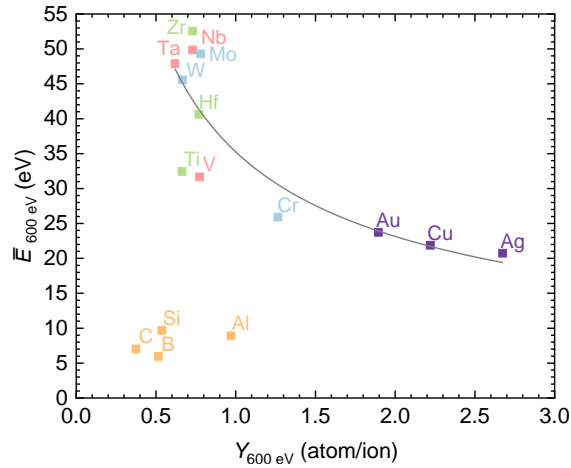


Figure 6.33: Total average energy in dependence on sputtering yield for 600 eV Ar ions.

We emphasize that Eq. (6.8) should be used only as a rough approximation for the expected average energies of sputtered transition metals. In Table 6.9, we provide the average energies of sputtered atoms for sputtering with 300 eV, 600 eV, and 1000 eV Ar ions. The table provides data for all transition metal elements from groups 4–12 of the periodic table. For the evaluation, we used sputtering yields from Table 6.4 calculated with Eq. (6.3).

Graphical presentation can be found in Figure 6.34 where average energy and sputtering yields for transition metals are presented with respect to atomic number Z . Elements of the same group are plotted in the same color for periods 4, 5 and 6.

A possible qualitative explanation for the inverse proportionality could be that in elements with higher sputtering yield the energy of the incident ions is redistributed among a larger number of atoms in the solid; as a result, the average energy of recoiled and sputtered atoms is lower. On the other hand, in the case of low sputtering yield, the energy of the incident ions is transferred to a smaller number of atoms, and consequently, the average energy of the sputtered atoms is higher. Based on similar reasoning, it can be expected that Eq. (6.8) should better describe the relationship when fully developed collision cascades are formed (i.e., at higher ion energies).

Table 6.9: Average energies of sputtered atoms calculated with Eq. (6.8). The theoretical sputtering yields are taken from Table 6.4.

Element	$Y_{300 \text{ eV}}$	$\bar{E}_{300 \text{ eV}}$	$Y_{600 \text{ eV}}$	$\bar{E}_{600 \text{ eV}}$	$Y_{1000 \text{ eV}}$	$\bar{E}_{1000 \text{ eV}}$
Ti	0.39	28.82	0.63	45.36	0.89	63.60
V	0.44	27.14	0.72	42.43	1.04	58.83
Cr	0.61	23.05	1.05	35.13	1.55	48.19
Mn	0.90	18.97	1.53	29.10	2.26	39.91
Fe	0.77	20.51	1.34	31.10	2.01	42.32
Co	0.86	19.41	1.52	29.20	2.32	39.39
Ni	0.94	18.57	1.70	27.61	2.60	37.21
Cu	1.09	17.24	1.98	25.58	3.08	34.19
Zn	3.44	9.70	6.40	14.23	10.11	18.87
Zr	0.41	28.11	0.66	44.31	0.95	61.56
Nb	0.41	28.11	0.69	43.34	1.00	60.00
Mo	0.43	27.45	0.73	42.13	1.07	58.00
Tc	1.48	14.80	2.51	22.72	3.70	31.19
Ru	0.63	22.68	1.07	34.80	1.60	47.43
Rh	0.75	20.78	1.29	31.70	1.93	43.19
Pd	1.10	17.16	1.92	25.98	2.90	35.23
Ag	1.36	15.43	2.39	23.29	3.63	31.49
Cd	3.38	9.79	6.04	14.65	9.25	19.73
Hf	0.44	27.14	0.73	42.13	1.06	58.28
Ta	0.36	30.00	0.61	46.09	0.88	63.96
W	0.40	28.46	0.69	43.34	1.02	59.41
Re	0.60	23.24	1.03	35.47	1.52	48.67
Os	0.64	22.50	1.09	34.48	1.63	47.00
Ir	0.76	20.65	1.32	31.33	1.98	42.64
Pt	0.91	18.87	1.60	28.46	2.42	38.57
Au	1.00	18.00	1.77	27.06	2.69	36.58

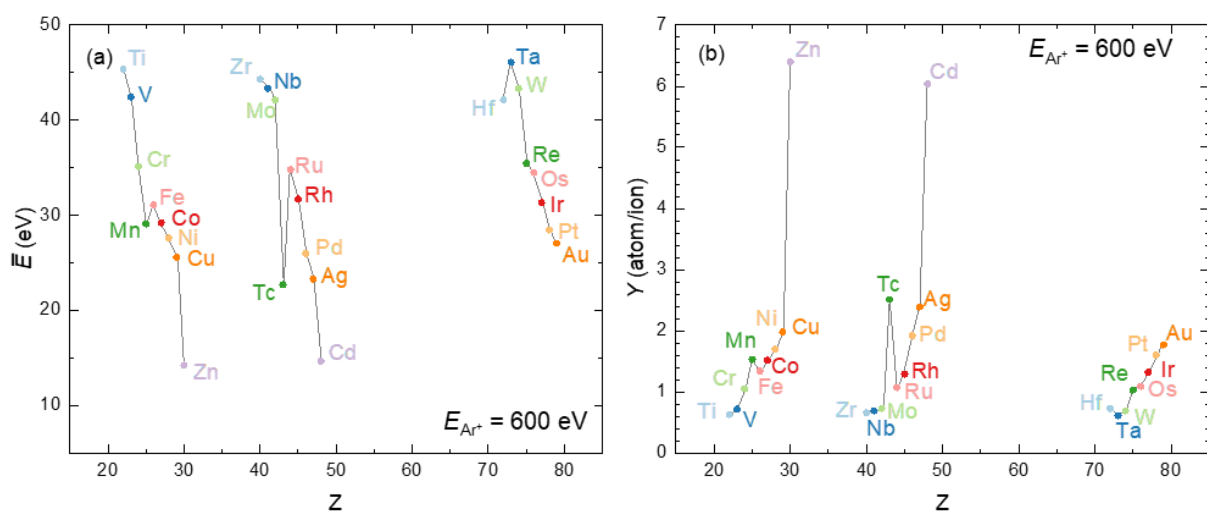


Figure 6.34: The average energy (a) and sputtering yield (b) of transition metals, calculated with Eq. (6.3) and Eq. (6.8).

6.4.2 Angular average energies of sputtered atoms

Figure 6.35 presents the polar distribution of average energies for the investigated elements. The shapes of the distribution are similar regardless of the ion energy. The elements in period 4 and groups 4–6 (i.e., Ti, V, Cr) exhibit the most directed distribution with the highest average energies near the 65° emission angle. The elements in period 5 and groups 4–6 (i.e., Zr, Nb, Mo) have a somewhat less directed distribution with the highest average energies around the 50° angle. For the elements in groups 4–6 in period 6 (i.e., Hf, Ta, W) the distribution of the average energy is more isotropic than in periods 4 and 5. The highest average atom energies are found near the 45° emission angle. The shape of the polar distribution for elements in groups 11 (i.e., Cu, Ag, Au) also changes with the period – a more anisotropic distribution is visible for Cu (period 4) and most isotropic distribution (close to circular) for Au (period 6). In general, the elements in group 11 have a more isotropic distribution compared to elements in groups 4–6. Furthermore, the heaviest elements show the most isotropic distributions for the angular average energies.

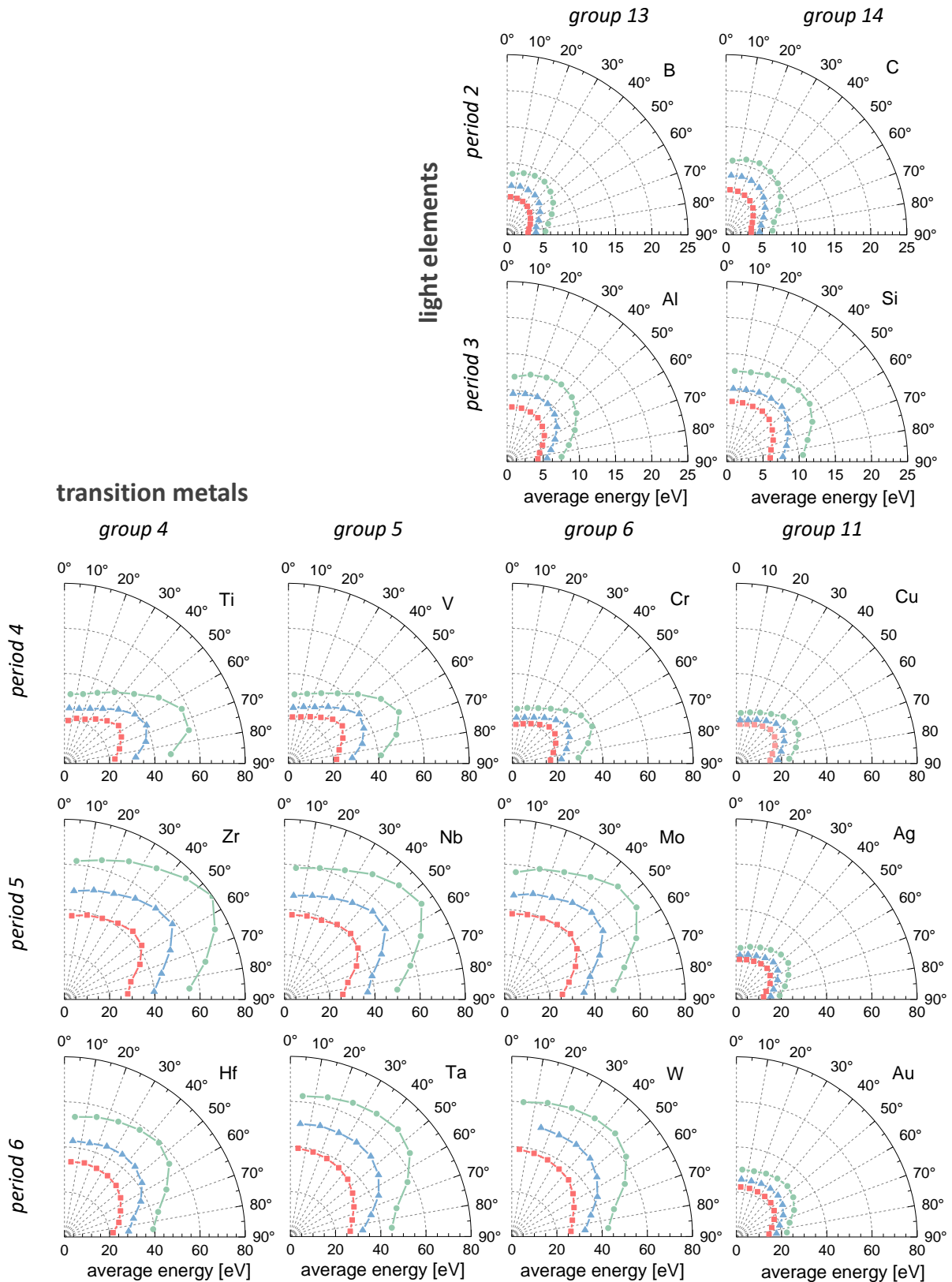


Figure 6.35: Angular distribution of average energies for selected elements with 300 eV (red), 600 eV (blue), and 1200 eV (green) energy Ar ions at perpendicular sputtering directions. The graphs show the average energy of atoms, sputtered in a particular polar angle interval.

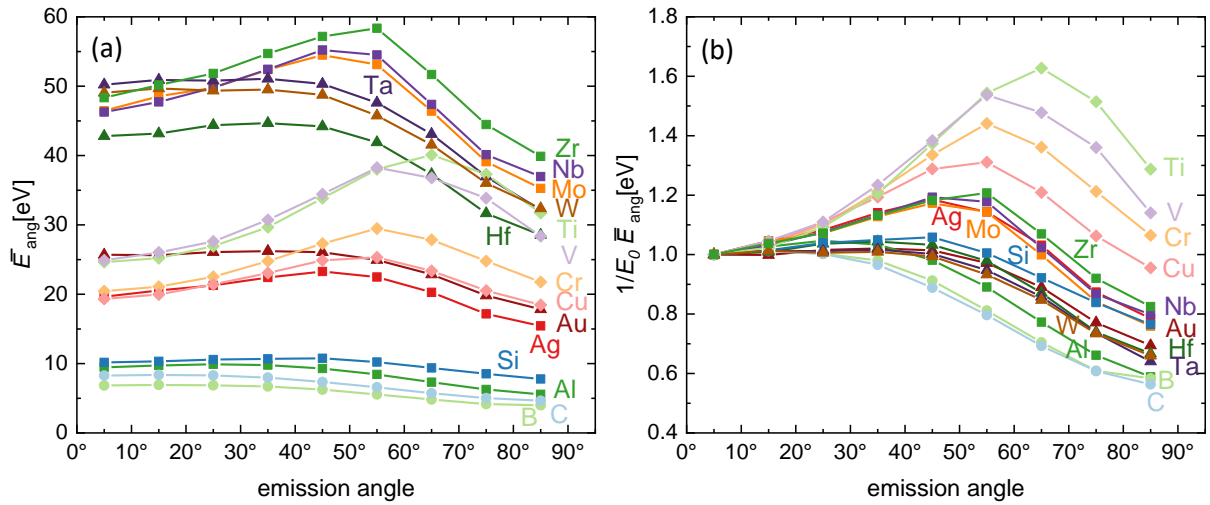


Figure 6.36: Average energies of sputtered atoms in dependence on emission angle obtained from SRIM simulations for Ar ions with 600 eV: (a) absolute distributions of average energies and (b) normalized distributions.

In order to more easily compare the polar distributions of average atom energies, we present the data also in the cartesian coordinate system shown in Figure 6.36. The angular average energies for investigated target materials bombarded by 600 eV Ar ions are shown in Figure 6.36a, while in Figure 6.36b, the same angular average energies are normalized by the value of average energy in the normal direction.

The average energy of sputtered atoms depends on the emission angle as demonstrated in Figure 6.35 and Figure 6.36a. For transition metals, the average energies increase with the emission angle and reach the highest values at approximately 50–70°, followed by a gradual decrease. In period 4 (Ti, V, Cr, Cu), the average atom energies show the largest variation with the emission angle (see Figure 6.36b). In period 5, the differences between average energies into different emission angle ranges are lower than in period 4. In period 6 (Hf, Ta, W and Au), the differences between angular average energies are the lowest. For the light elements (B, C and Al) the SRIM simulations show that the average energies of sputtered atoms are approximately the same for all analyzed angles and are the highest for emission angles in the 0°–30° range.

In individual groups, the element with the lowest atomic number exhibits the highest differences between angular average energies for different emission angles. For example, in group 4 (Ti, Zr and Hf), the differences between average energies into specific emission angles are higher for Ti than for Zr and are the lowest for the heaviest element Hf. The same trend is observed in other groups too. The differences between angular average energies for different emission angles become lower with increasing atomic number.

The angular average energies obtained from SRIM simulations can be compared to the measured average energies from the literature. Lautenschläger *et al.* [117] measured angular EDFs for Ti bombarded by Ar ions with 1 keV at normal incidence using the ion beam sputtering, which is also discussed in [128]. The authors measured an average energy of 26 eV at 60° emission angle, 32 eV at 70°, and 56 eV at 80°. These energies somewhat deviate from the energies from SRIM simulations obtained in this work. For Ar ion bombardment of Ti with the energy of 1.2 keV, the SRIM simulations give 40 eV at 65°, 37 eV at 75° and 32 eV at 85°.

Feder *et al.* also measured and simulated the sputtering of Ag target with Ar ions [113]. The average energies calculated from measured EDFs for sputtering with 0.5 keV and 1 keV Ar ions were somewhat lower than the ones calculated in this work. For sputtering with 1 keV, the authors measured the average energy to be approximately 18 eV for emission angles higher than 60° . For sputtering with 1.2 keV, the average energy evaluated from SRIM simulations is 25.5 eV for 65° emission angle, 22.4 eV for 75° and 19.4 eV for 85° emission angle. The authors also show that the average energy of sputtered Ag atoms does not change much with the increasing emission angle.

Angular EDFs of sputtering Cu, V and Nb targets with Ar ions were measured by Dembowski *et al.* [118]. Their experimentally determined average energies differ significantly from our simulation results. For sputtering Cu target with 600 eV normally impinging Ar ions, the authors measured 8.8 eV average energy of atoms sputtered in the normal direction, while our SRIM simulations give 19.3 eV. When sputtering V and Nb under the same emission angles, the authors measured 8.7 eV and 12.7 eV, respectively, while our simulations show significantly higher average energies, 25.0 eV and 46.3 eV. The authors simulated average energies using ACAT simulation code and also obtained somewhat higher average energies as compared to the measured ones (see Fig. 7 in Ref. [118]).

Brizzolara *et al.* [122] analyzed the average energies of sputtered atoms from the measured EDFs for Cu sputtered by Ar ions impinging normal to the surface in the 40–1000 eV range. The authors observed that the average kinetic energy of the sputtered Cu atoms increased with the ion energy and that the rate of this increase was lower at higher ion energies (see Fig. 7 in Ref [122]). The average energies of normally sputtered atoms ranged from approximately 5 eV for sputtering with 200 eV Ar ions to 8 eV for sputtering at 1000 eV. The dependence of average atom energy on the ion energy only qualitatively agrees with our SRIM simulations, since we get about 3-times higher total average energies (16 eV at 200 eV and around 25 eV at 1000 eV).

Semi-empirical models have also been used to calculate the average energies of sputtered atoms in dependence on the emission angle. For example, Stepanova [121] evaluated the angular dependence for Cu and W. The angular distribution at high angles differs significantly from the SRIM simulations at high angles (cf. Fig. 13 in [121] and Figure 6.36a in this work). For Cu sputtering with 1000 eV Ar ions, the energies calculated with the Stepanova model range from approximately 8 eV in the normal direction with increasing values up to 17 eV for atoms sputtered close to the plane of the target (see Figure 15 in Ref. [60]). The SRIM simulations for sputtering with 600 eV Ar ions give the average energy of 19.3 eV in the normal direction. With the increasing emission angle, the average energy is increased to the maximum of 25.3 eV at 55° emission angle. The average energy is then decreased at higher angles down to 18.5 eV at the 85° emission angle. SRIM simulations show that the atoms with the highest energies are in the 60° – 70° range, while the Stepanova model predicts that the most energetic atoms are sputtered close to the surface plane.

6.5 Measurements of the Sputtering Yield

The main purpose of the thesis was to compare the analytical model and Monte Carlo simulations. However, we also decided to compare the results of the optimized sputtering yield simulations with measurements of the sputtering yield performed in our deposition systems. Here, we present the measurements of the target mass-change performed in the triode sputtering system and the layer thickness measurements of thin films that were deposited in the magnetron sputtering system.

6.5.1 Measurements of the total sputtering yield from the target mass change

The total sputtering yield measurements were performed in the triode sputtering system Sputron (Balzers, Liechtenstein). We sputtered Ti, V, Cr, and Cu targets with Ar ions. The ion energy was varied between 100 eV and 1000 eV in 100 eV steps. In this part of the experimental work, the sputtering yields were measured based on the measurement of the change in target mass before and after sputtering. Voltage and current as well as time of sputtering were recorded too.

The sputtering yields were determined as described in Section 5.2.1 and are presented in Figure 6.37 along with the sputtering yield simulations performed with SRIM. The results of the measurements are plotted with symbols while the SRIM simulations are shown with the line of the same color.

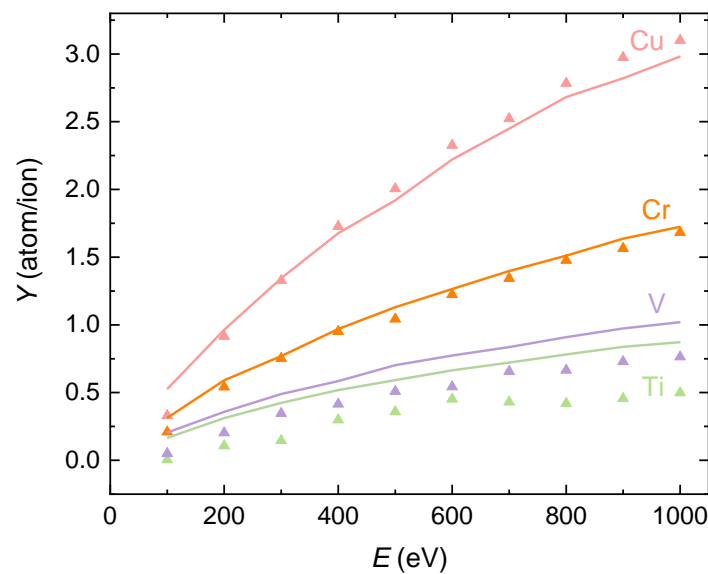


Figure 6.37: Sputtering yields of Ti, V, Cr and Cu in dependence on Ar ion energy. Experimental values are plotted with symbols and sputtering yields simulated by SRIM simulations with lines.

For all elements the deviations between the SRIM simulations and the experimentally measured sputtering yields are the largest at the Ar ion energy of 100 eV. The authors of the SRIM program were aware of the program limitations at very low ion energies [37]. This has also been noted by other authors [43].

The results of our experimental work show an agreement with the simulations for Cu and Cr at energies above 100 eV. The differences between the simulations and the measurements are less than 10 % in the investigated energy range. For V and Ti, the discrepancies are much larger. The measured sputtering yield for Ti is up to three times lower than the values obtained by simulations. The difference between the two values decreases with the energy of the Ar ions. At 1000 eV, the measured sputtering yield is for approximately 45% lower than the simulated value. For V, the experimental values are also lower than the SRIM results. At 200 eV Ar ion energy, the measured sputtering yield for V is 50% lower than the simulated values and at 1000 eV, the measured sputtering yield is 20% lower than the simulations predict.

The differences between the experimental data and the simulations can be attributed to the fact that we sputtered targets in a triode system, where the energy of the incident ions is not as precisely determined as in ion gun sources, but the incident ions have a certain energy distribution. During the sputtering process, we can also observe a slight fluctuation of the current at constant voltage – the fluctuations are not large, but rather they fluctuate around a certain average value, so we included the average value in the calculation. Nevertheless, this part can also contribute to the deviation from the experimental values. In addition, a breakdown can sometimes occur during the sputtering process, from which we can conclude that evaporation of atoms occurs at a certain point. Neither does SRIM take into account the fact that some Ar atoms may occupy a place in the target during sputtering. In addition to the sputtering of atoms, self-sputtering also occurs, which has a different sputtering yield than the atoms of the target.

6.5.2 Measurements of differential sputtering yield from thin film thickness

From the target mass-change, we can only measure the total sputtering yield. However, if we are interested in the angular distribution, which is important for the deposition of thin films, the total sputtering yield does not give enough information. For some applications, a high accuracy in film thickness is required and, above all, uniformity over the entire surface is also important. The angular sputtering yield can be determined from the thickness of thin films deposited at different angular positions of samples.

Angular sputtering yields were measured for the following materials: Al, Ti, V, Cr, Cu, Nb, Mo, Hf and Ta. The measured angular distribution is shown in Figure 6.38a. The substrates were placed in the chamber as shown in Figure 5.8 and sputtered with 0.4 A current. Layer thicknesses h were measured in 10° polar angle intervals and differential sputtering yields were calculated according to Eq. (5.16).

Copper exhibited the highest differential sputtering yield values, while all other elements exhibited 50–70 % lower differential sputtering yields. For all elements the differential sputtering yield was the highest at about $40\text{--}50^\circ$. With increasing emission angle, the differential sputtering yield decreases for all elements. The differential sputtering yield is the highest for lower sputtering angles due to the fact that the source of sputtered atoms is flat and not point-like.

The differential sputtering yield for Al, Ti, V, Nb, and Ta remained about the same while the angle decreased from 50° toward zero. On the other hand, the sputtering yield for Zr, Mo, Hf, Cr, and Cu slightly decreased for angles below 40° . The differences between angular distributions can easily be distinguished in Figure 6.38b where the measurements for each element are normalized to the maximum value. The angular distribution of normalized values of differential sputtering yields was very similar for all of the investigated materials.

According to the SRIM simulation of the differential sputtering yield (Figure 6.17), no decrease in the central region is expected. The layer thickness measurements give information about the deposition rate, while the collisions between the particles can be neglected due to the low gas pressure in the vacuum chamber. Thus, it follows that the deposition rate and the sputtering yield are linearly dependent (see Eq. (5.13)).

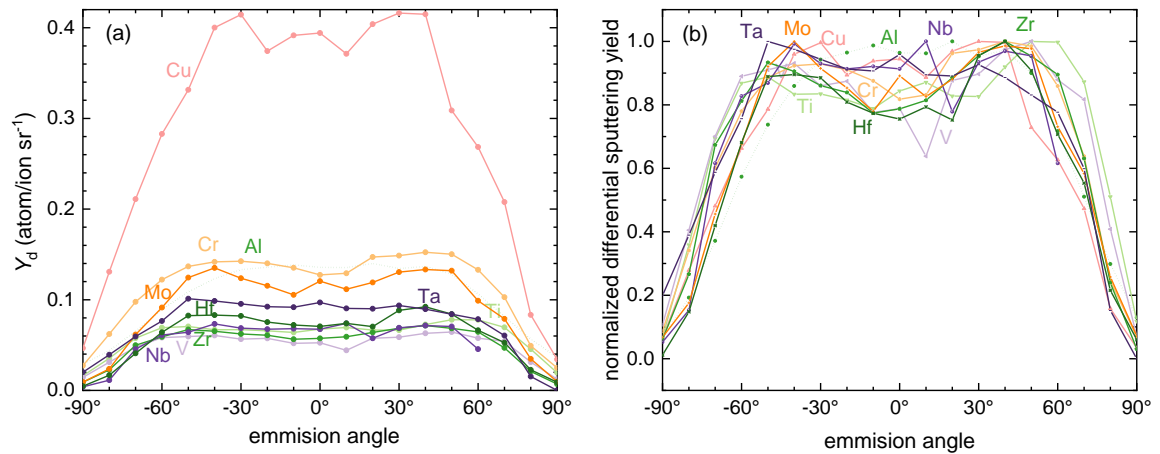


Figure 6.38: Differential sputtering yields for Al, Ti, V, Cr, Cu, Nb, Mo, Hf and Ta for different emission angles: (a) absolute values of differential sputtering yields and (b) sputtering yields normalized to the highest value.

In experimental measurements and deposition of thin films in diode, triode, or magnetron systems, one must be aware that the source is not point-like, but planar. For our experiments, we used a planar circular magnetron source where the racetrack is circular, as shown in Figure 6.39a. Thus, the atoms originate from a larger area that can be modeled by summing many point-like sources in a plane. The cross-section of this magnetron model is illustrated in Figure 6.39b.

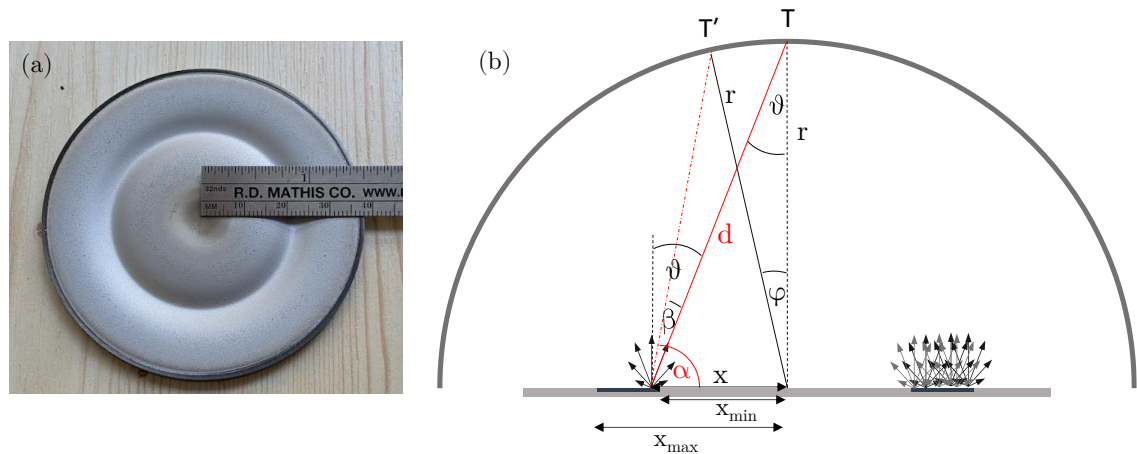


Figure 6.39: (a) Photo of a used magnetron source, from where we can determine the racetrack region. (b) Scheme of the magnetron cross-section. Circular symmetry enables us to sum the contributions of two linear sources of sputtered atoms.

To verify the experimental results from Figure 6.38, we integrated the contributions of many point sources, as shown in the magnetron cross-section in Figure 6.39b. In Chapter 6.2 (see Eq. (6.4) and Table 6.5) we presented that the sputtered atoms have a cosine distribution, therefore we calculated the contributions of many cosine point-like sources to a semicircular substrate with a radius of 100 mm. The center of the semicircular substrate coincides with the center of the magnetron surface, in the same way as in our experimental setup.

The deposition rate of all point-like sources between x_{\min} and x_{\max} to any point at distance d is equal:

$$R(d, \vartheta) = A \int_{x_{\min}}^{x_{\max}} \frac{1}{d^2} \cos(\vartheta - \beta) dx. \quad (6.9)$$

Here, A is a constant that depends on the sputtering yield and time of sputtering.

The deposition rate at any point T' on the semicircular substrate decreases with the square of the distance between T' and any point-like source at the distance x from the center of the magnetron (x is anywhere between x_{\min} and x_{\max} (see Figure 6.39b)). According to the cosine law, this distance equals to:

$$d = \sqrt{r^2 + x^2 - 2xr \cos(\pi/2 - \varphi)}, \quad (6.10)$$

From Figure 6.39b it follows that the angle $\vartheta - \beta$ equals $\pi/2 - \alpha$, from where we can express: $\beta = \vartheta + \alpha - \pi/2$. Eq. (6.9) can then be written as:

$$R(r, x, \alpha, \vartheta) = A \int_{x_{\min}}^{x_{\max}} \frac{1}{r^2 + x^2 - 2xr \cos(\pi/2 - \varphi)} \cos\left(\frac{\pi}{2} - \alpha\right) dx. \quad (6.11)$$

Using the law of sines, angle α can be extracted from:

$$\sin \alpha = \sin\left(\frac{\pi}{2} - \varphi\right) \frac{r}{d}. \quad (6.12)$$

Taking all the above equations into account (Eqs. (6.9) – (6.12)), the contribution of all point-like sources to the semicircular substrate at distance d finally depends only on the angle φ when r and x are known quantities:

$$R(x, r, \varphi) = A \int_{x_{\min}}^{x_{\max}} \frac{r \cos(\varphi)}{(r^2 + x^2 - 2rx \sin(\varphi))^{3/2}} dx; \quad 0 \leq \varphi \leq \pi/2. \quad (6.13)$$

Finally, we also consider the contribution from the opposite side of the magnetron in the same way since the experiment is symmetrical.

To estimate the limits of integration, or to determine the area from where the sputtered atoms originate, we took one of the targets that was already worn from use, where the racetrack is clearly pronounced and visible (Figure 6.39a). The boundaries of integration were set between 18 and 27 mm (see Figure 6.39a).

Using parameters $r = 100$ mm, $x_{\min} = 18$ mm and $x_{\max} = 27$ mm, we calculated the distribution of the sputtered particles on the semi-circular substrate which is shown as the green curve in Figure 6.40a. The shape of this distribution is consistent with the experimental data for Al, Ti, V, Nb and Ta. However, since we observe a slightly lower deposition rate for other elements (Zr, Mo, Hf, Cr and Cu) at angles lower than 40° , we examined the influence of the distance r between the center of the magnetron and the semicircular substrate. Furthermore, we also checked how the result is affected by the integration boundaries.

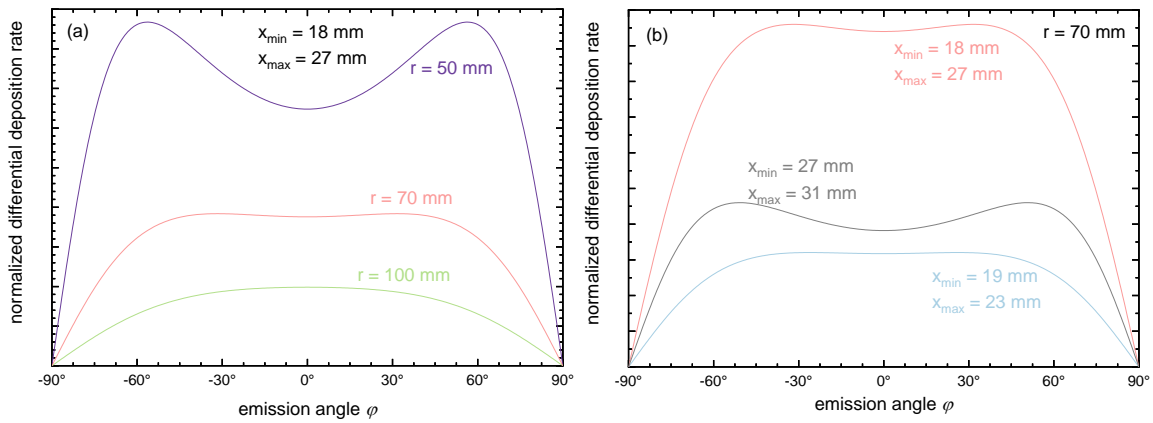


Figure 6.40: Normalized differential deposition rate on a semicircular substrate originating from the magnetron source: (a) the influence of variation of the semicircular radius r ; (b) the influence of the racetrack size and position. Note: y scales are not identical.

Figure 6.40a also shows the sputtering on a semicircular substrate if its radius is less than 100 mm (70 mm and 50 mm). Since the particle flux density decreases with the square of the distance, more atoms are deposited onto the substrate with lower r if the deposition time is the same. As the distance between the magnetron and the semicircular substrate decreases, the distributions of deposited atoms show that the atoms come from two planar sources. Two maxima appear in the distribution and fewer particles are sputtered into the angle interval between them. At a distance of $r = 50$ mm when $x_{\min} = 18$ mm and $x_{\max} = 27$ mm, even 20 % less atoms are sputtered at 0° angle than at 60° angle (see purple line). In addition, a significant sputtering rate drop toward zero appears at different angles as r decreases. For $r = 10$ cm (green line) sputtering rate starts to decrease toward zero at approximately 30° and for $r = 7$ cm (red line) at approximately 45° .

On the other hand, the shape of the deposited atom distribution originating from the magnetron is also influenced by the source from which the sputtered atoms originate. The influence of the position and width of the racetrack region are shown in Figure 6.40b. All three calculations were performed for sputtering on a semicircular substrate with $r = 70$ mm. The red line shows the same calculation as the red line in Figure 6.40a. First, we varied the width of the racetrack region. The blue line shows the calculation where x_{\min} was set to 19 mm and x_{\max} to 23 mm. Both distributions (red and blue line) have a fairly flat central part. The contribution from the wider racetrack region (red line) barely noticeably decreases, for the angles close to 0° , but we need to be aware that the center of this racetrack is at 22.5 mm, while the center of the narrower racetrack is at 21 mm.

The deposition rate for the racetrack with $x_{\min} = 27$ mm and $x_{\max} = 31$ mm is presented by a gray line in Figure 6.40b. The width of both racetracks, the one that results in deposition rate presented with gray and with blue lines is 4 mm, but as we can see from the comparison, their contribution to the distribution of the deposited particles is very different. When the inner radius of the magnetron is lower, we obtain an almost completely uniformly applied layer between -45° and 45° . With a larger inner radius of the racetrack, we get about 15 % more deposited particles at 50° than at 0° (see gray line).

Based on the calculations, we see that even minimal differences between the experimental setups can lead to substantially different amounts of deposited atoms at different sputtering angles. In addition to our calculations, we must be aware that magnetrons are not perfectly flat. After a short time, a channel of a specific shape is created in the racetrack – more material is sputtered from the central region of the racetrack. This

means that the ions in this part are no longer impinging perpendicularly to the surface and the atoms do not sputter from the ideally flat surface that is perpendicular to the substrate. In our calculation, however, we assumed a completely flat surface of the magnetron and a cosine distribution of the sputtered material.

So far, we have tried to explain the results with a simplified analytical calculation. In the next step, we tried to experiment in such a way that the deposited particles would originate from a narrower part of the magnetron and not from the entire racetrack region.

In order to experimentally achieve a nearly point-like source of atoms in our vacuum chamber, we placed a collimators in front of the samples so that only the atoms sputtered directly at a certain angle from a narrow part of the magnetron surface would be deposited onto the surface of the sample (Figure 5.9). The collimators were 10 mm long tubes with a diameter of 6 mm. This allowed us to see if our experiment was consistent with the SRIM simulations. In this case, we did not measure the thickness of the deposited films but measured the mass of the samples before and after the deposition of Cu.

When we calculate the differential sputtering yield and compare it to the SRIM simulations, the expected sputtering yield from SRIM simulations is significantly higher than the measured values. In the central region, near the surface normal, it is higher even for a factor above 2.5. The differences are lower at higher emission angles. Another surprising outcome is that we did not achieve the point-like source approximation by adding collimators: the number of sputtered particles was approximately the same at all samples positioned at emission angles below 30°. These measurements do not exhibit the angular distribution as expected by SRIM.

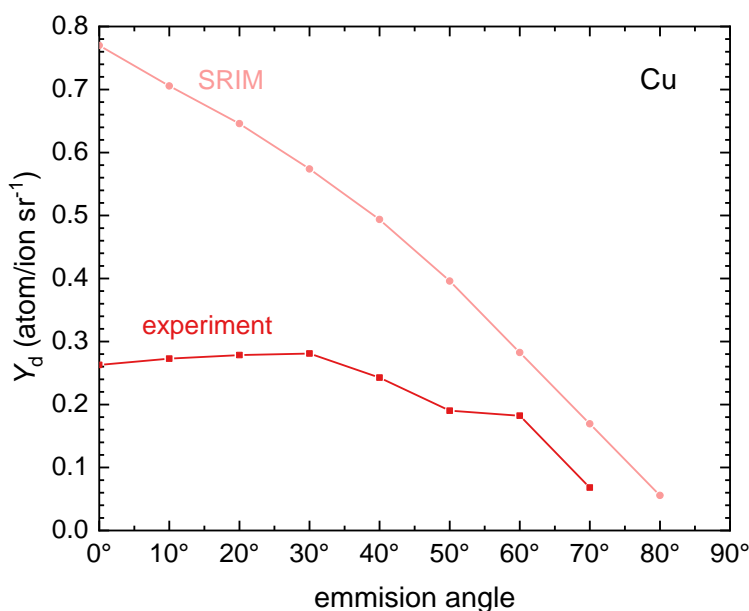


Figure 6.41: Differential sputtering yield measurements and SRIM simulations of Cu.

This difference could originate from the direction of the collimators. Although we used the magnetron target, which was planar, the minimum surface slope of the target surface (it could be the slope of the target surface within the racetrack) from where the atoms originated could also cause the difference in the result.

However, since these are not realistic conditions for sputtering in the deposition processes, and the material consumption is high, we decided not to perform further measurements with other materials.

Chapter 7

Conclusions

Ion bombardment is an important process in various scientific and technological fields, and is the basis of ion etching and sputtering. Sputtering depends on several parameters, including ion energy, mass, current density, angle of incidence and target material properties.

The Stopping and Range of Ions in Matter (SRIM) program was employed to conduct comprehensive simulations investigating the total sputtering yield, angular distribution of sputtered atoms, energy distributions and average energies for a range of materials. We focused on transition metals from groups 4, 5, 6, and 11 of the periodic table, as well as selected lighter elements (B, C, Al and Si) that are relevant in sputter deposition processes. The simulations involved the use of Ar ions with energy in the range of 300 to 1200 eV for both normal and oblique ion incidence at various ion energies.

The main objective was to improve the agreement between the simulated and experimental sputtering yield data. This was achieved primarily by modification of surface binding energies (SBEs) but also involving other parameters. SBE significantly influences the sputtering yield and is a free input parameter in SRIM. By adjusting this parameter, the experimental total sputtering yields were calculated, particularly within the energy range typical for sputter deposition techniques, namely below 1200 eV.

For transition metals, the total sputtering yield increased with increasing group in the periodic table. Notably, elements in group 4 exhibited the lowest sputtering yields with elements from group 11 demonstrating the highest yields. For lighter elements in groups 13 and 14, except for Al, the sputtering yields were considerably lower compared to the transition metals.

Furthermore, the simulations revealed that transition metals tend to exhibit a cosine angular distribution of sputtered atoms. In contrast, elements with atomic numbers below 14 (B, C, and Al) displayed a predominantly directional sputtering pattern, particularly near the surface normal. This unusual sputtering behavior is an artifact of the SRIM simulations, as it contradicts experimental observations which has already been reported by other authors. Consequently, the accuracy of the differential sputtering yields for these lower atomic number elements was questionable, while the simulations remained valuable for providing insights into total sputtering yields.

The analysis was extended to investigate angular distributions for oblique ion incidence. A noticeable trend was observed, with a more asymmetric distribution at lower ion energies transitioning to a more symmetric pattern at higher ion energies. The degree of symmetry was found to be dependent on the group within the periodic table and the atomic mass of the element within that group. Elements from group 4 exhibited the most pronounced asymmetry, while those from group 11 displayed a higher degree of symmetry. Heavier elements generally demonstrated more symmetric atom distributions compared to their lighter counterparts within the same group.

To gain a deeper understanding of the influence of target and ion properties on total sputtering yield, an analytical expression derived by Sigmund was employed. Comparisons between sputtering yields simulated by SRIM and those predicted by Sigmund simplified equation revealed comparable trends, particularly when incorporating modified surface binding energies. The dependence of the target-to-ion mass ratio, as suggested by Sigmund formula, also demonstrated a reasonable agreement with simulated values. Notably, deviations were more pronounced in terms of ion energy dependence, with Sigmund linear prediction differing from the parabolic dependence observed in both simulated and experimental data.

To address this discrepancy, a modified equation was introduced that included a power parameter relating ion energy and modified surface binding energy. The results of the modified equation agree with experimental sputtering yields for Ar ions with energies up to 1000 eV. In addition, a linear relationship was established between the power fitting coefficient and the atomic number for transition metals, which allowed the estimation of the total sputtering yield for other transition elements. This approach showed a reasonable agreement between the calculated and the experimental yield values. Although the modified equation is suitable for other ion types, the appropriate power coefficients should be determined by a similar procedure as in this thesis.

In the second part of the thesis, we investigated the angular energy distributions of sputtered atoms and explored the impact of various parameters on energy distribution. Additionally, we analyzed average energies of sputtered atoms across different spatial directions.

Simulation results of energy distribution functions (EDFs) and average energies of sputtered atoms were compared with analytical EDFs derived by Sigmund and Thompson. The EDF characteristics were discussed, including the low-energy peak, the high-energy tail, the high-energy peaks, and the maximum energy of the sputtered atoms with respect to the arrangement in the periodic table.

Comparison between the total EDFs produced by the SRIM simulations and the EDFs predicted by Sigmund and Thompson showed a good agreement for all transition metals, although minor differences were evident in the energy tail. However, a notable discrepancy was observed for the light elements (B, C, Al, and Si), where the simulated and analytical EDFs differed significantly. The simulated lighter element EDFs differed from both the analytical results and from the experimental EDFs taken from the existing literature. This shows that the SRIM simulations do not accurately represent the EDFs for elements with atomic number lower than 14. We draw this conclusion based on the fact that all simulated lighter elements (B, C, Al, and Si) exhibited major disagreement with the analytical results and experimental measurements. Note that we did not check all elements of the periodic table. In addition, the shape of the total EDFs normalized to the low-energy peak exhibited no variation with ion energy.

SRIM simulations predict that the low-energy peak appears at approximately half of the surface binding energy for all elements, which is consistent with the Sigmund and Thompson distribution. Comparisons within each period showed that the position of the low-energy peak increases with the group number, except for the elements in group 11.

Full width at half maximum (FWHM) analysis of the simulated EDFs revealed an increasing trend with atomic number within a given group, while ion energy variations in the 300–1200 eV range had negligible effects. The maximum energy of the sputtered atoms depends strongly on the period and slightly on the group of the periodic table. In particular, period 4 elements exhibited the highest maximum energies, followed by period 5 and 6 elements. While the maximum energy values derived from the SRIM simulations agree with those predicted by the Thompson equation for the transition metal elements, they differ significantly for the light elements, for which the SRIM simulations predicted much lower energies.

Comparison of the simulated angular EDFs with the Sigmund–Thompson distribution revealed a significant reduction in magnitude of simulated EDFs, often by as much as two orders of magnitude. This divergence was supported by experimental data indicating an overestimation of angular EDFs by the angular Sigmund distribution. Notable observations include the presence of broad high-energy peaks in SRIM simulations at emission angles above 45° for elements of periods 5 and 6, especially when sputtering with 300 eV Ar ions. Such peaks also occurred for some period 6 elements under ion bombardment with 600 eV. At an ion energy of 1200 eV, small high-energy peaks appeared at period 6 elements, while they were absent at the others.

For transition metals, an inverse proportionality was observed between the average energy of the sputtered atoms and the sputtering yield. We established an empirical equation according to which the average energy of sputtered atoms is approximately inversely proportional to the sputtering yield, with a power of about 0.5. The average energy of sputtered atoms increases linearly with the energy of incident Ar ions according to our fitting function. Such a qualitative relationship provides an estimate for the total average energies of the studied transition metals in the energy range of 300–1200 eV and possibly also for other transition metals and for higher Ar energies.

While the main goal of this work was to compare the analytical model and Monte Carlo simulations of sputtering processes, we also decided to perform a comparison between simulations of sputtering yield with optimized surface binding energies and measurements in sputtering systems. We presented measurements of the total sputtering yield in a triode sputtering system and measurements of the differential sputtering yield for thin films deposited in a magnetron system. The deviations between the SRIM simulations and experimental sputtering yields were most pronounced at an Ar ion energy of 100 eV. While the measurements of Cu and Cr above 100 eV agreed with the simulations, the discrepancies were more pronounced for V and Ti. In addition, we measured differential sputtering yields, with Cu having the highest differential sputtering yield, while other elements had significantly lower values. The differential sputtering yield was the highest for all measured elements at $40\text{--}50^\circ$ emission angles and decreased with emission angle.

References

- [1] F. A. Stevie, *Secondary Ion Mass Spectrometry: Applications for Depth Profiling and Surface Characterization*. Momentum Press, 2016.
- [2] J. C. Vickerman and D. Briggs, *Tof-SIMS: materials analysis by mass spectrometry*. Surface Spectra, 2013.
- [3] K. Nojiri, *Dry etching technology for semiconductors*. Springer, 2015.
- [4] L. A. Giannuzzi, *Introduction to focused ion beams: instrumentation, theory, techniques and practice*. Springer Science & Business Media, 2004.
- [5] R. Timilsina and P. D. Rack, "Monte Carlo simulations of nanoscale focused neon ion beam sputtering," *Nanotechnology*, vol. 24, no. 49, p. 495303, Dec 13 2013.
- [6] N. Yao, *Focused Ion Beam Systems: Basics and Applications*. Cambridge University Press, 2011.
- [7] R. Stadlmayr *et al.*, "Fluence dependent changes of surface morphology and sputtering yield of iron: Comparison of experiments with SDTrimSP-2D," *Nuclear Instruments and Methods in Physics Research Section B: Beam Interactions with Materials and Atoms*, vol. 430, pp. 42-46, 2018.
- [8] R. Stadlmayr *et al.*, "Sputtering of nanostructured tungsten and comparison to modelling with TRI3DYN," *Journal of Nuclear Materials*, vol. 532, p. 152019, 2020.
- [9] S. J. Lindsey, G. Hobler, D. Maciążek, and Z. Postawa, "Simple model of surface roughness for binary collision sputtering simulations," *Nuclear Instruments and Methods in Physics Research Section B: Beam Interactions with Materials and Atoms*, vol. 393, pp. 17-21, 2017.
- [10] M. Kelemen *et al.*, "Influence of surface roughness on the sputter yield of Mo under keV D ion irradiation," *Journal of Nuclear Materials*, vol. 555, p. 153135, 2021.
- [11] G. Z. Li and R. E. Wirz, "Persistent Sputtering Yield Reduction in Plasma-Infused Foams," *Phys Rev Lett*, vol. 126, no. 3, p. 035001, Jan 22 2021.
- [12] C. Cupak *et al.*, "Sputter yields of rough surfaces: Importance of the mean surface inclination angle from nano- to microscopic rough regimes," *Applied Surface Science*, vol. 570, p. 151204, 2021.
- [13] D. Nishijima, M. J. Baldwin, R. P. Doerner, and J. H. Yu, "Sputtering properties of tungsten 'fuzzy' surfaces," *Journal of Nuclear Materials*, vol. 415, no. 1, pp. S96-S99, 2011.
- [14] P. S. Szabo *et al.*, "Experimental Insights Into Space Weathering of Phobos: Laboratory Investigation of Sputtering by Atomic and Molecular Planetary Ions," *Journal of Geophysical Research: Planets*, vol. 125, no. 12, 2020.

- [15] B. Schmidt and K. Wetzig, *Ion beams in materials processing and analysis*. Springer Science & Business Media, 2012.
- [16] I. Petrov, F. Adibi, J. Greene, L. Hultman, and J. E. Sundgren, "Average energy deposited per atom: A universal parameter for describing ion-assisted film growth?," *Applied physics letters*, vol. 63, no. 1, pp. 36-38, 1993.
- [17] J. Greene, J. E. Sundgren, L. Hultman, I. Petrov, and D. Bergstrom, "Development of preferred orientation in polycrystalline TiN layers grown by ultrahigh vacuum reactive magnetron sputtering," *Applied physics letters*, vol. 67, no. 20, pp. 2928-2930, 1995.
- [18] J. Musil, H. Poláková, J. Šuna, and J. Vlček, "Effect of ion bombardment on properties of hard reactively sputtered Ti(Fe)N_x films," *Surface and Coatings Technology*, vol. 177-178, pp. 289-298, 2004.
- [19] G. Greczynski *et al.*, "A review of metal-ion-flux-controlled growth of metastable TiAlN by HIPIMS/DCMS co-sputtering," *Surface and Coatings Technology*, vol. 257, pp. 15-25, 2014.
- [20] J. Xia, W. Liang, Q. Miao, and D. Depla, "The effect of energy and momentum transfer during magnetron sputter deposition of yttrium oxide thin films," *Applied Surface Science*, vol. 439, pp. 545-551, 2018.
- [21] G. Greczynski, S. Mráz, J. M. Schneider, and L. Hultman, "Metal-ion subplantation: A game changer for controlling nanostructure and phase formation during film growth by physical vapor deposition," *Journal of Applied Physics*, vol. 127, no. 18, p. 180901, 2020.
- [22] A. Anders, "A structure zone diagram including plasma-based deposition and ion etching," *Thin Solid Films*, vol. 518, no. 15, pp. 4087-4090, 2010.
- [23] A. Bogaerts *et al.*, "Computer modelling of magnetron discharges," *Journal of physics D: applied physics*, vol. 42, no. 19, p. 194018, 2009.
- [24] D. Depla, S. Mahieu, and R. De Gryse, "Magnetron sputter deposition: Linking discharge voltage with target properties," *Thin Solid Films*, vol. 517, no. 9, pp. 2825-2839, 2009.
- [25] M. Raadu, I. Axnäs, J. T. Gudmundsson, C. Huo, and N. Brenning, "An ionization region model for high-power impulse magnetron sputtering discharges," *Plasma Sources Science Technology*, vol. 20, no. 6, p. 065007, 2011.
- [26] D. Depla and W. Leroy, "Magnetron sputter deposition as visualized by Monte Carlo modeling," *Thin Solid Films*, vol. 520, no. 20, pp. 6337-6354, 2012.
- [27] D. Depla, "On the effective sputter yield during magnetron sputter deposition," *Nuclear Instruments Methods in Physics Research Section B: Beam Interactions with Materials*, vol. 328, pp. 65-69, 2014.
- [28] H. Winter and J. Burgdörfer, *Slow heavy-particle induced electron emission from solid surfaces*. Springer, 2007.
- [29] W. Eckstein, *Computer simulation of ion-solid interactions*. Springer Science & Business Media, 2013.
- [30] P. Sigmund, *Stopping of heavy ions: a theoretical approach*. Springer Science & Business Media, 2004.

- [31] R. Behrisch and W. Eckstein, *Sputtering by Particle Bombardment: Experiments and Computer Calculations from Threshold to MeV Energies*. Springer Berlin Heidelberg, 2007.
- [32] F. H. Attix, *Introduction to radiological physics and radiation dosimetry*. John Wiley & Sons, 2008.
- [33] E. Rutherford, "The scattering of α and β particles by matter and the structure of the atom", *Philosophical Magazine*, vol. 92, no. 4, pp. 379-398, 2012.
- [34] G. Moliere, "Theorie der streuung schneller geladener teilchen i. einzelstreuung am abgeschirmten coulomb-feld," *Zeitschrift für Naturforschung A*, vol. 2, no. 3, pp. 133-145, 1947.
- [35] W. Wilson, L. Haggmark, J. Biersack, "Calculations of nuclear stopping, ranges, and straggling in the low-energy region," *Physical Review B*, vol. 15, no. 5, p. 2458, 1977.
- [36] D. O'connor and J. Biersack, "Comparison of theoretical and empirical interatomic potentials," *Nuclear Instruments Methods in Physics Research Section B: Beam Interactions with Materials Atoms*, vol. 15, no. 1-6, pp. 14-19, 1986.
- [37] J. F. Ziegler, M. D. Ziegler, and J. P. Biersack, "SRIM – The stopping and range of ions in matter (2010)," *Nuclear Instruments and Methods in Physics Research Section B: Beam Interactions with Materials and Atoms*, vol. 268, no. 11-12, pp. 1818-1823, 2010.
- [38] A. Bohr, *Atomic interaction in penetration phenomena*. Munksgaard Copenhagen, Denmark, 1948.
- [39] W. Lenz, "Über die Anwendbarkeit der statistischen Methode auf Ionengitter," *Zeitschrift für Physik*, vol. 77, no. 11-12, pp. 713-721, 1932.
- [40] H. Jensen, "Die Ladungsverteilung in Ionen und die Gitterkonstante des Rubidumbromids nach der statistischen Methode," *Zeitschrift für Physik*, vol. 77, no. 11-12, pp. 722-745, 1932.
- [41] R. Behrisch, *Sputtering by Particle Bombardment I: Physical Sputtering of Single-Element Solids*. Springer Berlin Heidelberg, 2014.
- [42] J.E. Mahan, *Physical vapor deposition of thin films*, Wiley-VCH, 2000.
- [43] J. Biersack and W. Eckstein, "Sputtering studies with the Monte Carlo program TRIM. SP," *J. Applied Physics A*, vol. 34, no. 2, pp. 73-94, 1984.
- [44] W. Eckstein and R. Preuss, "New fit formulae for the sputtering yield," *Journal of Nuclear Materials*, vol. 320, no. 3, pp. 209-213, 2003.
- [45] M. W. Thompson, "II. The energy spectrum of ejected atoms during the high energy sputtering of gold," *Philosophical Magazine*, vol. 18, no. 152, pp. 377-414, 1968.
- [46] P. Sigmund, "Theory of Sputtering. I. Sputtering Yield of Amorphous and Polycrystalline Targets," *Physical Review*, vol. 184, no. 2, pp. 383-416, 1969.
- [47] N. Mahne, M. Čekada, and M. Panjan, "Energy Distribution of Sputtered Atoms Explored by SRIM (Stopping and Range of Ions in Matter) Simulations," *Coatings*, vol. 13, no. 8, 2023.
- [48] M. W. Thompson, "The contribution of collision cascades to sputtering and radiation damage," *Philosophical Transactions of the Royal Society of London*,

- Series A: Mathematical, Physical and Engineering Sciences*, vol. 362, no. 1814, pp. 5-28, 2003.
- [49] G. H. Kinchin and R. S. Pease, "The displacement of atoms in solids by radiation," *Reports on progress in physics*, vol. 18, no. 1, p. 1, 1955.
- [50] P. Sigmund, "Mechanisms and theory of physical sputtering by particle impact," *Nuclear Instruments and Methods in Physics Research Section B: Beam Interactions with Materials and Atoms*, vol. 27, no. 1, pp. 1-20, 1987.
- [51] M. W. Thompson, J. S. Colligon, and W. R. Grove, *Sputtering: Past, Present and Future, W.R. Grove 150th Anniversary Issue : Papers of a Theme Issue*. Royal Society, 2004.
- [52] C. Garcia-Rosales, W. Eckstein, and J. Roth, "Revised formulae for sputtering data," *Journal of nuclear materials*, vol. 218, no. 1, pp. 8-17, 1995.
- [53] J. Bohdansky, "A universal relation for the sputtering yield of monatomic solids at normal ion incidence," *Nuclear Instruments and Methods in Physics Research Section B: Beam Interactions with Materials and Atoms*, vol. 2, no. 1, pp. 587-591, 1984.
- [54] Y. Yamamura and H. Tawara, "Energy dependence of ion-induced sputtering yields from monatomic solids at normal incidence," *Atomic data and nuclear data tables*, vol. 62, no. 2, pp. 149-253, 1996.
- [55] H. Wilhelm, "Quantum-statistical analysis of low energy sputtering," *Australian Journal of Physics*, vol. 38, no. 2, pp. 125-134, 1985.
- [56] S. Shang, G. Cai, D. Zhu, and B. He, "An empirical formula for E_z in the modified Sigmund formula for low energy heavy ion bombardment," *Vacuum*, vol. 125, pp. 192-204, 2016.
- [57] L. Zhang and Z. L. Zhang, "Anisotropic energy distribution of sputtered atoms induced by low energy heavy ion bombardment," *Radiation Effects and Defects in Solids*, vol. 160, no. 8, pp. 337-347, 2005.
- [58] J. T. Yim, "A Survey of Xenon Ion Sputter Yield Data and Fits Relevant to Electric Propulsion Spacecraft Integration," in *35th International Electric Propulsion Conference*, Georgia Institute of Technology, Atlanta, Georgia, 2017.
- [59] N. Mahne, M. Čekada, and M. Panjan, "Total and Differential Sputtering Yields Explored by SRIM Simulations," *Coatings*, vol. 12, no. 10, 2022.
- [60] D. Depla, *Magnetrons, Reactive Gases and Sputtering*. Lulu.com, 2019.
- [61] J.F. Ziegler, J. Biersack, "TRIM, the transport of ions in matter," *New York, NY: IBM*, (1992).
- [62] J. P. Biersack and L. Haggmark, "A Monte Carlo computer program for the transport of energetic ions in amorphous targets," *Nuclear Instruments and Methods*, vol. 174, no. 1-2, pp. 257-269, 1980.
- [63] W. Takeuchi and Y. Yamamura, "Computer studies of the energy spectra and reflection coefficients of light ions," *Radiation Effects*, vol. 71, no. 1-2, pp. 53-64, 1983.
- [64] G. Abel, G. Ross, B. Terreault, and J. Labrie, "Ranges of 5–25 keV He^+ ions in Nb, Cu, Al and Be," *Nuclear Instruments Methods*, vol. 170, no. 1-3, pp. 171-175, 1980.

- [65] M. Vicanek and H. M. Urbassek, "Energy and angular distributions of sputtered particles: A comparison between analytical theory and computer simulation results," *Nuclear Instruments: Methods in Physics Research Section B: Beam Interactions with Materials Atoms*, vol. 30, no. 4, pp. 507-513, 1988.
- [66] T. Pugacheva, "Transition layer formation simulation during film deposition by an ion-molecular beam," *Radiation effects*, vol. 102, no. 1-4, pp. 143-155, 1987.
- [67] J. Beeler Jr, "Computer experiment methods," in *Radiation effects computer experiments*, 1983.
- [68] Y. Yamamura, "Sputtering by cluster ions," *Nuclear Instruments Methods in Physics Research Section B: Beam Interactions with Materials Atoms*, vol. 33, no. 1-4, pp. 493-496, 1988.
- [69] J. Tatariewicz, "Distributions of energetic proton ranges in silicon as determined by the Monte Carlo method," *Nuclear Instruments Methods*, vol. 146, no. 2, pp. 447-453, 1977.
- [70] M. Roush, T. Andreadis, and O. Goktepe, "Evolve, a time-dependent monte carlo code to simulate the effects of ion-beam-induced atomic mixing," *Radiation Effects*, vol. 55, no. 1-2, pp. 119-129, 1981.
- [71] H. Attaya and G. Kulcinski, "Report UWFD-479," *University of Wisconsin*, 1982.
- [72] A. Schönborn, N. Hecking, and E. Te Kaat, "Dynamic monte carlo simulation of high dose effects during ion bombardment," *Nuclear Instruments Methods in Physics Research Section B: Beam Interactions with Materials Atoms*, vol. 43, no. 2, pp. 170-175, 1989.
- [73] C. M. Davison, "IMPLNT—A fortran program to calculate the distribution of implanted ions which includes the effects due to sputtering," *Nuclear Instruments Methods in Physics Research Section B: Beam Interactions with Materials Atoms*, vol. 13, no. 1-3, pp. 421-425, 1986.
- [74] A. Hassanein and D. Smith, "Elastic and inelastic surface effects on ion penetration and the resulting sputtering and backscattering," *Nuclear Instruments Methods in Physics Research Section B: Beam Interactions with Materials Atoms*, vol. 13, no. 1-3, pp. 225-229, 1986.
- [75] V. Nikiforov, V. Pavlenko, R. Slabospitskij, and I. Khirnov, "Simulation of sputtering for multi-component solids by ion bombardment: attestation of the PERST program," *AN Ukrainskoj SSR* 1987.
- [76] I. Adesida and L. Karapiperis, "Monte Carlo simulation of ion beam penetration in solids," *Radiation Effects*, vol. 61, no. 3-4, pp. 223-233, 1982.
- [77] A. Desalvo and R. Rosa, "Rita, a promising monte carlo code for recoil implantation," *Radiation Effects*, vol. 67, no. 4, pp. 119-123, 1982.
- [78] A. Mel'ker and S. Romanov, "Distribution of vacancies interstitial atoms and thermal spikes in cascade collisions," *Fizika i Khimiya Obrabotki Materialov*, pp. 12-21, 1979.
- [79] Y. Miyagawa and S. Miyagawa, "Computer simulation of ion beam penetration in amorphous target," *Journal of applied physics*, vol. 54, no. 12, pp. 7124-7131, 1983.
- [80] D. Jackson, "Comparison of ion backscattering models," *Journal of Nuclear Materials*, vol. 93, pp. 507-511, 1980.

- [81] C. Fu-Zhai and L. Heng-De, "Recoil implantation and interface mixing: A computer simulation study," *Nuclear Instruments Methods in Physics Research Section B: Beam Interactions with Materials Atoms*, vol. 7, pp. 650-656, 1985.
- [82] W. Möller, W. Eckstein, and J. Biersack, "Tridyn-binary collision simulation of atomic collisions and dynamic composition changes in solids," *Computer Physics Communications*, vol. 51, no. 3, pp. 355-368, 1988.
- [83] W. Möller and W. Eckstein, "Tridyn—A TRIM simulation code including dynamic composition changes," *Nuclear Instruments Methods in Physics Research Section B: Beam Interactions with Materials Atoms*, vol. 2, no. 1-3, pp. 814-818, 1984.
- [84] J. F. Ziegler and J. P. Biersack, "The stopping and range of ions in matter," in *Treatise on Heavy-Ion Science*: Springer, 1985, pp. 93-129.
- [85] P. Chou and N. Ghoniem, "Collisional aspects of preferential sputtering using the Monte Carlo method," *Journal of Nuclear Materials*, vol. 141, pp. 216-220, 1986.
- [86] A. Anders, "Discharge physics of high power impulse magnetron sputtering," *Surface and Coatings Technology*, vol. 205, S2, pp. S1-S9, 7/25/ 2011.
- [87] A. Kramida, et al. (08 10). *NIST Atomic Spectra Database (version 5.4)*. Available: <http://physics.nist.gov/asd>, (3. 12. 2023)
- [88] M. Panjan and A. Anders, "Plasma potential of a moving ionization zone in DC magnetron sputtering," *Journal of Applied Physics*, vol. 121, no. 6, p. 063302, 2017.
- [89] K. A. Zoerb, J. D. Williams, D. D. Williams, and A. P. Yalin, "Differential sputtering yields of refractory metals by xenon, krypton, and argon ion bombardment at normal and oblique incidences," in *29th International Electric Propulsion Conference*, 2005, pp. 2005-293.
- [90] A. Yalin, J. Williams, V. Surla, K. Zoerb, "Differential sputter yield profiles of molybdenum due to bombardment by low energy xenon ions at normal and oblique incidence," *Journal of Physics D: Applied Physics*, vol. 40, no. 10, p. 3194, 2007.
- [91] B. Rubin, J. L. Topper, and A. P. Yalin, "Total and differential sputter yields of boron nitride measured by quartz crystal microbalance," *Journal of Physics D: Applied Physics*, vol. 42, no. 20, p. 205205, 2009.
- [92] A. Farhadizadeh and T. Kozák, "The importance of discharge voltage in DC magnetron sputtering for energy of sputtered and backscattered atoms on the substrate: Monte-Carlo simulations," *Vacuum*, vol. 196, p. 110716, 2022.
- [93] N. Matsunami, Y. Yamamura, Y. Itikawa, N. Itoh, Y. Kazumata, S. Miyagawa, K. Morita, R. Shimizu, H. Tawara, "Energy dependence of sputtering yields of monatomic solids," *Atomic data - nuclear data tables*, vol. 31, no. 1, p. 1-80, 1984.
- [94] N. Matsunami *et al.*, "Energy dependence of the ion-induced sputtering yields of monatomic solids," *Atomic Data and Nuclear Data Tables*, vol. 31, no. 1, pp. 1-80, 1984/07/01/ 1984.
- [95] Z. Somogyvári, G. A. Langer, G. Erdélyi, and L. Balázs, "Sputtering yields for low-energy Ar⁺ and Ne⁺ ion bombardment," *Vacuum*, vol. 86, no. 12, pp. 1979-1982, 2012.
- [96] R. D. Kolasinski, J. E. Polk, D. Goebel, and L. K. Johnson, "Carbon sputtering yield measurements at grazing incidence," *Applied Surface Science*, vol. 254, no. 8, pp. 2506-2515, 2008.

- [97] M. Chen, C. Rohrbach, A. Neuffer, K.-L. Barth, and A. Lunk, "Simulation of boron nitride sputtering process and its comparison with experimental data," *IEEE Transactions on Plasma Science*, vol. 26, no. 6, pp. 1713-1717, 1998.
- [98] D. Rosenberg and G. Wehner, "Sputtering Yields for Low Energy He⁺, Kr⁺, and Xe⁺ Ion Bombardment," *Journal of Applied Physics*, vol. 33, no. 5, pp. 1842-1845, 1962.
- [99] N. Laegreid and G. Wehner, "Sputtering yields of metals for Ar⁺ and Ne⁺ ions with energies from 50 to 600 eV," *Journal of Applied Physics*, vol. 32, no. 3, pp. 365-369, 1961.
- [100] Y. Yamamura and K. Muraoka, "Over-cosine angular distributions of sputtered atoms at normal incidence," *Nuclear Instruments and Methods in Physics Research Section B: Beam Interactions with Materials and Atoms*, vol. 42, no. 2, pp. 175-181, 1989.
- [101] V. I. Shulga, "Note on the artefacts in SRIM simulation of sputtering," *Applied Surface Science*, vol. 439, pp. 456-461, 2018.
- [102] K. Wittmaack, "Reliability of a popular simulation code for predicting sputtering yields of solids and ranges of low-energy ions," *Journal of applied physics*, vol. 96, no. 5, pp. 2632-2637, 2004.
- [103] H. Hofsäss, K. Zhang, and A. Mutzke, "Simulation of ion beam sputtering with SDTrimSP, TRIDYN and SRIM," *Applied Surface Science*, vol. 310, pp. 134-141, 2014.
- [104] G. Hobler, R. M. Bradley, and H. M. Urbassek, "Probing the limitations of Sigmund's model of spatially resolved sputtering using Monte Carlo simulations," *Physical Review B*, vol. 93, no. 20, p. 205443, 2016.
- [105] N. Novikov, Y. A. Teplova, Y. A. Fainberg, and V. Kulikauskas, "Reflection of nitrogen ions from copper surface: Experiment and calculations," *Nuclear Instruments: Methods in Physics Research Section B: Beam Interactions with Materials Atoms*, vol. 235, no. 1-4, pp. 448-451, 2005.
- [106] G. K. Wehner and D. Rosenberg, "Angular Distribution of Sputtered Material," *Journal of Applied Physics*, vol. 31, no. 1, pp. 177-179, 1960.
- [107] H. Tsuge and S. Esho, "Angular distribution of sputtered atoms from polycrystalline metal targets," *Journal of Applied Physics*, vol. 52, no. 7, pp. 4391-4395, 1981.
- [108] E. Oyarzabal, R. P. Doerner, M. Shimada, and G. R. Tynan, "Carbon atom and cluster sputtering under low-energy noble gas plasma bombardment," *Journal of Applied Physics*, vol. 104, no. 4, p. 043305, 2008.
- [109] E. Oyarzabal, J. Yu, R. Doerner, G. Tynan, K. Schmid, "Molybdenum angular sputtering distribution under low energy xenon ion bombardment," *Journal of applied physics*, vol. 100, no. 6, p. 063301, 2006.
- [110] G. M. Turner, S. M. Rossnagel, and J. J. Cuomo, "Measured radial and angular distributions of sputtered atoms in a planar magnetron discharge," *Journal of Applied Physics*, vol. 75, no. 7, p. 3611, 1994.
- [111] V. Surla and A. P. Yalin, "Differential sputter yield measurements using cavity ringdown spectroscopy," *Applied optics*, vol. 46, no. 19, pp. 3987-3994, 2007.

- [112] T. Chini, M. Tanemura, and F. Okuyama, "Angular distribution of sputtered Ge atoms by low keV Ar⁺ and Ne⁺ ion bombardment," *Nuclear Instruments, Methods in Physics Research Section B: Beam Interactions with Materials* vol. 119, no. 3, pp. 387-391, 1996.
- [113] R. Feder, C. Bundesmann, H. Neumann, and B. Rauschenbach, "Ion beam sputtering of Ag—Angular and energetic distributions of sputtered and scattered particles," *Nuclear Instruments and Methods in Physics Research Section B: Beam Interactions with Materials and Atoms*, vol. 316, pp. 198-204, 2013.
- [114] C. Bundesmann, R. Feder, R. Wunderlich, U. Teschner, M. Grundmann, and H. Neumann, "Ion beam sputter deposition of Ge films: Influence of process parameters on film properties," *Thin Solid Films*, vol. 589, pp. 487-492, 2015.
- [115] D. N. Ruzic, "The effects of surface roughness characterized by fractal geometry on sputtering," *Nuclear Instruments and Methods in Physics Research Section B: Beam Interactions with Materials and Atoms*, vol. 47, no. 2, pp. 118-125, 1990.
- [116] K. Schlueter *et al.*, "Absence of a Crystal Direction Regime in which Sputtering Corresponds to Amorphous Material," *Phys Rev Lett*, vol. 125, no. 22, p. 225502, 2020.
- [117] T. Lautenschläger, R. Feder, H. Neumann, C. Rice, M. Schubert, and C. Bundesmann, "Ion beam sputtering of Ti: Influence of process parameters on angular and energy distribution of sputtered and backscattered particles," *Nuclear Instruments and Methods in Physics Research Section B: Beam Interactions with Materials and Atoms*, vol. 385, pp. 30-39, 2016.
- [118] J. Dembowski, H. Oechsner, Y. Yamamura, and M. Urbassek, "Energy distributions of neutral atoms sputtered from Cu, V and Nb under different bombardment and ejection angles," *Nuclear Instruments and Methods in Physics Research Section B: Beam Interactions with Materials and Atoms*, vol. 18, no. 1, pp. 464-470, 1986/01/01/ 1986.
- [119] C. Bundesmann, R. Feder, T. Lautenschläger, and H. Neumann, "Energy Distribution of Secondary Particles in Ion Beam Deposition Process of Ag: Experiment, Calculation and Simulation," *Contributions to Plasma Physics*, vol. 55, no. 10, pp. 737-746, 2015.
- [120] W. Eckstein, "Energy distributions of sputtered particles," *Nuclear Instruments and Methods in Physics Research B*, vol. 18, no. 1, pp. 344-348, 1986.
- [121] M. Stepanova and S. Dew, "Estimates of differential sputtering yields for deposition applications," *Journal of Vacuum Science & Technology A: Vacuum, Surfaces, and Films*, vol. 19, no. 6, pp. 2805-2816, 2001.
- [122] R. A. Brizzolara, C. B. Cooper, and T. K. Olson, "Energy distributions of neutral atoms sputtered by very low energy heavy ions," *Nuclear Instruments and Methods in Physics Research Section B: Beam Interactions with Materials and Atoms*, vol. 35, no. 1, pp. 36-42, 1988/11/01/ 1988.
- [123] A. Goehlich, N. Niemöller, and H. Döbele, "Anisotropy effects in physical sputtering investigated by laser-induced fluorescence spectroscopy," *Physical Review B*, vol. 62, no. 14, p. 9349, 2000.

- [124] D. Kalanov, A. Anders, and C. Bundesmann, "Ion beam sputtering of silicon: Energy distributions of sputtered and scattered ions," *Journal of Vacuum Science & Technology A*, vol. 37, no. 5, p. 051507, 2019.
- [125] R. Feder, F. Frost, H. Neumann, C. Bundesmann, and B. Rauschenbach, "Systematic investigations of low energy Ar ion beam sputtering of Si and Ag," *Nuclear Instruments and Methods in Physics Research Section B: Beam Interactions with Materials and Atoms*, vol. 317, pp. 137-142, 2013.
- [126] R. Feder, C. Bundesmann, H. Neumann, and B. Rauschenbach, "Ion beam sputtering of germanium—Energy and angular distribution of sputtered and scattered particles," *Nuclear Instruments and Methods in Physics Research Section B: Beam Interactions with Materials and Atoms*, vol. 334, pp. 88-95, 2014.
- [127] J. Held, A. Hecimovic, A. von Keudell, and V. Schulz-von der Gathen, "Velocity distribution of titanium neutrals in the target region of high power impulse magnetron sputtering discharges," *Plasma Sources Science and Technology*, 2018.
- [128] D. Depla, *Magnetrons, Reactive Gases and Sputtering*. Lulu.com, 2017.

Bibliography

Publications Related to the Thesis

Journal Articles

- N. Mahne, M. Čekada, M. Panjan, "Energy Distribution of Sputtered Atoms Explored by SRIM Simulations", *Coatings*, vol. 13, 2023: 1441.
- N. Mahne, M. Čekada, M. Panjan, "Total and Differential Sputtering Yields Explored by SRIM Simulations," *Coatings*, vol. 12, no. 10, 2022: 1541.
- P. Panjan, A. Drnovšek, N. Mahne, M. Čekada, M. Panjan, "Surface Topography of PVD Hard Coatings". *Coatings*, vol. 11, 2021: 1387.
- N. Mahne, M. Panjan, "Obstreljevanje trdnih snovi z ioni. 2., Simulacije razprševanja atomov", *Vakuumist*, vol. 41, no. 1/2, pp. 4–13, 2021.
- N. Mahne, M. Panjan, „Obstreljevanje trdnih snovi z ioni. 1., Teoretični opis razprševanja“, *Vakuumist*, vol. 40, no. 1/2, pp. 10–21, 2020.

Conference Papers

- N. Mahne, M. Čekada, M. Panjan, „Sputtering yields for a range of target materials calculated by SRIM simulations“, *RSD 2022, International Conference on Reactive Sputter Deposition: 7.-9. December 2022, Ghent, Belgium*, pp. 15, 2022.
- N. Mahne, M. Čekada, M. Panjan, „Monte Carlo simulations of sputtering yield for deposition-relevant target materials: invited lecture“, *Book of abstracts, International Scientific Meeting on Vacuum Science and Technique: 18.-20. may, Crikvenica, Croatia*, pp. 26, 2022.
- N. Mahne, M. Čekada, M. Panjan, „Calculatins of sputtering parameters by SRIM program for magnetron depositin“, *27. , International Scientific Meeting on Vacuum Science and Technique: 9.-10. september 2021, Gozd Martuljek*, pp. 43, 2021.
- N. Mahne, M. Panjan, M. Čekada, „Magnetron plasma characterization by optical emission spectroscopy“, *Throughout knowledge towards a green new world: 13. Študentska konferenca Mednarodne podiplomske šole Jožefa Stefana in 15. dan mladih raziskovalcev (Konferenca KMBO), 27-28 maj 2021, Planica, Slovenija*, pp. 74, 2021.
- N. Mahne, M. Panjan, P. Panjan, M. Čekada, „Analysis of magnetron sputtering and triode sputtering plasmas using optical emission spectroscopy“, *Book of abstracts, International Scientific Meeting on Vacuum Science and Technique: 16.-17. May, Njivice, Croatia*, pp. 31–32, 2019.

Biography

Nastja Mahne, the first of three siblings with two brothers, was born on 26 April 1991 in Ljubljana and raised in Kamnik, Slovenia. Nastja obtained her bachelor's degree in Physics from the Faculty of Mathematics and Physics, University of Ljubljana, in 2015. In 2016, she finished her master studies in Medical Physics at the Faculty of Mathematics and Physics, University of Ljubljana, and enrolled in the Nanosciences and Nanotechnologies third-level study program at the Jožef Stefan International Postgraduate School in Ljubljana. At the same time, she started working as a Young Scientist at the Department of Thin Films and Surfaces at the Jožef Stefan Institute in Ljubljana and as a teaching assistant at the Faculty of Mathematics and Physics, University of Ljubljana.

Alongside her academic pursuits, Nastja has found profound fulfillment in her personal life. She is happily married and a proud parent of two lovely daughters.